



TECHNISCHE  
UNIVERSITÄT  
WIEN  
Vienna University of Technology

DISSERTATION

# GAS SENSING PROPERTIES OF METAL OXIDE NANOWIRES AND THEIR CMOS INTEGRATION

ausgeführt zum Zwecke der Erlangung des akademischen Grades  
eines Doktors der technischen Wissenschaften

unter der Leitung von  
Ao.Univ.Prof. Mag. Dr. Jürgen Smoliner  
und  
Univ.Doiz. Mag. Dr. Anton Köck

eingereicht an der  
Technischen Universität Wien  
Fakultät für Elektrotechnik und Informationstechnik  
Institut für Festkörperelektronik

von  
**Dipl.-Ing. Stephan Steinhauer**  
Matr. Nr. 0825426  
Dürauergasse 12a/4/19  
A-1170 Wien

Wien, im August 2014

## Abstract

Highly sensitive gas detecting devices are of significant importance in various applications such as environmental air quality monitoring or occupational safety and health. In the last decades considerable advances have been made in the development of conductometric metal oxide gas sensors and in optimization of sensor performance regarding sensitivity and selectivity. Traditional metal oxide based gas sensors employ thin or thick film resistors and their working principle is based on electrical conductance changes due to interaction with surrounding gas molecules. Due to favorable material properties, nanowire-based devices are considered as potential candidate for the realization of miniaturized, next-generation gas sensors with improved performance. In particular the integration of nanomaterials with CMOS technology is expected to result in low power consumption gas sensor systems for daily life applications.

In this thesis, the gas sensing properties of nanowire devices based on two different metal oxide materials, i.e. cupric oxide (CuO) and zinc oxide (ZnO), are investigated. CuO and ZnO nanowires are obtained by various synthesis techniques on wire and thin film substrates. Complimentary characterization methods are employed for structural as well as compositional analysis. Fabrication processes are developed for the realization of single nanowire as well as nanowire array devices, which are characterized in terms of electrical properties and gas sensing performance. The nanowire gas sensors are operated at elevated temperatures up to 350 °C and device resistance changes are investigated during exposure to water vapor and small concentrations of the toxic gases CO (ppm-level range) and H<sub>2</sub>S (ppb-level range). The results obtained for the different sensor configurations are compared and interpreted in terms of sensing mechanism model. Furthermore, the integration of CuO nanowire arrays on CMOS microhotplates is demonstrated resulting in miniaturized, low power consumption gas sensor devices.

## Acknowledgements

The work presented in this thesis was conducted at the AIT Austrian Institute of Technology (business unit Molecular Diagnostics, Health & Environment Department) and the Materials Center Leoben. Financial support is acknowledged from the European projects COCOA (CATRENE), ESiP (ENIAC, FFG No.824954) and MSP (Framework Programme 7, Grant Agreement No.611887) as well as from the WWTF Vienna Science and Technology Fund project “Mathematics and Nanosensors” (No.MA09-028).

First of all, I would like to especially thank Univ.Doz. Mag. Dr. Anton Köck for giving me the opportunity to write this thesis, for his competent guidance and for constant encouragement. Furthermore, I am very grateful to my supervisor at university Ao.Univ.Prof. Mag. Dr. Jürgen Smoliner, who contributed to the completion of this thesis with highly appreciated advice.

I also want to thank Dr. Elise Brunet and Dr. Giorgio C. Mutinati for the stimulating working atmosphere as well as for the cheerful support and friendship. Moreover, I would like to show my gratitude to Dr. Thomas Maier, Dr. Jörg Schotter and Dr. Moritz Eggeling for their scientific support with the gas measurement setup, electron beam lithography and atomic force microscopy. I am very thankful to all other colleagues at AIT for making the last four years a very enjoyable time.

In addition, I am grateful to Martina Dienstleder and Dr. Christian Gspan from the Austrian Centre for Electron Microscopy and Nanoanalysis for sample preparation and transmission electron microscopy. I want to thank Ao.Univ.Prof. Dipl.-Ing. Dr. Roland Resel for providing the XRD measurement results presented in this thesis. Furthermore, successful collaboration with partners at ams AG, Siemens Corporate Technology and University of Applied Sciences Wr. Neustadt is acknowledged. I also want to show my gratitude to Ass.Prof. Dipl.-Ing. Dr. Christian Edtmaier (Vienna University of Technology) and Univ.Doz. Dipl.-Ing. Dr. Peter Pölt (Graz University of Technology) for energy-dispersive X-ray spectroscopy measurements.

In addition, I want to acknowledge Mag. Gerhard Tulzer and Dr. Clemens Heitzinger (Vienna University of Technology) for their work on mathematical modeling of nanowire surface reactions. Thank you to Dr. Lado Filipovic and O.Univ.Prof. Dipl.-Ing. Dr. Siegfried Selberherr (Vienna University of Technology) for mathematical modeling of spray pyrolysis deposition. Moreover, I am thankful to Dr. Olena Yurchenko (Freiburg Materials Research Center) as well as Dr. Vidyadhar Singh and Dr. Cathal Cassidy (Okinawa Institute of Science and Technology) for nanoparticle decoration of nanowire samples.

I want to thank my friends for distraction from work and for the great times we had during the last years. Finally, I am especially grateful to my family, in particular my mother and grandmother, for constantly supporting me throughout my life.

# Contents

<b>1</b>	<b>Introduction</b>	<b>1</b>
<b>2</b>	<b>Fundamentals of Metal Oxide Gas Sensors</b>	<b>9</b>
2.1	Solid-Gas Interaction	9
2.2	Ionosorption Model	14
2.3	Polycrystalline Thick Film Gas Sensors	17
2.4	Gas Selectivity	20
2.4.1	Additives and Surface Modification	21
2.4.2	Temperature Modulation	23
2.4.3	Electronic Nose	24
<b>3</b>	<b>One-Dimensional Nanostructures: Basic Principles and Gas Sensor Application</b>	<b>26</b>
3.1	Device Integration	26
3.2	Metal-Semiconductor (Nano-) Contacts	29
3.3	Gas Sensing Mechanism	33
3.4	Nanowire Gas Sensor Devices - Literature Review	37
<b>4</b>	<b>Synthesis of Metal Oxide Nanowires</b>	<b>41</b>
4.1	CuO Nanowires	43
4.1.1	Thermal Oxidation Growth Mechanism	43
4.1.2	Thermal Oxidation of Cu Wires by Resistive Heating	47
4.1.3	Thermal Oxidation of Electroplated Cu Structures	51
4.1.4	Thermal Oxidation of Evaporated Cu Structures	56
4.2	ZnO Nanowires	59
4.2.1	Growth Mechanisms	59
4.2.2	Vapor Phase Growth Using Zn Wires	62
4.2.3	Thermal Oxidation of Evaporated Zn Structures	66

<b>5 Gas Measurements: Methods and Target Gas Properties</b>	<b>70</b>
5.1 Gas Sensor Assembly	70
5.2 Gas Sensor Testing System	71
5.3 Properties of Selected Target Gases	72
5.3.1 Water Vapor H <sub>2</sub> O	72
5.3.2 Carbon Monoxide CO	73
5.3.3 Hydrogen Sulfide H <sub>2</sub> S	73
<b>6 Single Nanowire Devices</b>	<b>75</b>
6.1 Single CuO Nanowire Devices	75
6.1.1 Two-Point Configuration	75
6.1.2 Four-Point Configuration	79
6.1.3 Single Suspended CuO Nanowire	85
6.1.4 Discussion	88
6.2 Single ZnO Nanowire Devices	89
<b>7 Nanowire Array Devices</b>	<b>93</b>
7.1 CuO Nanowire Arrays: Thermal Oxidation of Electroplated Cu	93
7.2 CuO Nanowire Arrays: Thermal Oxidation of Evaporated Cu	97
7.3 ZnO Nanowire Arrays: Thermal Oxidation of Evaporated Zn	102
<b>8 CuO Nanowire Gas Sensors: Humidity Interference</b>	<b>107</b>
8.1 CO Sensing in Dry and Humid Atmosphere	107
8.2 H <sub>2</sub> S Sensing in Dry and Humid Atmosphere	109
<b>9 CuO Nanowire Integration on CMOS Microhotplates</b>	<b>117</b>
9.1 CMOS Microhotplates: General Description	117
9.2 CuO Nanowire Synthesis by Local Microhotplate Heating	119
9.3 Gas Sensing Results	121
<b>10 Outlook</b>	<b>122</b>
<b>11 Conclusion</b>	<b>125</b>

<b>References</b>	<b>129</b>
<b>List of Figures</b>	<b>156</b>
<b>List of Tables</b>	<b>158</b>
<b>Appendices</b>	<b>159</b>
<b>List of Publications</b>	
<b>Curriculum Vitae</b>	

# 1 Introduction

During the last decades, the demand for highly sensitive gas detecting devices has considerably increased. A large number of applications such as toxic gas alarms, smoke detectors or indoor air quality monitoring for heating, ventilation and air conditioning have created established as well as highly promising emerging markets [1]. Most importantly, atmospheric pollution caused by combustion of fossil fuels and emissions from industrial plants has become a major issue in modern urban societies. Considerable research effort is directed towards the development of inexpensive sensor technologies as replacements for conventional costly and time-consuming analytical techniques such as optical spectroscopy or gas chromatography. Miniaturized, high-performance gas sensor devices would allow widespread urban pollution monitoring, which is expected to result in significant societal impact in terms of advances in personal exposure assessment and improved understanding of atmospheric processes [2, 3].

The performance of gas sensing devices is most commonly evaluated according to the following parameters [4]:

*Sensitivity:* As the detection of low ppm-level concentrations of certain target gases is required in safety applications or industrial process control, high gas sensor sensitivity is of crucial importance.

*Selectivity:* The sensor device needs to be capable of distinguishing between several different target gases.

*Stability:* Long-term stability of the gas sensor response is essential for continuous monitoring of the surrounding gas atmosphere.

Moreover, fast sensor response and recovery times are necessary in several cases, in particular for toxic gas detection. Apart from these sensor related parameters, commercial factors often play a major role in practical applications such as low-cost, minimized power consumption or compatibility with standard semiconductor fabrication technology [5].



Considerable advances in gas sensor technology have been achieved resulting in different types of devices [4]:

- Conductometric sensors: Semiconducting metal oxides or polymers are employed in a resistive configuration. They change their electrical conductivity during gas exposure and are thus often termed chemiresistors.
- Field effect transistor (FET): The transfer characteristics depend on the surrounding gas atmosphere due to a gas-sensitive gate.
- Electrochemical sensors: The sensor response results from chemical reactions at the gas-sensitive interface of a working electrode and a solid electrolyte.
- Capacitive sensors: Absorption of gas molecules into the dielectric (most commonly polymers) of a capacitor results in changes of its electrical capacitance.
- Optical sensors: Gas-dependent optical properties are utilized for spectroscopic, surface plasmon resonance or ellipsometric measurements.
- Calorimetric sensors: These sensors make use of temperature changes that are caused by interactions of solid surfaces with gas molecules.
- Acoustic wave sensors: Adsorption of gas molecules on piezoelectric resonators leads to mass loading, which influences mechanical motion and is transduced in resonant frequency shifts.
- Cantilever-based sensors: Similar as in acoustic wave sensors, mass changes due to gas molecule adsorption result in frequency shifts of micromachined cantilever resonators.

Conductometric sensors are particularly interesting due to high sensitivity, low-cost and simplicity of the device configuration [5]. Commercial sensors are typically based on metal oxide thick films with polycrystalline structure, which are most commonly heated to elevated temperatures up to 400 °C.

However, state-of-the-art devices are rather dedicated to industrial use and do not fulfill requirements for consumer market applications. The development of CMOS compatible device fabrication technology is expected to pave the way for wide-spread gas sensor commercialization in the future [6].

Nanowire-based devices are a potential candidate for the realization of next-generation gas sensors because of several favorable properties [5, 7]. The schematic illustration in Fig.1.1 summarizes the most important aspects, which have to be considered in the gas sensing application.

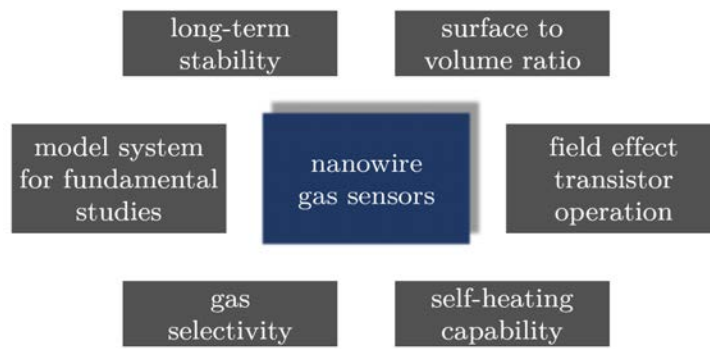


Figure 1.1: Important aspects of nanowire-based devices for the gas sensing application

In contrast to traditional polycrystalline gas sensors, which in many cases suffer from material instabilities due to grain growth by coalescence at elevated operation temperatures, nanowires provide superior long-term stability due to the high crystallinity and the lack of grain boundaries. In a comparative study,  $\text{SnO}_2$  nanowire networks showed excellent reproducibility of the gas response after 46 days of continuous sensor operation, whereas the sensing properties of  $\text{SnO}_2$  nanoparticle films changed considerably [8].

Furthermore, the small lateral dimensions of one-dimensional nanostructures are typically comparable with the Debye length of the material and are linked with a high surface to volume ratio. Therefore surface effects strongly influence the overall electronic properties leading to high sensor sensitivity. As a result, one-dimensional nanostructures are potential candidates for the realization of miniaturized devices with improved performance [7, 9].

Metal oxide nanowire gas sensors provide several opportunities for distinguishing different gas species as the main strategies in order to achieve gas selectivity have been adapted for nanowire-based devices. The surface of single as well as multiple metal oxide nanowire devices was modified by catalytic metal nanoparticles (typically Pd, Pt or Au) leading to superior gas sensing performance even at room temperature operation [10–13]. Increased gas selectivity can be also achieved by means of temperature modulation of metal oxide nanowire sensors realized on microhotplate devices [14, 15]. Moreover, nanowire-based devices have shown promising results for the realization of miniaturized electronic nose systems. In [16], individual nanowires of different metal oxide materials were used for the discrimination of hydrogen and carbon monoxide. A similar approach is reported in [17], where a sensor array of metal oxide nanowires and single-walled carbon nanotubes was able to distinguish between nitrogen dioxide, ethanol and hydrogen. Alternatively, SnO<sub>2</sub> nanowires decorated with different catalytic metals and operated at varying temperatures were successful in differentiating between hydrogen, carbon monoxide and ethylene [18]. Even a single SnO<sub>2</sub> nanobelt with longitudinal width variations and Pd functionalized segments was able to discriminate between vapors from various alcoholic beverages [19]. Most interestingly, also SnO<sub>2</sub> nanowire areal density differences in percolating networks exhibited specificity to the gas response towards carbon monoxide, ethanol and isopropanol. The discrimination power of the sensor device was attributed to statistical variations of signal contributions from two different transduction mechanisms (modulation of nanowire channel resistance and nanowire-nanowire junction barrier) [20]. Thus nanowire-based electronic noses do not only provide opportunities for considerable device miniaturization but also for novel sensing concepts due to the one-dimensionality of the employed nanostructures.

In addition, the free carrier concentration of nanowire-based devices can be controlled by means of field effect transistor operation, which provides another option for improving gas sensor performance and gas selectivity [21]. It was shown in [22] that oxidation and reduction reactions at the surface

of a single SnO<sub>2</sub> nanowire are influenced by applying different gate voltages. The authors of [23] reported on a ZnO nanowire field effect transistor with a room temperature gas response towards NO<sub>2</sub> and NH<sub>3</sub>, which was affected by gate-induced changes in carrier concentration. Furthermore, the nanowire sensor could be recovered by large negative gate voltages and the resulting potential for enhanced gas selectivity was indicated. In [15] the combined modulation of both operation temperature and gate voltage of a multiple SnO<sub>2</sub> nanowire sensor was successfully employed for the discrimination between three volatile organic compounds. Optimized gate voltage cycles lead to an increased recognition rate of 98% compared to 77% for a grounded backgate, which demonstrates the significance of field effect operation for selective gas detection.

Despite the fact that metal oxide semiconductor gas sensors have been used for several decades, detailed insights in surface chemistry and thus the underlying sensing mechanism are often limited [24–26]. Due to the simple geometry and the high crystallinity of single nanowire devices, gas sensitive effects are governed by a considerably lower number of parameters. In contrast to thin or thick film devices, the sensor response transients are not influenced by diffusion at intergrain boundaries, which allows to draw conclusions from response time constants on chemical to electrical transduction mechanisms [27, 28]. Long-term resistance drifts of single SnO<sub>2</sub> nanowires in different oxygen partial pressures were studied and due to the one-dimensional geometry new insights into the role of oxygen ion diffusion could be achieved [29]. Moreover, several literature reports indicate that experimental gas sensing results on single nanowire devices can be successfully correlated with quantum chemistry, in particular with density functional theory computations. In [30], theoretical calculations of gas adsorption on one-dimensional ZnO nanostructures were thoroughly reviewed. The authors of [31] interpreted experimental gas responses of individual CuO nanowires towards O<sub>2</sub>, NO<sub>2</sub> and ethanol by comparison with first-principles methods. In [32], the interaction of SnO<sub>2</sub> nanoribbons with O<sub>2</sub>, CO and NO<sub>2</sub> was studied by density functional theory calculations and confronted with exper-

imental data. Surface reactions of  $\text{NH}_3$  on  $\text{SnO}_2$  nanowires were investigated both theoretically and experimentally in [33] leading to an increased understanding of the underlying processes and humidity interference effects. As a consequence, nanowire-based gas sensing devices can be considered as excellent platform for fundamental studies of interaction mechanisms of metal oxides with gas molecules.

In conventional gas sensors, additional heating elements are most commonly employed in order to reach elevated device temperatures (typically up to  $400^\circ\text{C}$ ), which enhances chemical reactions at the metal oxide surface. However, external heaters are linked with an increase in both device complexity and power consumption. Single nanowire sensors provide an exceptional opportunity to overcome these disadvantages by utilizing the self-heating effect. The latter is based on Joule heat that is generated in a nanowire device operated under certain biasing conditions. Due to the weak thermal coupling of the nanowire to the substrate and the electrodes, heat losses are minimized. It was demonstrated that an increase of nanowire temperature can be indirectly observed by changes in surface reactivity and kinetics for different bias levels [34]. In [35], the effects of self-heating on single nanowire sensor response and recovery time were systematically investigated and the results were successfully correlated with measurements performed with external heating elements. Moreover, it was shown that self-heated nanowires may be operated in pulsed mode for improved gas selectivity [36]. The main advantage of utilizing Joule heating in single nanowire gas sensors is the exceedingly low power consumption of around few tens of  $\mu\text{W}$ , which makes such devices particularly interesting for portable devices. The authors of [37] combined a self-heated single nanowire gas sensor with a state-of-the-art energy harvesting device resulting in the successful demonstration of an autonomous gas sensor system.

Among the variety of target gases occurring in different practical sensing applications, the detection of carbon monoxide  $\text{CO}$  and hydrogen sulfide  $\text{H}_2\text{S}$  is of particular importance. These highly toxic gases both occur in

industrial processes and are thus relevant for occupational safety and health [38]. Furthermore, domestic CO exposure due to defect gas appliances is especially dangerous and has led to a large number of fatal accidents [39]. In addition, health effects because of constant environmental CO exposure in urban areas should not be underestimated [40]. Low concentrations of H<sub>2</sub>S may be released by geothermal sources or during bacterial breakdown of organic matter (e.g. swamps, sewers) and constant ppb-level exposure may result in chronic health effects [41].

Motivated by the high relevance of CO and H<sub>2</sub>S detection for practical applications, conductometric gas sensors based on cupric oxide (CuO) and zinc oxide (ZnO) nanowires are developed in this thesis. The gas sensing properties of n-type ZnO have been thoroughly investigated in literature and single [42–44] as well as multiple [45–47] nanowire sensor devices have been reported. Here, single ZnO nanowires are studied regarding a self-heated gas sensor operation, which is hardly explored for metal oxide materials other than SnO<sub>2</sub>. Furthermore, ZnO nanowire array devices fabricated by a thermal oxidation process are investigated as alternative to common vapor phase methods [48, 49], which require considerably higher nanowire synthesis temperatures. On the other hand, gas sensors based on the p-type metal oxide CuO are comparatively poorly studied [50]. The gas sensing properties of CuO nanowire based devices have been reported in single [31, 51, 52] and multiple [53–55] nanowire configurations and are further explored in this thesis. Apart from different realizations of single CuO nanowire sensors, a novel method for the fabrication of CuO nanowire arrays is presented, which allows efficient nanowire device integration. Moreover, the influence of humidity during CO and H<sub>2</sub>S exposure is studied, which has been scarcely investigated in literature.

Micromachined devices with integrated heating elements (typically termed microhotplates) have attracted considerable interest in the field of conductometric gas sensors due to their outstanding performance. In particular, the replacement of external heating elements is accompanied by a considerable

reduction of thermal time constants and power consumption [56]. In [57], literature results on MEMS microhotplates were summarized and it was emphasized that most of the reported fabrication processes are not compatible with standard CMOS technology. However, CMOS integration is considered as crucial step towards consumer market penetration of gas sensing devices due to the possibility of on-chip electronics and low-cost batch fabrication [58]. Here, the integration of CuO nanowires on CMOS microhotplates is demonstrated, which is a crucial step towards miniaturized smart gas sensor systems.

This thesis is organized as follows:

- Chapter 2 summarizes theoretical fundamentals and basic principles of conductometric gas sensors based on metal oxide semiconductors.
- Chapter 3 recapitulates literature reports on nanowire device integration, metal-semiconductor (nano-) contacts and nanowire gas sensors.
- Chapter 4 treats literature models for one-dimensional growth of CuO and ZnO nanowires as well as experimental synthesis results.
- Chapter 5 describes experimental gas measurement methods and summarizes the most basic target gas properties.
- Chapter 6 shows results on the fabrication, electrical characterization and gas sensing properties of single CuO and ZnO nanowire devices.
- Chapter 7 summarizes the most important findings on the gas sensing performance of CuO and ZnO nanowire array devices.
- Chapter 8 focuses on humidity interference effects using CuO nanowire devices for CO and H<sub>2</sub>S sensing in dry and humid atmosphere.
- Chapter 9 provides an overview of results on the integration of CuO nanowire devices on CMOS microhotplates.
- Chapter 10 describes potential future research directions in a short outlook.
- Chapter 11 gives a summary and a conclusion of the results achieved within this thesis.

## 2 Fundamentals of Metal Oxide Gas Sensors

After first scientific publications on the gas sensitivity of semiconducting metal oxides in the 1950's and 1960's, Taguchi succeeded in developing and commercializing an industrial gas sensor product around 1970. It was based on a  $\text{SnO}_2$  thick film deposited around a ceramic tube with a coiled heating wire inside. Over the last decades, various companies (Figaro, FIS, Applied Sensor, ...) have manufactured similar thick film based gas sensors using different metal oxide materials for various applications such as automotive cabin air intake, industrial process control or security devices for monitoring of explosive or toxic gases [59, 60].

In this chapter, the basic working principles of these devices are recapitulated by outlining the most important aspects of solid-gas interactions. Next, the ionosorption model is presented, which describes charge transfer between adsorbates and metal oxide surfaces. Moreover, the electrical and gas sensing properties of polycrystalline thick film sensors are summarized. Eventually, the most common strategies in order to obtain gas selectivity are reviewed.

### 2.1 Solid-Gas Interaction

In general, three different interaction mechanisms between a solid surface and gas molecules are possible [61] (see Fig.2.1):

- Physical adsorption (physisorption) relies on van der Waals dipole/dipole interactions and is thus characterized by weak, long-range forces. Physisorbed molecules are never dissociated and the physisorption enthalpy is typically about 0.2 eV/molecule [62].
- Chemical adsorption (chemisorption) is the formation of chemical bonds between gas molecules and solid surfaces which is accompanied by charge transfer. Most commonly, chemisorbed gas molecules are dissociated and



chemisorption enthalpy is considerably larger than in physisorption with values most commonly around 2 eV/molecule [63].

- Non-reversible reactions with the solid surface typically lead to the formation of new compounds. During gas sensor operation this type of interaction is usually not desired and avoided as far as possible.

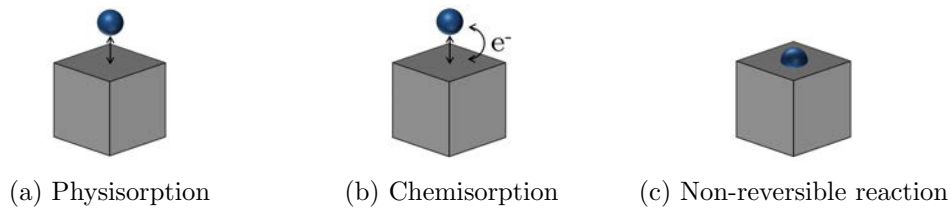


Figure 2.1: Interactions between solids and gas molecules (adapted from [61])

In the following, models describing surface coverages by physisorbed and chemisorbed molecules are presented in more detail. The coverage  $\Theta$  of solid surfaces by adsorbed molecules can be described by adsorption isotherms, i.e. the variation of  $\Theta$  as a function of partial pressure/concentration at a constant temperature.

A very simple model is given by the Langmuir isotherm, which is based on three assumptions: the coverage is well below a monolayer, all surface sites are equivalent and there is no interaction between adsorbed molecules.

In the case of non-dissociative adsorption, a rate equation for the surface coverage  $\Theta$  can be written as [64]

$$\frac{d\Theta}{dt} = k_{ads} (1 - \Theta) [C] - k_{des} \Theta$$

with rate constants for adsorption ( $k_{ads}$ ) and desorption ( $k_{des}$ ) and the concentration  $[C]$  of the adsorbed molecules in the gas phase. At equilibrium with a stationary coverage, the rate equation leads to the Langmuir isotherm

$$\Theta = \frac{K [C]}{1 + K [C]}$$

with the equilibrium constant  $K = k_{ads}/k_{des}$ .

For dissociative adsorption, the adsorption and desorption rates depend on the square of the vacant/occupied sites leading to the Langmuir isotherm for dissociative adsorption [64]

$$\Theta_d = \frac{(K [C])^{1/2}}{1 + (K [C])^{1/2}},$$

which is characterized by a weaker concentration dependence than in the case of non-dissociative adsorption.

In many cases the Langmuir isotherms are approximated by Henry's law for low adsorbate coverages [62]

$$\Theta_H = K [C]$$

with a simple proportionality relation between the concentration and the coverage. However, it has to be kept in mind that these simple models are often not able to describe experimental observations as the underlying assumptions are too simplistic, which will be discussed in detail later on. Alternatively, the Freundlich isotherm may be used for the estimation of surface coverages [63]

$$\Theta_F = c_1 [C]^{1/c_2}$$

with two constants  $c_1$  and  $c_2$ . In contrast to the Langmuir isotherm, surface sites are not considered independent and equivalent in this model. In addition, several different adsorption isotherm models can be found in [61].

The interactions between solid surfaces and gas molecules can be understood as a superposition of repulsive (interactions based on Coulomb's law and on the Pauli principle) and attractive (van der Waals interaction) forces. The Lennard-Jones potential is a widely used approximation for intermolecular interactions and is most commonly written as [63]

$$V(r) = 4 \epsilon \left\{ \left( \frac{r_0}{r} \right)^{12} - \left( \frac{r_0}{r} \right)^6 \right\}$$

with the intermolecular distance  $r$ , the parameter  $r_0$ , which is related to the value of  $r$  at the minimum of the function by  $r_{min} = 2^{1/6} r_0$ , and the parameter  $\epsilon$  equal to the minimum of the potential energy. Typical Lennard-Jones potentials for physisorption and chemisorption are shown in Fig.2.2.

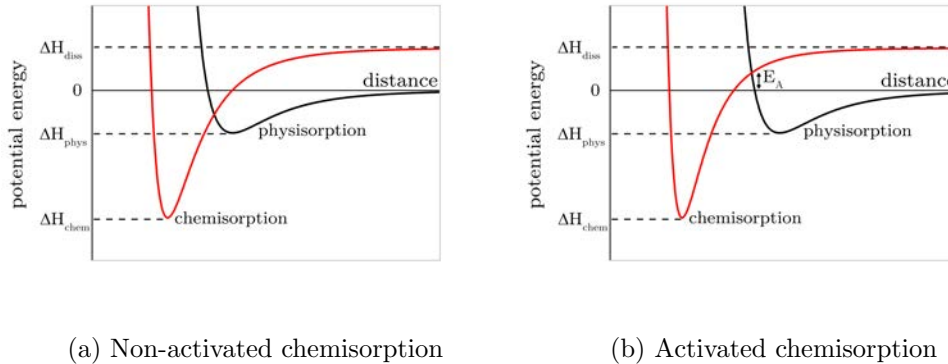


Figure 2.2: Lennard-Jones model for physisorption and chemisorption of a gas molecule (adapted from [4, 63, 65, 66])

In the case of physisorption, the energy of a gas molecule approaching a solid surface is lowered due to dipole-dipole interactions. Therefore it is an exothermic process with a small heat of adsorption corresponding to the van der Waals binding energy. In general, gas species are physisorbed at high coverages for low temperatures and at low coverages for high temperatures [65]. Chemisorption is most commonly accompanied by dissociation of the impinging gas molecules. In the Lennard-Jones model, the potential energy thus approaches the dissociation enthalpy  $\Delta H_{diss}$  at large distances. The minimum of the potential energy is considerably lower and typically occurs at smaller distances than for physisorption. Two different types of chemisorption can be distinguished: non-activated and activated chemisorption. The potential barrier between the physisorbed and the chemisorbed state can be identified as the difference between the intersection of the physisorption and the chemisorption curves and the minimum of the physisorption potential. In the non-activated case, this potential barrier is small and does not rise above the energy of a distant, stationary particle (zero potential energy in Fig.2.2). For activated chemisorption the physisorption and chemisorption

curves intersect at a positive energy  $E_A$ , which is usually referred to as activation energy [63]. In the following, emphasis will be put on activated chemisorption as it is widely used for the description of chemisorption of gas molecules on metal oxide semiconductors [4, 65, 66].

The potential energy curves of the Lennard-Jones model can be related to the rate constants for adsorption and desorption of chemisorbed molecules. Considering physisorption as a precursor state for chemisorption, the adsorption and desorption rate constants can be expressed as [4]

$$\begin{aligned} k_{ads} &= A e^{-E_A/kT} \\ k_{des} &= B e^{-(E_A+\Delta H_{chem})/kT}. \end{aligned}$$

In gas sensing experiments, energies for adsorption and desorption are typically provided thermally or by photon illumination. Assuming Henry's law, the equilibrium surface coverage of chemisorbed molecules can be written as

$$\Theta_H = \frac{A}{B} e^{\Delta H_{chem}/kT} [C],$$

which results in an exponential decrease of surface coverage with temperature. However, it cannot be generally assumed that the chemisorption enthalpy  $\Delta H_{chem}$  is independent of surface coverage. It typically decreases with increasing coverage, which can be explained by surface heterogeneity (high-energy sites are occupied first followed by low-energy ones), repulsion between adsorbates or surface charge induced band bending. In addition, the chemisorption activation energy most commonly increases with negatively charged molecules at the surface [4, 66].

The density of adsorbed gas molecules (often termed adsorption isobar) is shown in Fig.2.3. Equilibrium coverages for physisorption and chemisorption decrease exponentially with temperature, which can be understood within the Lennard-Jones model. However, for low temperatures the rates of chemisorption and especially desorption are very low so that equilibrium is not reached within realistic experimental time frames. This adsorption behavior is char-

acterized by irreversible chemisorption, which is qualitatively indicated by the dashed line in Fig.2.3. The maximum surface coverage occurs at an intermediate temperature  $T_{max}$  close to the equilibrium chemisorption regime [66].

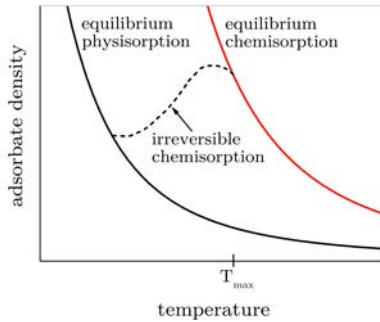


Figure 2.3: Density of adsorbed gas molecules (adapted from [65])

## 2.2 Ionosorption Model

As mentioned in the last chapter, the chemisorption of gas species is accompanied with charge transfer between adsorbent and adsorbate molecules. In this chapter, the resulting effects on the physical properties of the gas sensitive material, in particular the energy band structure, will be discussed. For this purpose, the ionosorption model [67–71] will be outlined, as it is the most widespread literature model explaining the gas sensing properties of metal oxide materials.

Depending on the sensor temperature (typical operation from 150-400 °C), oxygen chemisorbs at the surface as different ionic species  $O_2^-$ ,  $O^-$  or  $O^{2-}$  [68]. In the energy band representation, adsorbed oxygen can be described as extrinsic surface acceptor state, which may be negatively charged due to trapping of electrons. Consequently, a space charge layer is formed and the energy bands bend upwards. In the case of a n-type metal oxide (Fig.2.4a), the conduction band will be depleted of majority carriers and electron transport from the bulk to the surface is reduced due to the energy barrier  $eV_S$  [72]. For p-type materials (Fig.2.4b), electrons from the valence band are captured

on the surface trap leading to majority carrier accumulation. Due to the increased hole concentration, the electric resistance will decrease in the space charge layer [70]. The surface coverage with ionosorbed oxygen species is limited to  $10^{-3}$  -  $10^{-2}$  monolayers for n-type metal oxides, which is known as Weisz limit. Oxygen chemisorption on p-type materials is less explored, but considerably higher surface coverages were observed experimentally in this case which may be explained by ionization of lattice oxygen [62, 65].

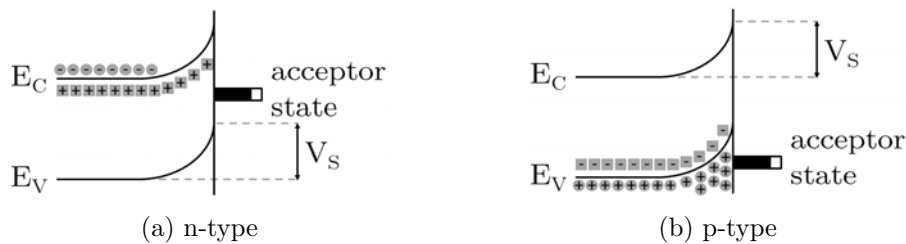


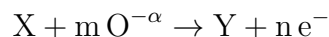
Figure 2.4: Surface band bending due to ionosorption of oxygen (adapted from [68, 70])

The width of the space charge region can be estimated using the Debye length [71]

$$L_D = \sqrt{\frac{kT\epsilon_r\epsilon_0}{q^2N}} . \quad (2.1)$$

The Debye length is influenced by the temperature  $T$ , the relative permittivity  $\epsilon_r$  and the density of majority carriers  $N$ . Thus it is a parameter influenced by material properties and by sensor operation conditions.

The interaction of metal oxide surfaces with reducing gases is typically described by a reaction with ionosorbed oxygen species. In many cases, only the atomic forms  $O^{-\alpha}$  ( $\alpha$  takes values of one or two depending on the ionisation state) are considered as they are more reactive than the molecular ion  $O_2^-$  [65]. The chemical reaction can be written in the general form [68, 73]



with the reacting target gas  $X$ ,  $m=1,2,\dots$  chemisorbed oxygen  $O^{-\alpha}$  ions, the reaction product  $Y$  and  $n=1,2,\dots$  electrons released into the material. After the reaction with reducing gases the occupation of the acceptor state

is changed and electrons are released into the material. On the other hand, oxidizing gases such as  $\text{NO}_2$  or  $\text{O}_3$  are typically chemisorbed on metal oxide surfaces acting as electron acceptors similar as in the case of  $\text{O}_2$  [74]. As a consequence, surface space charge and band bending are influenced by surface reactions [68]. In a conductometric gas sensor device these changes are transduced into electrical resistance signals, which will be described in the next chapter.

The reaction of gas molecules with ionosorbed species is most commonly described by two different mechanisms. In the Langmuir-Hinshelwood mechanism, co-adsorption of multiple molecular fragments on the metal oxide surface is required as the reaction takes place by encounters of adsorbed species. On the other hand, impinging gas molecules may collide and react with the adsorbate, which is termed Eley-Rideal mechanism. However, these two mechanisms should be regarded as ideal limits, because realistic surface reactions may involve both processes depending on the concentrations of the different species [63].

However, it has to be noted that the sensing mechanism of metal oxide gas sensors is still under debate. It was claimed that convincing spectroscopic evidence for the existence of chemisorbed  $\text{O}_2^-$ ,  $\text{O}^-$  and  $\text{O}^{2-}$  species are lacking under realistic sensor working conditions [24]. Alternatively, the oxygen-vacancy model can be found for the description of metal oxide gas sensor operation, which relies on the alternate reduction and re-oxidation of the surface (Mars-van Krevelen mechanism) [75, 76]. In this model, the sensor conductivity is controlled by the surface concentration of oxygen vacancies, which may be changed by reactions with gas molecules. A comparison of the ionosorption and the oxygen-vacancy model can be found in [77].

## 2.3 Polycrystalline Thick Film Gas Sensors

Conductometric sensor devices make use of electrical resistance changes of gas-sensitive materials in order to monitor the composition of the surrounding gas atmosphere. Based on the ionosorption model outlined in the last chapter, it will be described in the following how surface processes are transduced into electrical resistance changes in a typical gas sensor device. Emphasis will be put on the case of polycrystalline thick film sensors due to their widespread use in practical applications.

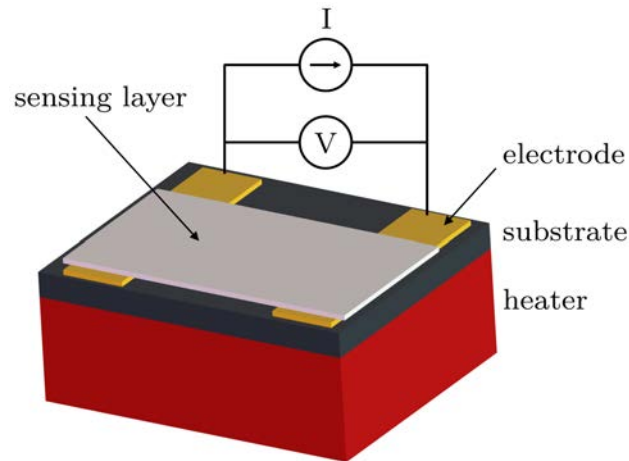


Figure 2.5: Schematics of a conductometric gas sensor based on a polycrystalline film

Most commonly, a chemiresistive gas sensor device consists of a substrate containing a gas-sensitive layer deposited over metal electrodes and a heater for operation at elevated temperatures (Fig.2.5). The electrical and gas sensing properties of the polycrystalline film strongly depend on its morphology and thus the used fabrication method. Typical conduction mechanisms are grain-boundary-controlled or neck-grain-boundary-controlled in porous thick film devices and surface-controlled in compact thin film devices. Depending on the crystallite grain size and the Debye length of the material the gas-sensitive layers may be partly or completely depleted/accumulated due to oxygen ionosorption at the surface [70]. In Fig.2.6, the sensor transduction mechanism of a grain-boundary-controlled porous thick film device is schematically depicted. Four adjacent, partly depleted/accumulated grains



are shown as representation of the gas-sensitive material between the electrodes. The surface space charge layers are indicated by the red shading and current transport is assumed in the horizontal direction.

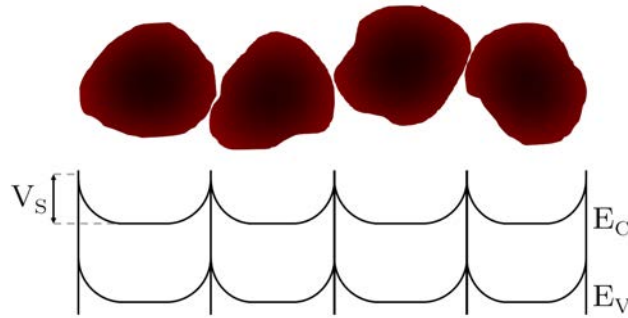


Figure 2.6: Conduction mechanism of a porous thick film gas sensor device. Electron transport and thus electrical resistance is determined by energy barriers at the interfaces of polycrystalline grains. The red shading indicates the surface space charge resulting from oxygen chemisorption. (adapted from [69])

Depending on the majority carrier type in the semiconducting metal oxide, the upward band bending is linked with a depletion (n-type) or an accumulation layer (p-type) at the grain surface. The electrical resistance of a gas-sensitive layer with n-type conductivity is proportional to [71]

$$R \sim e^{qV_S/kT} ,$$

whereas in the case of p-type conductivity it can be approximated by [78]

$$R \sim e^{-qV_S/2kT} .$$

As can be seen, changes in the band bending  $V_S$  due to gas reactions at the surface are transduced differently into electrical signals when comparing n-type and p-type materials. During exposure to reducing gases the resistance of n-type metal oxides decreases, whereas the resistance of a p-type material increases. On the other hand, during exposure to oxidizing gases the resistance of n-type metal oxides increases, but the resistance of p-type materials decreases. As can be easily derived from the equations above, the sensor response, i.e. the ratio of resistance values in air and in presence of the

target gas, is described by exponential functions of surface potential changes  $\Delta V_S$ . The exponents differ by a factor of two for n-type and p-type materials due to different conduction mechanisms [78].

Numerous metal oxides have been investigated regarding an application in gas-sensitive devices. The different material and gas sensing properties were extensively reviewed in [79] and different material deposition techniques suitable for the realization of nanocrystalline metal oxide films were summarized in [80]. Most commonly, metal oxide based gas sensors share several similar characteristics. A considerable increase in gas sensor response is observed for decreasing grain sizes approaching twice the Debye length of the material. In the case of such small nanocrystals it is expected that the gas-dependent surface space charge influences the electrical properties of the whole grain resulting in maximized sensor responses [81]. The concentration dependence of the sensor response  $S$  typically follows a power law of the form

$$S = K [C]^n$$

with a constant  $K$ , the concentration  $[C]$  of a certain target gas and a characteristic exponent  $n$ . Different values of  $n$  were found for various gas species and a theoretical explanation based on the ionosorption model was proposed [73]. Furthermore, a bell-shaped temperature dependence of the gas sensor response is most commonly observed experimentally with a distinct maximum depending on the adsorbate/adsorbent system and the target gas concentration. For conventional thick film devices, the decrease of sensor response at high temperatures was explained by gas diffusion into the porous material (see for instance [82]). During the diffusion of reactive gas molecules into the porous, polycrystalline thick film structure, they are partially consumed because of reactions on the metal oxide grain surfaces. This leads to a decrease of gas concentration along the diffusion path and thus to a lower gas response of the bottom layers of the thick film. Although this model was successful in describing several experimental observations, it is, however, not able to explain the sensing characteristics of thin film sensors [83] and single

nanowire devices [35,84], where similar bell-shaped response curves have also been observed for different operation temperatures.

Alternative models explained the experimentally observed sensor response curves in terms of rate equation approaches, which emphasize the temperature dependence of different surface processes such as adsorption, desorption or molecule dissociation. The sensing behavior can be qualitatively understood by considering the temperature dependence of the Langmuir isobar and the probability for an activated surface reaction (see Fig.2.7). The low temperature increase of the gas response is caused by the exponential increase of the probability for an activated surface reaction (Arrhenius-type), whereas the high temperature decrease results from a lower surface coverage with target gas molecules [85, 86].

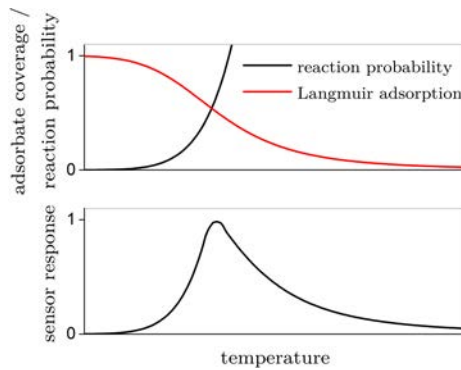


Figure 2.7: Temperature dependence of the Langmuir isotherm and of the activated surface reaction probability resulting in a bell-shaped sensor response (adapted from [85])

## 2.4 Gas Selectivity

In the majority of practical applications a mixture of multiple gas species is present and selective sensor responses to certain target gases are desired. However, metal oxides typically show considerable cross-sensitivities and thus their ability to distinguish between different gases is very limited. In order to remedy this shortcoming various methods have been thoroughly investigated and it has been demonstrated that a certain degree of gas selectivity can be

achieved by different approaches (see [87] and references therein). For instance, passive filters (reducing the gas penetration of certain gas molecules) and active filters (enabling catalytic decomposition of certain gas molecules) have been successfully employed either in the sensor packaging or as porous surface layer on the metal oxide sensing film. Another promising example is the integration of non-selective sensors with microfabricated gas chromatographic columns. In this case gas species may be distinguished due to their temporal separation at the column outlet. However, the most widespread techniques to achieve selectivity in metal oxide gas sensors are surface modification, temperature modulation and electronic nose arrays, which will be described in more detail in the following.

#### **2.4.1 Additives and Surface Modification**

The introduction of additives has proven to be an efficient method for the optimization of gas sensing properties of metal oxide materials. Please note that this approach is often referred to as 'doping' in gas sensing literature although it is in most cases not comparable to doping of semiconductors in microelectronic industry, where considerably lower dopant concentrations and different process technologies are employed. Various methods have been proposed for the preparation of multi-component gas sensor materials: additives can be incorporated during materials synthesis (e.g. in sol-gel or spray pyrolysis processes), introduced by impregnation of porous sensing layers or added by physical vapor deposition on the sensor surface [88, 89]. Numerous parameters of metal oxides such as grain size, stability, stoichiometry or porosity may be influenced by additive materials [83].

Here, emphasis will be put on catalytic additives on metal oxide surfaces, as this is the most relevant case for nanowire-based devices. Nanoparticles of noble metals such as Pd, Pt, Ag or Au are most commonly used for selectivity enhancement, although in some cases surface modification with another metal oxide leads to favorable sensing properties. Typically, the introduction of these nanoclusters is accompanied by increased sensitivity

and decreased response/recovery times, while it allows a reduction of sensor operation temperature at the same time. The influence of the surface additive is described by two major processes, i.e. chemical and electronic interaction [10,90]. These mechanisms are schematically illustrated in Fig.2.8:

- Chemical interaction (see Fig.2.8a) represents the enhanced dissociation of impinging gas molecules  $A_2$  on catalytic nanoclusters (typically Pt or Au). The resulting molecular fragments A are spilled over onto the metal oxide support, where they react with chemisorbed oxygen species. A typical example is the dissociation of molecular hydrogen  $H_2$  on Pt nanoparticles. However, the spillover effect also leads to enhanced dissociation of molecular oxygen  $O_2$  causing an increased concentration of reactive oxygen ions in the vicinity of the catalytic nanocluster (often termed spillover zone). Furthermore, a reverse spillover effect may occur, which means that mobile species, which are physisorbed on the metal oxide surface, diffuse to the catalytic nanoparticle where they are dissociated.
- Electronic interaction is characterized by electron exchange between the metal oxide and the surface additive (see Fig.2.8b). A space charge layer depleted of electrons is formed in the metal oxide near the interface. If the surface additive reacts with a reducing analyte, electrons are released into the metal oxide leading to a modulation of its conductance. Electronic interaction has been observed for instance in PdO/Pd, AgO/Ag or CuO/Cu nanoparticles on  $SnO_2$  surfaces [91].

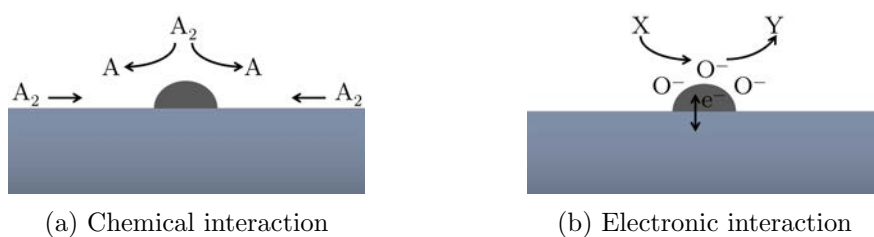


Figure 2.8: Interaction between metal oxides and surface additives (adapted from [10,90])

## 2.4.2 Temperature Modulation

As the gas response of metal oxide sensors typically shows a specific temperature dependence for different target analytes (see Chapter 2.3), temperature modulation is a promising strategy in order to achieve a certain degree of gas selectivity. Several different dynamic operation modes have been reported. Fast heating pulses can be utilized in order to observe characteristic gas-dependent features in the transient sensor response. Alternatively, different periodically oscillating waveforms (for example staircase, sinusoidal, triangular etc.) may be applied to the heater (Fig.2.9). In some cases simple mathematical operations such as curve fitting or fast Fourier transform are sufficient in order to enhance the gas discrimination power of the sensor device [92].

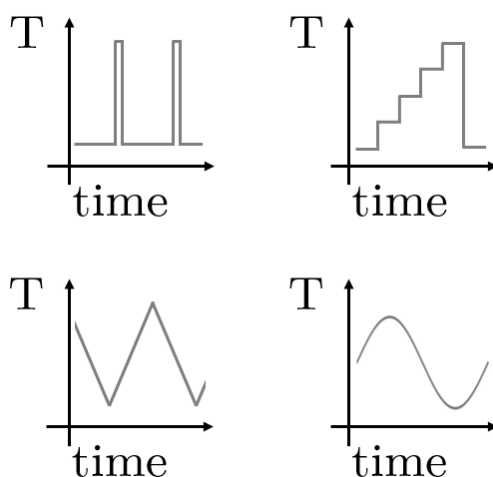


Figure 2.9: Typical waveforms of temperature modulated gas sensors

A typical example for selectivity enhancement can be found in [93], where different temperature modulation techniques were compared for the classification of ethanol and other volatile organic compounds. Although the fast temperature transients complicate the theoretical description of the sensing mechanism, considerable advances have been made in modeling the sensor response of temperature modulated gas sensors [94–97]. More recently, various sophisticated methods were successfully employed for the optimization

of analyte discrimination by sensor temperature modulation. Among others, selection of optimal modulation frequencies by multi-level pseudo-random heating sequences [98], determination of optimal operation temperature by mutual information in a sensor array [99] or self-adapted temperature modulation [100] can be considered as representative examples. An exhaustive review on dynamic sensor operation and the associated feature extraction can be found in [101].

### 2.4.3 Electronic Nose

Mammalian olfaction has inspired researchers to the development of chemical sensor systems relying on similar working principles. In the nasal cavity millions of olfactory receptors detect the various impinging gas molecules in a non-selective way, which means that the identification of a specific chemical species is not based on a single type of receptor. Instead, the response pattern of an array of multiple different receptors is utilized and odors are identified by their characteristic response "fingerprints" [102].

In electronic noses this manner of identifying chemical species is mimicked by an array of chemical sensors connected to readout circuitry followed by extensive data analysis. A large number of mathematical methods for pattern recognition is available and successfully employed. Functional sensor systems have been realized using different gas sensor technologies (for instance metal oxide semiconductors, field effect transistors, chemocapacitors, optical sensors, conductive polymers, acoustic wave devices or electrochemical sensors) and device architectures [103].

Although gas sensor systems based on electronic noses are commercially available, their applications in daily life are typically restricted due to their bulky size and high price [104]. Nevertheless this approach can be considered as powerful gas sensing technique due to various advantages, for instance rapid detection, ability of continuous, real-time operation and similar discrimination power for pure chemical species and complex odors [87]. The feasibility

of using electronic noses has been demonstrated in various practical applications such as food quality control [105], explosives detection [106] or drug identification [107]. The optimum number of sensor elements and the ideal transducer technology may be different from one application to another and discrimination power does not necessarily rise with increasing number of employed sensor elements. Apart from detrimental properties specific for the used gas sensor technology, electronic noses suffer from disadvantages such as lack of absolute calibrations, necessity of application-specific method development and lack of sensitivity in the presence of high concentrations of a single component [87].

For the reduction of size and cost of electronic nose systems, CMOS integration of gas sensing devices is of crucial importance as it allows the fabrication of miniaturized sensor arrays, electronic interfaces and pattern recognition engines on a single chip. Due to the broad functionality such devices are most commonly termed System on Chip (SoC) solutions (see Fig.2.10 for a schematic illustration). The remarkable performance of sensor arrays in combination with integrated circuitry fabricated in CMOS technology has been demonstrated in [80,108], for instance. Therefore SoC approaches are promising candidates for the realization of highly integrated, miniaturized, fast and inexpensive gas sensor systems [104].

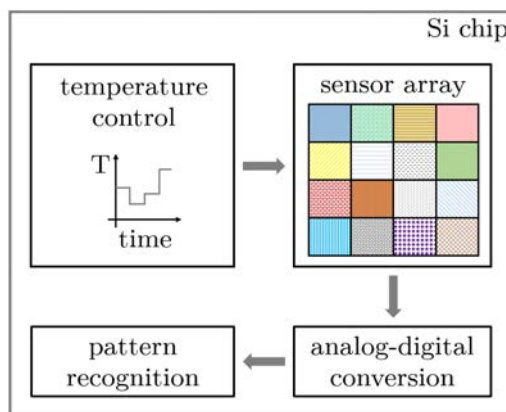


Figure 2.10: Schematics of a System on Chip electronic nose device (adapted from [80,104])



## 3 One-Dimensional Nanostructures: Basic Principles and Gas Sensor Application

### 3.1 Device Integration

In order to enable large-scale, industrial applications of nanowire devices, reaching from field-effect transistors to optoelectronic devices or chemical sensors, reliable and reproducible nanowire device integration is of crucial importance. Nanowire integration with standard CMOS technology is particularly interesting, as it may lead to increased functionality and superior performance in combination with low-cost batch fabrication. However, various aspects have to be considered for successful nanowire device implementation [109]:

- Nanowire growth control: position, diameter, morphology, doping ...
- Reliable nanowire contacts
- Thermal budget (above 1000 °C for CMOS front-end-of-line; around 400 °C for CMOS back-end-of-line)
- Material (in)compatibilities (e.g. Au catalyst)
- Variability in device fabrication

In general, two different paradigms are distinguished in nanowire fabrication, i.e. the top-down and the bottom-up paradigm [110]. Top-down fabrication involves processes for structure formation by material removal from a larger piece, whereas bottom-up fabrication comprises structure formation by assembly of smaller components (Fig.3.1).

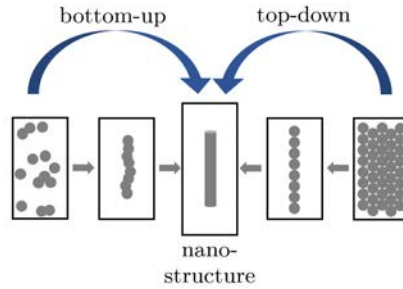


Figure 3.1: Top-down and bottom-up paradigms for nanostructure synthesis

In the following, emphasis will be put on methods for integration of nanowires synthesized by the bottom-up paradigm, as the majority of nanowire gas sensing devices in literature were realized by this approach. In this case two main strategies are typically used for nanowire device integration [109]:

The first strategy relies on nanowire synthesis on a growth substrate and a nanowire transfer step to another substrate, where the functional device is subsequently fabricated. The nanowires are typically suspended in a liquid, which is spin-coated or drop-coated on the device substrate. Alternatively, mechanical transfer can be used to deposit nanowires on the desired substrate. Next, the randomly dispersed nanowires are most commonly contacted by focused ion beam assisted metal deposition or lift off processes. When using this approach, challenges like sample to sample variation or intricate fabrication of reliable nanowire contacts have to be faced [111]. However, several methods have been developed in order to optimize this nanowire integration scheme. Non-uniform electric fields between pre-patterned metal electrodes can be used to exert dielectrophoretic forces on nanowires in a liquid, which allows to place them between the two electrodes [112–114]. Multiple parameters can be adjusted in a dielectrophoresis process, for instance gap geometry, DC electric field, AC electric field, frequency, flow conditions etc. By balancing surface, hydrodynamic and dielectrophoretic forces, the authors of [115] were able to show that single nanowires can be assembled with a yield of 98.5% over 16 000 electrodes demonstrating the tremendous potential of this technique. Another very promising nanowire device integration technique is contact printing from flat or cylindrical nanowire growth

substrates. This method makes use of shear forces during mechanical contact leading to parallel nanowire alignment. The printing process can be further optimized by assistance of a lubricant for reduced nanowire breakage or receiver substrate surface modification for controlling nanowire density and patterned nanowire transfer. The main advantages of this method are versatility, scalability and high nanowire areal density (see [116] for an extensive review). Recently, a specific printing process, which was termed 'nanoscale combing' by the authors of [117], yielded arrays with more than 98.5% of the nanowires aligned to within an angle of  $\pm 1^\circ$ . Furthermore, several other methods have been developed such as optical trapping [118], template guided assembly [119], flow-assisted alignment, bubble blown techniques and Langmuir-Blodgett techniques (see [120] for further references).

The second strategy is based on nanowire growth directly on the device substrate. Most importantly, this nanowire integration scheme does not require nanowire transfer between different substrates, which eliminates a certain amount of randomness inherent to this process step. Various literature results show efficient nanowire integration by this method. In [121], the fabrication of vertical, wrap-gated nanowire field effect transistors was demonstrated. Nanowire logic gates and photovoltaic devices were fabricated by directly integrating nanowires with different doping levels along their axes realized by modifying the precursor gas during vapor-liquid-solid growth [122]. Moreover, large-scale synthesis of GaAs/InGaP core/shell nanowires was achieved on Si substrates resulting in vertical light emitting diodes [123]. These exemplary literature reports do not only validate the effectiveness of the on-chip nanowire synthesis integration scheme, but also indicate the enormous versatility of this method.

In the field of nanowire gas sensors, various authors report on optimized nanowire device integration methods. In [124], the fabrication of highly sensitive NO<sub>2</sub> sensors by printing highly ordered Si nanowires on a plastic substrate was reported. The authors of [114] used dielectrophoresis in order to align nanowires between prepatterned electrodes, which resulted in

a conductometric gas sensors for volatile organic compounds. Several groups have demonstrated the integration of SnO<sub>2</sub> nanowires by VLS growth between prepatterned Au catalysts resulting in an electrical connection between adjacent electrodes [125–129]. A different integration scheme was proposed in [130], where a sacrificial SiO<sub>2</sub> layer was used for patterning of a VLS grown SnO<sub>2</sub> nanowire film. ZnO nanowires have been directly integrated by VLS growth between adjacent contact pads using Au [131, 132] or ZnO:Ga [45, 46] catalysts. Alternatively, ZnO nanowires can be synthesized on the gas sensing device substrate by low temperature hydrothermal methods [133, 134], which was also successfully demonstrated on SOI CMOS microhotplates [47].

### 3.2 Metal-Semiconductor (Nano-) Contacts

For the realization of functional semiconductor devices their electrical connection to external circuitry by a contact metallization is of crucial importance. The basic principles of metal-semiconductor contacts will be summarized in this chapter in order to gain an understanding of the resulting electrical properties. Eventually, particularities of contacts to nanomaterials regarding technological aspects and physical characteristics will be discussed.

The electrical properties of metal-semiconductor contacts are typically described by energy band diagrams. In Fig.3.2, the band structures of a metal and a semiconductor, which are not in contact with each other, are shown. The work function for the metal  $\Phi_M$  and for the semiconductor  $\Phi_S$  is defined as energy difference between the Fermi level and the vacuum level. For the semiconductor, the electron affinity  $\chi_S$  denotes the energy difference between the bottom of the conduction band and the vacuum level. The band gap energy  $E_G$  is determined by the difference between the bottom of the conduction band and the top of the valence band [135].

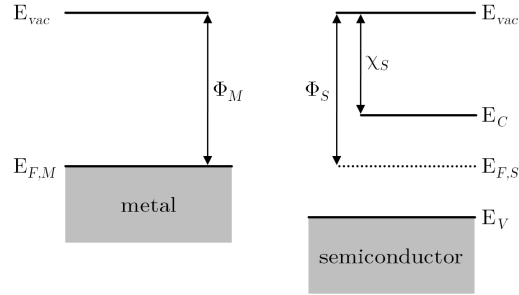


Figure 3.2: Energy band diagrams of metals and semiconductors (adapted from [135])

For ideal Schottky contacts, four different possibilities can be distinguished depending on the semiconductor majority carrier type (n-type or p-type) and the difference between the work functions of the metal and the semiconductor (see Fig.3.3 and Fig.3.4). In any case, electrical charges will be transferred from one material to the other until the Fermi levels are aligned. The resulting space charge is screened within few Ångstrom in the metal, whereas the space charge region may extend hundreds of Ångstrom into the semiconductor due to the lower concentration of free carriers [136].

In the case of a metal contact to a p-type semiconductor, the conduction of holes in the valence band is significant for the electrical properties. If the work function of the metal  $\Phi_M$  is smaller than that of the semiconductor  $\Phi_S$  (see Fig.3.3a), electrons will flow from the metal to the semiconductor until the Fermi levels are lined up. As a consequence, the energy bands in the p-type semiconductor bend downwards resulting in a Schottky barrier at the interface of  $\phi_B = E_G - (\Phi_M - \chi_S)$ . The difference of work functions is termed contact potential  $\phi_C = \Phi_M - \Phi_S$  [137]. For the case of  $\Phi_M > \Phi_S$  (see Fig.3.3b), electrons will flow from the semiconductor to the metal leading to an upward band bending. Thus there is no potential barrier for hole transport and an Ohmic contact is formed.

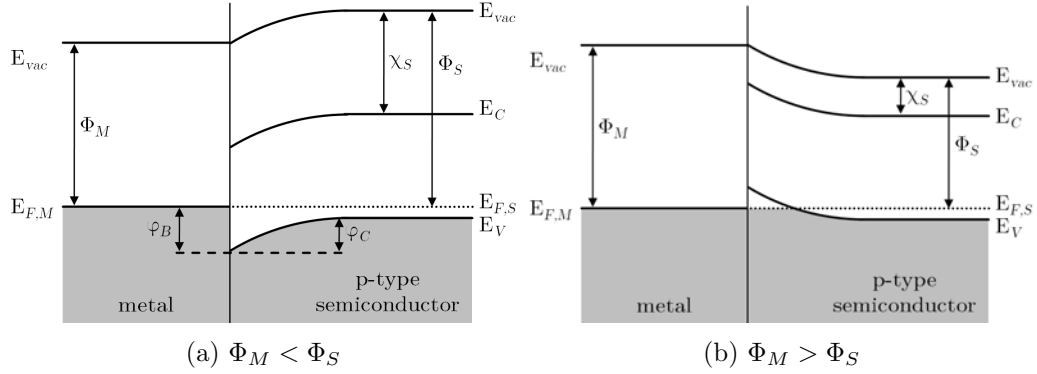


Figure 3.3: Metal contacts to p-type semiconductors (adapted from [135,137–139])

For n-type semiconductors a potential barrier  $\phi_B = \Phi_M - \chi_S$  for electrons is formed if the metal work function  $\Phi_M$  is larger than the work function of the semiconductor  $\Phi_S$  (Fig.3.4a). The opposite case of  $\Phi_M < \Phi_S$  (Fig.3.4b) leads to the formation of an Ohmic contact [138].

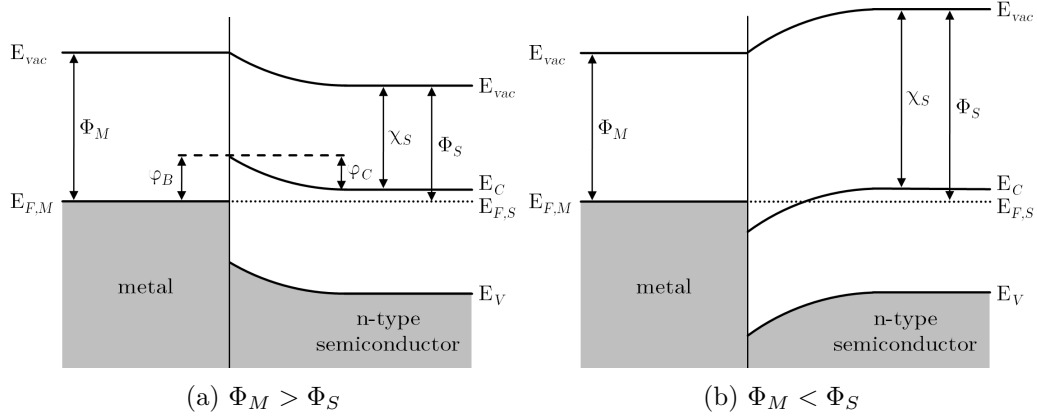


Figure 3.4: Metal contacts to n-type semiconductors (adapted from [135,137–139])

The width of the space charge region  $W$  can be estimated using the one-dimensional Poisson equation in a abrupt junction approximation as [138]

$$W = \sqrt{\frac{2\epsilon_r\epsilon_0(\phi_C - V)}{qN_D}}$$

with the contact potential  $\phi_C$ , the applied voltage  $V$ , the relative permittivity  $\epsilon_r$  and the dopant density  $N_D$ .

However, a large number of experimental findings does not support this simple picture of Schottky contact formation. In most practical realizations of metal-semiconductor junctions deviations from this idealized model will arise due to an interface layer or the influence of surface and interface states [137]. In the energy band diagram formalism, surface states are described as donor or acceptor states in the band gap and lead to bending of the valence and conduction band near semiconductor surfaces. In case of a Schottky contact with a metal layer the intrinsic surface states of the semiconductor are influenced by a variety of factors (formation of metal-induced gap states, chemical reactions, interdiffusion, structural changes) [136]. The states in the band gap at the metal semiconductor junction are termed interface states and may determine the contact properties to a large extent. For high densities of interface states the semiconductor Fermi level is pinned near the neutral level, which separates acceptor states (above the neutral level; neutral when empty, negatively charged when occupied) and donor states (below the neutral level; positively charged when empty, neutral when occupied). As a consequence, the Schottky barrier height is determined by the neutral level and thus semiconductor surface properties rather than the difference of metal work function and semiconductor electron affinity [137].

In many cases, established models of electrical contacts to bulk materials cannot be applied at nanoscale dimensions. Existing concepts have to be adapted due to differences between bulk materials and nanostructures regarding electrostatics and contact geometry. In bulk contacts high doping levels may be employed at the semiconductor interface in order to obtain Ohmic contacts relying on tunneling through the Schottky barrier. However, this strategy is not feasible for nanowires with small diameters due to weak surface band bending. Furthermore, it has been shown theoretically for the case of nanowires and nanotubes that interface states have a weaker influence on band alignment being in agreement with experimental findings [140]. Moreover, the estimated width of the space charge region  $W$  may differ from the bulk model in the case of one-dimensional nanostructures. For very small cross-sections and low or moderate doping levels a diameter dependence of

$W$  was suggested, which plays an important role in the charge transport processes at the interface [141].

The reproducible fabrication of contacts to one-dimensional nanostructures with well-defined electrical characteristics often remains a major challenge. For instance, the electrical device characteristics of GaN nanowires,  $\text{In}_2\text{O}_3$  nanowires and carbon nanotubes contacted in two-point and four-point configurations were extensively characterized in [142]. The impact of lithography technology (photolithography versus electron beam lithography), oxygen plasma treatment and thermal annealing were systematically investigated. It was suggested that electron beam exposure causes nanowire surface damage leading to Fermi level pinning, which was not observed for photolithographically fabricated devices. Nanocontact properties are thus strongly influenced by the used fabrication technology and re-evaluation of processes developed for bulk devices is often necessary due to the small volume and the large surface to volume ratio of the employed nanostructures [141].

### 3.3 Gas Sensing Mechanism

As already outlined in Chapter 2.2, common literature models for metal oxide gas sensors are based on the interaction between the surrounding gas molecules and ionosorbed oxygen species at the sensor surface. The gas sensing mechanism of nanowire based sensors can be described by a similar approach, but some adaptations have to be made due to the quasi one-dimensional sensing elements. In the following, the influence of surface charges on the carrier concentration in p-type and n-type metal oxide nanowires is illustrated. Moreover, different contributions to the sensor response in nanowire networks are described. Eventually, a different sensing principle based on Schottky contacts is discussed.



Space charge effects due to reactive surface species can be described by the Poisson equation [62], which may be expressed in cylindrical coordinates:

$$\frac{1}{r} \frac{\partial}{\partial r} \left( r \frac{\partial V}{\partial r} \right) + \frac{1}{r^2} \frac{\partial^2 V}{\partial \phi^2} + \frac{\partial^2 V}{\partial z^2} = - \frac{\rho}{\epsilon_r \epsilon_0} .$$

For the case of an infinitely long nanowire which is totally surrounded by the gas atmosphere (no substrate influence), the potential  $V$  is independent of the angle  $\phi$  and the  $z$ -coordinate. Consequently, the Poisson equation reduces to:

$$\frac{\partial^2 V}{\partial r^2} + \frac{1}{r} \frac{\partial V}{\partial r} = - \frac{\rho}{\epsilon_r \epsilon_0} .$$

In the following, acceptors/donors are assumed to be fully ionized and the concentration of free holes/electrons is approximated by a Boltzmann distribution. In oxygen atmosphere p-type metal oxide semiconductors (for instance CuO, NiO or Cr<sub>2</sub>O<sub>3</sub>) form a surface accumulation layer. When neglecting the contribution of ionized donors and free electrons to the charge density  $\rho$ , the Poisson equation leads to [62]:

$$\frac{\partial^2 V(r)}{\partial r^2} + \frac{1}{r} \frac{\partial V(r)}{\partial r} = \frac{qN_A}{\epsilon_r \epsilon_0} \left( e^{\frac{qV(r)}{kT}} - 1 \right) .$$

On the contrary, oxygen ionosorption leads to a depletion layer at the surface of n-type metal oxides such as SnO<sub>2</sub>, ZnO or In<sub>2</sub>O<sub>3</sub> and the potential can be found from (acceptors and free holes neglected) [62]:

$$\frac{\partial^2 V(r)}{\partial r^2} + \frac{1}{r} \frac{\partial V(r)}{\partial r} = \frac{qN_D}{\epsilon_r \epsilon_0} \left( 1 - e^{-\frac{qV(r)}{kT}} \right) .$$

These non-linear, second order differential equations can be solved numerically using two boundary conditions. Radial symmetry leads to a vanishing electric field  $E = -\frac{\partial V(r)}{\partial r}$  in the center of the nanowire ( $r = 0$ ). At the surface either the potential or the charge density (using the Gauss relation) can be used as boundary condition. Typical solutions are schematically shown in Fig.3.5 for p-type and n-type metal oxides. The majority carrier concentration  $N(r)$  is inhomogeneous across the nanowire diameter and is directly

linked to the nanowire conductivity by

$$G = qN(r)\mu\frac{D^2\pi}{4L}$$

with the mobility  $\mu$  and the nanowire diameter  $D$  and length  $L$ . As in the case of polycrystalline metal oxide gas sensors, gas molecules may react with ionosorbed oxygen species. This induces a change of surface band bending, which results in a variation of nanowire conductivity. For n-type semiconductors the inhomogeneous carrier concentration is often approximated in literature by a fully depleted space charge region leading to a conducting channel with reduced diameter  $D - 2W$  [16, 20].

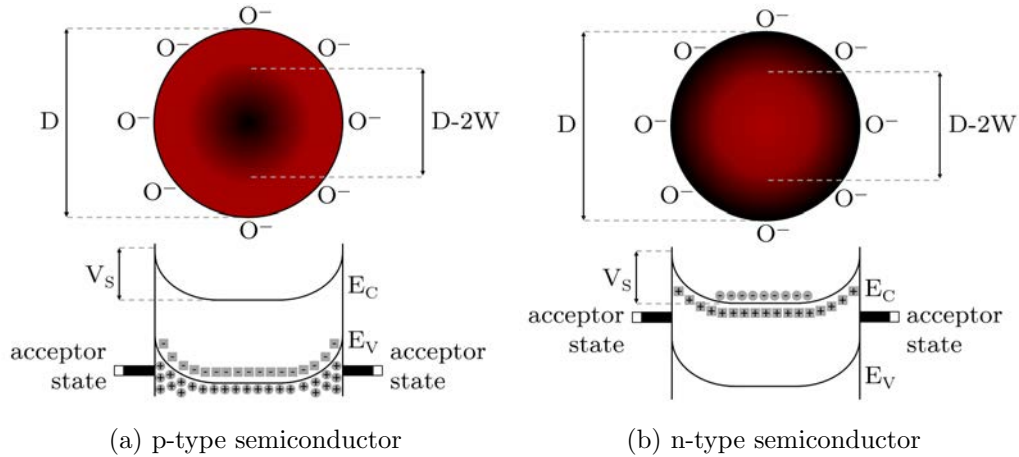


Figure 3.5: Band bending at metal oxide nanowire surfaces

In sensors based on nanowire networks two different contributions are most commonly responsible for the gas response. First of all, nanowire specific conductivity depends on the coverage with ionosorbed oxygen species and the resulting surface band bending, as described above. In addition, gas-sensitive effects on the carrier transport across nanowire-nanowire junctions have to be considered. A schematic illustration can be found in Fig.3.6, where the junction potential barrier is indicated and the inhomogeneous carrier density is represented by the black shading. The current across these junctions can be described by thermionic emission theory and is exponentially dependent on gas-induced changes of the surface band bending [8, 132].

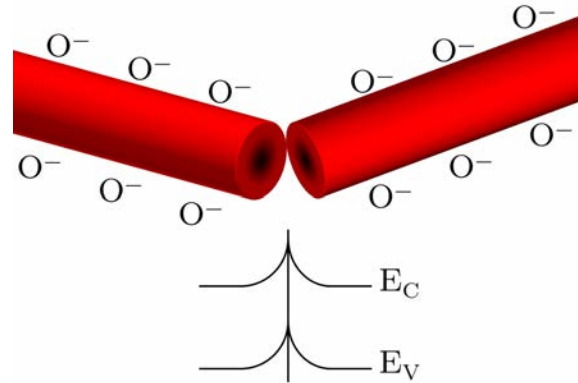


Figure 3.6: Sensor response in nanowire networks (adapted from [8])

Another working principle of nanowire-based gas sensors is based on Schottky contacts. The current passing through the rectifying metal semiconductor junction can be described by thermionic-emission theory (forward bias) and thermionic-emission-diffusion theory (reverse bias). Most importantly, the height and the width of the Schottky barrier is very sensitive to the gaseous environment. Due to the different transduction mechanism considerably increased sensor responses were achieved compared to Ohmic contact devices [143].

### 3.4 Nanowire Gas Sensor Devices - Literature Review

One-dimensional nanostructures have been extensively employed in chemical sensing using a variety of different configurations, such as chemiresistors, field effect transistors, gas ionization sensors, quartz crystal microbalances, surface acoustic wave devices or optical sensors. Depending on the sensing principle different materials have been employed ranging from metals to semiconductors and conducting polymers [144, 145].

Here, focus will be put on conductometric gas sensors based on nanowire networks and single nanowire devices including field effect transistor configurations. Most commonly, semiconducting metal oxides are employed and in some cases surface additives are utilized in order to modify the sensor response, as already mentioned above. Literature reports on nanowire gas sensor devices are summarized in Table 3.1 with an emphasis on five target gases relevant for environmental monitoring (carbon monoxide CO, ammonia NH<sub>3</sub>, nitrogen dioxide NO<sub>2</sub>, hydrogen sulfide H<sub>2</sub>S) and indoor air quality control (ethanol C<sub>2</sub>H<sub>5</sub>OH). From these results it can be seen that metal oxide nanowire based sensors show high sensitivity with detection limits in the ppm or even sub-ppm concentration range. However, the similar results for the different materials and target gases clearly illustrate the lack of selectivity of these devices.

<i>Material</i>	<i>Device</i>	<i>Target gas</i>	<i>Conc.</i> [ppm]	<i>Temp.</i> [°C]	<i>Ref.</i>
SnO <sub>2</sub>	single	CO	5-1000	295	[146]
SnO <sub>2</sub>	network	CO	0.5-10	307	[20]
SnO <sub>2</sub>	single	CO	25-100	100-300	[14]
SnO <sub>2</sub>	single	NH <sub>3</sub>	0.1-100	100-300	[14]
SnO <sub>2</sub>	single	NH <sub>3</sub>	0.5-200	150-300	[33]
SnO <sub>2</sub>	network	NH <sub>3</sub>	300-1000	50-300	[147]
SnO <sub>2</sub>	single	NO <sub>2</sub>	0.1-10	175	[148]
SnO <sub>2</sub>	network	NO <sub>2</sub>	0.2	250-400	[149]
SnO <sub>2</sub>	network	NO <sub>2</sub>	0.5-5	100-300	[125]
SnO <sub>2</sub>	single	H <sub>2</sub> S	1.4	250-400	[150]
SnO <sub>2</sub> -CuO	single	H <sub>2</sub> S	1-10	200-400	[151]
SnO <sub>2</sub> -CuO	network	H <sub>2</sub> S	5-80	300-400	[152]
SnO <sub>2</sub>	single	C <sub>2</sub> H <sub>5</sub> OH	10-1000	175	[28]
SnO <sub>2</sub>	network	C <sub>2</sub> H <sub>5</sub> OH	0.5-50	307	[20]
SnO <sub>2</sub>	network	C <sub>2</sub> H <sub>5</sub> OH	2.5-100	296	[153]
ZnO	single	CO	50-400	150-300	[154]
ZnO	network	CO	0.12-40	room temp.	[155]
ZnO-Pd	network	CO	0.1-2	room temp.	[12]
ZnO	network	NH <sub>3</sub>	0.5-100	180	[156]
ZnO-Pt	network	NH <sub>3</sub>	5-1000	300	[157]
ZnO	network	NO <sub>2</sub>	0.5-20	225	[131]
ZnO	network	NO <sub>2</sub>	0.2-4	23-200	[158]
ZnO	network	H <sub>2</sub> S	0.5-30	150-350	[159]
ZnO-CuO	network	H <sub>2</sub> S	0.5-30	100-350	[159]
ZnO-Au	network	H <sub>2</sub> S	1-5	room temp.	[13]
ZnO	network	C <sub>2</sub> H <sub>5</sub> OH	1-200	300	[160]
ZnO	network	C <sub>2</sub> H <sub>5</sub> OH	50-1500	180-300	[46]
CuO	single	CO	5-1200	200	[51]
CuO	network	CO	10-100	300-370	[53]

Continued on next page

<i>Material</i>	<i>Device</i>	<i>Target gas</i>	<i>Conc.</i> [ppm]	<i>Temp.</i> [°C]	<i>Ref.</i>
CuO	single	NH <sub>3</sub>	10000	room temp.	[52]
CuO	single	NH <sub>3</sub>	10-100	150-300	[50]
CuO	network	NH <sub>3</sub>	10000	room temp.	[161]
CuO-SnO <sub>2</sub>	network	NH <sub>3</sub>	10000	room temp.	[161]
CuO	single	NO <sub>2</sub>	100	room temp.	[52]
CuO	network	NO <sub>2</sub>	1-100	300-370	[53]
CuO	network	H <sub>2</sub> S	0.01-1	25-420	[55]
CuO	network	H <sub>2</sub> S	0.5-1000	25-160	[54]
CuO	single	C <sub>2</sub> H <sub>5</sub> OH	1300-3700	170-500	[31]
CuO	network	C <sub>2</sub> H <sub>5</sub> OH	25-500	400	[162]
CuO	network	C <sub>2</sub> H <sub>5</sub> OH	100-1000	200-280	[163]
In <sub>2</sub> O <sub>3</sub>	single	CO	10-100	275	[164]
In <sub>2</sub> O <sub>3</sub> -Au	single	CO	0.2-5	room temp.	[165]
In <sub>2</sub> O <sub>3</sub> -Zn	single	CO	1-5	room temp.	[166]
In <sub>2</sub> O <sub>3</sub>	single	NH <sub>3</sub>	10000	room temp.	[167]
In <sub>2</sub> O <sub>3</sub>	single	NO <sub>2</sub>	0.02-1	room temp.	[168]
In <sub>2</sub> O <sub>3</sub>	network	NO <sub>2</sub>	0.005-0.2	room temp.	[168]
In <sub>2</sub> O <sub>3</sub>	network	NO <sub>2</sub>	0.5	200-400	[169]
In <sub>2</sub> O <sub>3</sub>	single	H <sub>2</sub> S	1-160	23-160	[170]
In <sub>2</sub> O <sub>3</sub>	single	C <sub>2</sub> H <sub>5</sub> OH	1-100	100-275	[164]
WO <sub>3</sub> -Pt	network	CO	30	300	[171]
WO <sub>3</sub> -PPy	network	NH <sub>3</sub>	1-20	100	[172]
WO <sub>3</sub>	network	NO <sub>2</sub>	0.05-1	200-500	[173]
WO <sub>3</sub>	network	H <sub>2</sub> S	1-100	300	[174]
WO <sub>3</sub> -CuO	network	H <sub>2</sub> S	1-100	300	[174]
WO <sub>3</sub> -Pt	network	C <sub>2</sub> H <sub>5</sub> OH	1-200	140-300	[175]
WO <sub>3</sub> -Au	network	C <sub>2</sub> H <sub>5</sub> OH	1.5	250	[176]

Table 3.1: Overview of metal oxide nanowire based gas sensor devices

Carbon nanotubes (CNTs), on the other hand, have also been thoroughly investigated as sensor devices for similar target gases [177–180]. In this regard, they show some similarities but also several considerable differences compared to metal oxide nanowires. CNTs are graphene sheets (a monolayer of  $sp^2$ -bonded C atoms in a hexagonal lattice) rolled into cylinders with a single outer wall (single-walled CNT, SWCNT) or multiple concentrically nested walls (multi-walled CNT, MWCNT). Depending on the graphene lattice orientation with respect to the CNT axis, which is called chirality, they show metallic or semiconducting electrical properties. Typically, SWCNTs and MWCNTs have diameters from 0.8 nm to 2 nm and 5 nm to 20 nm, respectively, and lengths from 100 nm to several cm. Due to the outstanding CNT material properties, such as high carrier mobility, high electromigration threshold, high thermal conductivity or remarkable tensile strength, several potential applications (composite materials, transparent electrodes, transistors, interconnects, batteries, supercapacitors, field emitters, solar cells, biosensors ...) were demonstrated or have been commercially realized [181]. Gas sensors based on CNTs have been realized in a chemiresistor, field-effect transistor, capacitor or field emission configuration [177]. It is still under discussion if the gas sensitivity should be attributed to either chemisorption on the CNT surface or Schottky barrier modulation at the CNT-metal interface [178] or the presence of contaminants and defects [177]. The main advantage of CNT based gas sensors is their room temperature operation capability, which makes an internal heating element obsolete leading to a considerably reduced power consumption [179]. However, in some cases pristine CNTs show limitations regarding the detection of certain analytes, which makes the functionalization with catalytic metals or organic polymers inevitable [180]. Moreover, the main problem of CNT gas sensors is their lack of selectivity to different analytes [178], which they have in common with metal oxide nanowire based devices.

## 4 Synthesis of Metal Oxide Nanowires

After a short general introduction to nanowire synthesis, this chapter focuses on the synthesis of CuO and ZnO nanowires by thermal oxidation and vapor phase processes. Growth mechanism models relevant for the methods utilized within this thesis are described in Chapter 4.1.1 (CuO) and Chapter 4.2.1 (ZnO). Experimental synthesis results are shown and discussed for the case of CuO nanowires (Chapters 4.1.2, 4.1.3, 4.1.4) as well as ZnO nanowires (Chapters 4.2.2, 4.2.3).

One-dimensional nanostructures have been successfully synthesized from a variety of materials including elemental semiconductors, III-V semiconductors, II-VI semiconductors, metal oxides, carbides or nitrides. An extensive review on the synthesis of metal oxide nanowires, which are prevalent in nanowire-based gas sensing devices, can be found in [182]. Several different bottom-up techniques for nanowire growth have been thoroughly investigated during the last decades, in particular vapor phase methods, solution growth and template-assisted synthesis.

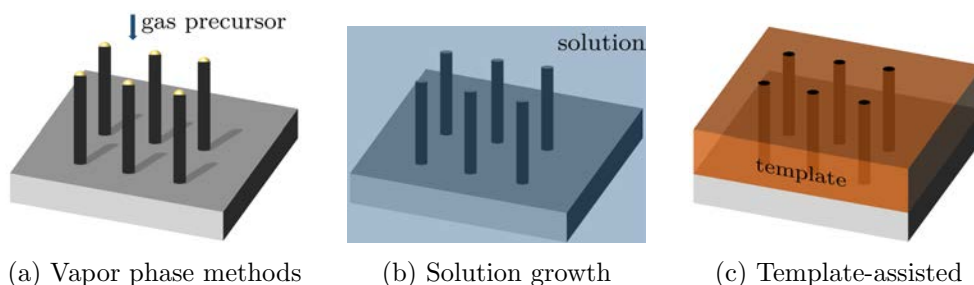


Figure 4.1: Bottom-up techniques for nanowire synthesis

Vapor phase methods are among the most extensively investigated synthesis techniques and rely on technologies such as laser ablation, chemical vapor deposition, chemical vapor transport, molecular beam epitaxy or sputtering for the preparation of gas phase species. The one-dimensional growth is most commonly explained by the vapor-liquid-solid (VLS) or the vapor-solid (VS) mechanism. During VLS synthesis a liquid droplet is formed from either a catalyst metal or from one element of a compound semiconductor



(self-catalytic VLS). The gas phase species dissolve into the droplet leading to supersaturation, nucleation and one-dimensional nanowire growth (Fig.4.1a). The droplet size determines the nanowire diameter, whereas its length can be controlled by the growth time. Longitudinal and coaxial nanowire heterostructures can be fabricated by switching between different gas phase precursors during the synthesis process. In contrast, the VS mechanism explains one-dimensional nanowire formation by an anisotropic growth mechanism (thermodynamic and kinetic parameters depending on the crystal facet) or by defect-induced models [183]. Regarding the realization of functional nanowire devices by vapor phase methods site-specific growth with controlled morphology is of crucial importance, which was reviewed in [184].

Alternatively, solution-based methods can be utilized for nanowire growth (Fig.4.1b). In this case, the main advantages are low cost and the low temperature synthesis process allowing the large scale fabrication of nanowire arrays on a variety of substrates. However, this method also shows considerable disadvantages such as potential contamination, little control over areal density, small aspect ratios and poor vertical alignment [144,184].

For large-scale nanowire synthesis template-assisted methods (Fig.4.1c) are particularly interesting. One-dimensional growth can be achieved using templates such as anodic aluminum oxide or polymer membranes. Nanowires are fabricated by filling the template nanopores by electrochemical deposition, electrophoretic deposition or template filling and subsequent dissolution of the template material. The dimensions of the one-dimensional nanostructures can be easily controlled, but nanowires typically show poor crystalline quality and difficulties during template removal may occur [185].

## 4.1 CuO Nanowires

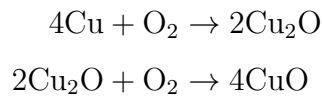
Cupric oxide (CuO) crystallizes in the C2/C monoclinic tenorite structure in contrast to other 3d transition-metal oxides with a cubic crystal lattice [186]. It shows p-type semiconducting properties with indirect band gap values reported from 1.2-1.9 eV. The theoretical description of the CuO band structure is complicated by strong electron-electron interactions in this material. Electrical conductivity is attributed to non-stoichiometry due to vacancies or antisite defects [187].

In literature, CuO nanowire synthesis has been reported by various different techniques, for instance thermal oxidation, solution-based methods, template-assisted electrochemical deposition, electrospinning, hydrothermal methods and direct plasma oxidation. A recent review on Cu<sub>2</sub>O and CuO nanowire growth can be found in [188], which also includes a thorough discussion of the advantages and disadvantages of the different synthesis techniques. In this thesis, CuO nanowires were synthesized by thermal oxidation of various Cu substrates, which is most commonly linked with high nanowire crystalline quality, simplicity and low cost [188]. Furthermore, this method is particularly interesting for CMOS integration due to the comparatively low nanowire synthesis temperatures and the possibility of site-specific nanowire growth by thermal oxidation of microstructured Cu thin films [189].

### 4.1.1 Thermal Oxidation Growth Mechanism

After reports on low-aspect-ratio CuO whiskers in the 1950's it was shown in [190] that CuO nanowires can be synthesized by thermal oxidation of various Cu substrates (TEM grids, wires, foils) at temperatures from 400 °C to 700 °C. CuO nanowires with diameters between 30 nm and 100 nm were achieved and the growth mechanism was attributed to the VS mechanism in this initial study. Up to now numerous investigations on CuO nanowire synthesis have been performed resulting in comparable experimental results.

However, it was argued that CuO nanowire growth cannot be attributed to the VS mechanism as the partial pressure of precursor species is expected to be far too low for the observed growth rates [191]. In recent studies, CuO nanowire synthesis was explained by a model relying on grain boundary diffusion [192] influenced by stress gradients that are induced by thermal oxidation [193, 194]. It is generally accepted that the thermal oxidation of Cu during CuO nanowire growth comprises two steps [190, 191]:



This mechanism is supported by experimental findings that Cu samples, which were thermally oxidized in the temperature range of CuO nanowire growth, are covered by two different copper oxide layers, i.e. a columnar  $\text{Cu}_2\text{O}$  layer above the Cu substrate and a nanocrystalline CuO layer on top, which is covered by CuO Nanowires [191, 193].

The mechanism for CuO nanowire growth proposed in [192–194] relies on grain boundary diffusion of Cu cations towards the oxidizing surface. In general, the diffusion along line and surface defects such as grain boundaries, surfaces or dislocations is more rapid than lattice diffusion and is thus often termed 'short-circuit diffusion'. The activation energy for diffusion along defects is smaller than for lattice diffusion and thus short-circuit diffusion dominates at lower temperatures. Typically, the transition from lattice diffusion to short-circuit diffusion is related to the melting point  $T_m$  of the material and occurs at temperatures between  $0.5 \cdot T_m$  and  $0.7 \cdot T_m$  [195].

A schematic illustration of the CuO nanowire growth mechanism is shown in Fig.4.2, where the multi-layered structure of a thermally oxidized Cu sample is shown. The diffusion of Cu cations from bottom to top serves as source for further oxidation of the sample and thus growth of the copper oxide layers. Due to the comparatively low thermal oxidation temperatures typically between  $400^\circ\text{C}$  and  $700^\circ\text{C}$  it is expected that the dominant mechanism is short-circuit diffusion at grain boundaries. After having passed the

large, columnar  $\text{Cu}_2\text{O}$  layer and the nanocrystalline  $\text{CuO}$  layer,  $\text{Cu}$  cations diffuse at the  $\text{CuO}$  surface and along the nanowire sidewalls towards the tip [193,194]. Facets of  $\text{CuO}$  grains were proposed to serve as template for nanowire growth and twin structures may occur due to  $\text{CuO}$  grains with multiple facets [193].  $\text{CuO}$  nanowire growth was suggested to proceed at the tips due to imaging results for different thermal oxidation times at the same sample location [194].

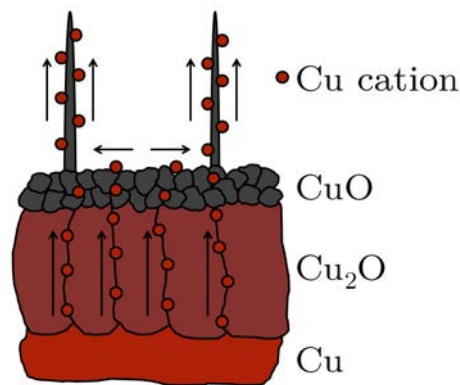


Figure 4.2: Schematics of the grain boundary diffusion model for  $\text{CuO}$  nanowire growth (adapted from [194])

During  $\text{CuO}$  nanowire growth the oxidizing atmosphere and the copper oxide layers establish a chemical potential gradient, which can be identified as one driving force for the  $\text{Cu}$  cation diffusion towards the surface [193]. However, the differences in unit cell volumes of  $\text{Cu}$ ,  $\text{Cu}_2\text{O}$  and  $\text{CuO}$  leads to stress gradients within the sample. The  $\text{Cu}_2\text{O}$  layer experiences compressive stress at the bottom  $\text{Cu}$  interface and tensile stress at the  $\text{CuO}$  interface. On the other hand, the  $\text{CuO}$  layer suffers compression at the  $\text{Cu}_2\text{O}$  interface, whereas the top surface is stress-free. Stress gradients are accompanied by mass transfer due to stress-induced migration and can be thus identified as additional driving force for  $\text{Cu}$  cation grain boundary diffusion [193,194].

There are several experimental indications that support the described  $\text{CuO}$  nanowire growth mechanism. The authors of [196] found that an electric field perpendicular to the growth substrate leads to decreased nanowire diameters and up to a five-fold increase in lengths. The results can be understood by

the interaction of the electric field and the diffusing Cu cations, which affects the effective diffusion rates. During the thermal oxidation of patterned Cu films CuO nanowires grew preferentially on the structure edges, which was in accordance with the described growth mechanism when considering the stress distribution obtained by finite element simulations [194]. Furthermore, the influence of surface stresses was described in [197] by investigating thermal oxidation of bent Cu foils. Enhanced CuO nanowire growth was observed for tensile stress and was interpreted by an increased effective diffusion rate due to a larger number of grain boundaries. Most importantly, direct evidence for the Cu cation outdiffusion via grain boundaries was found recently by Raman mapping of CuO nanowire sample cross sections [198].

CuO nanowires synthesized by the thermal oxidation method were found to grow in multiple preferred directions [52]. Some authors reported on single-crystalline CuO nanowires [51, 54, 191, 199], whereas others observed bi-crystalline CuO nanowires with a twin boundary [189, 190, 193, 200, 201]. The average nanowire length increases with synthesis time and follows a parabolic law [192], which is consistent with the diffusion-limited growth mechanism described above. Moreover, it was found that the temperature dependence of the parabolic rate constant can be described by an Arrhenius equation [199]. In most cases increasing nanowire diameter and decreasing nanowire areal density were observed experimentally for increasing oxidation temperatures [162, 191, 192, 194]. Photoluminescence measurements [202] and energy-dispersive X-ray spectroscopy combined with Raman spectroscopy [200] were performed on different CuO nanowire positions, which indicated that mixed copper oxide phases may be present at the root of the nanowires.

Apart from oxidation temperature and time, the Cu substrate has been identified as major influencing factor for CuO nanowire growth. It was suggested in [203] that a minimum critical thickness is required, which was found to lie around 300 nm in this specific case. Furthermore, CuO nanowire growth on electroplated and thermally evaporated Cu thin films was compared [189].

Superior synthesis results regarding nanowire lengths and areal density were achieved on electroplated Cu thin films, which was interpreted by its surface roughness and microstructure. The importance of Cu substrate morphology was also shown in [201], where surface mechanical treatment of Cu plates resulted in different CuO nanowire synthesis results.

The oxidizing atmosphere also has a considerable influence on CuO nanowire growth during thermal oxidation. It was observed that nanowire areal density is affected by the presence of water vapor and oxygen concentration [204]. The authors suggested that the presence of water vapor enhances the nucleation rate, whereas oxygen concentration is related with both nucleation rate and nanowire growth rate. Moreover, the vertical alignment of CuO nanowires could be increased by using a  $N_2/O_2$  gas flow compared to static air [189]. The influence of the local gas-flow field on the alignment and areal density of CuO nanowires was also investigated in [205] and compared with computational fluid dynamics simulations.

#### **4.1.2 Thermal Oxidation of Cu Wires by Resistive Heating**

In this chapter, CuO nanowire synthesis experiments by thermal oxidation of a Cu wire by direct resistive heating will be described. In particular, a highly pure Cu wire (6N, Alfa Aesar) with a diameter of 100  $\mu\text{m}$  was wrapped around a Pt-100 temperature sensor (10x2 Pt100, Delta-R) (see Fig.4.3a). Resistive Joule heating of the Cu wire was used to heat it to the desired CuO nanowire synthesis temperature, which was measured by the Pt-100 temperature sensor using a Agilent Technologies 34401A multimeter. As the resistance of the Cu wire changes during the thermal oxidation process, constant current operation is not feasible for experiments at constant temperatures. Therefore, the temperature is kept constant by adjusting the current through the Cu wire (current source Thurbly Thandar Instruments PL330P) by a PID control implemented in LabView.

As can be seen in Fig.4.3b, the color of the Cu wire turns black during the thermal oxidation process in ambient atmosphere, which is a first indication for the formation of CuO. The nanowire synthesis experiments were typically performed from 300-500 °C for thermal oxidation times up to 200 min. The oxidized Cu wires were characterized using a Zeiss Supra 40 scanning electron microscope (SEM). Results for CuO nanowire synthesis at  $T \sim 500$  °C for 200 min are shown in Fig.4.3c. In this case, typical nanowire diameters range from 50 nm to 200 nm and lengths lie between several  $\mu\text{m}$  and 100  $\mu\text{m}$ . Thus remarkable aspect ratios up to 1000 could be achieved at high nanowire areal densities. The CuO nanowire cross-sections most commonly exhibited faceted edges (see inset of Fig.4.3c), which is an indication for high crystalline quality. In additional experiments increasing nanowire diameters and lengths were found for increasing thermal oxidation temperatures. Moreover, longer thermal oxidation time resulted in nanowires with increased average length.

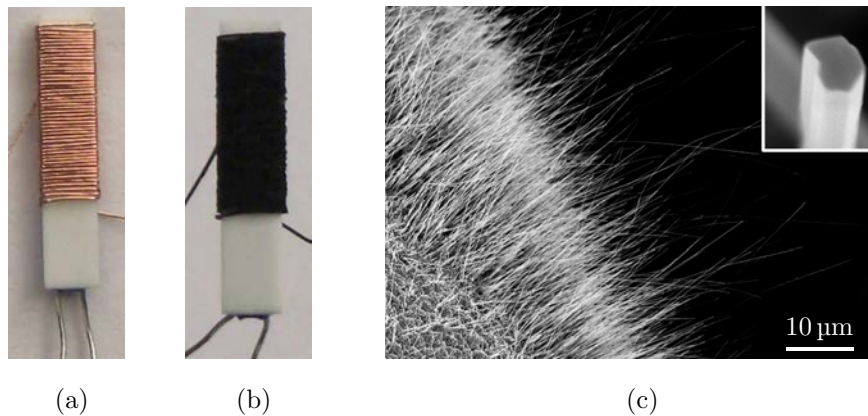


Figure 4.3: CuO nanowire synthesis by thermal oxidation of a Cu wire. (a) Cu wire wrapped around a Pt-100 temperature sensor. (b) After thermal oxidation by resistive heating in ambient atmosphere. (c) CuO nanowire growth at  $T \sim 500$  °C for 200 min; the inset shows a typical faceted CuO nanowire cross-section (width  $\sim 100$  nm).

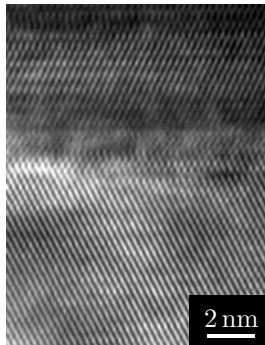
Comparable CuO nanowire synthesis experiments relying on resistive heating of Cu wires were performed in [206], but nanowire lengths did not exceed 2  $\mu\text{m}$  in this case. Regarding nanowire dimensions and areal density the presented results are in good agreement with literature reports on CuO nanowire growth on Cu wires [190] and Cu foils [191, 192] utilizing conventional heating in a furnace or on a hotplate. Similar temperature and time dependencies of CuO

nanowire dimensions were observed in literature [191, 192] and the faceted cross-sections are well comparable to those reported in [52].

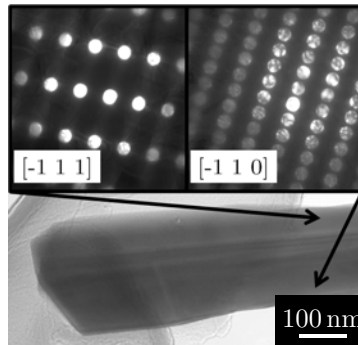
After mechanical transfer to transmission electron microscopy (TEM) grids (Quantifoil R 2/2), the CuO nanowires were further characterized using a FEI Tecnai F20 at an electron beam energy of 200 keV by the Institute for Electron Microscopy, Graz University of Technology. The CuO nanowires synthesized by thermal oxidation of a Cu wire showed single crystalline or bi-crystalline structure. In Fig.4.4a, a high resolution TEM image of a bi-crystalline CuO nanowire with twinning characteristics is shown. The transition area between the two crystalline orientations can be clearly observed. On another CuO nanowire, convergent beam electron diffraction was used on two different positions as indicated by the red arrows in Fig.4.4b, also confirming the different crystal orientations. Thus the crystallinity of the CuO nanowires synthesized by thermal oxidation of Cu wires is comparable to the various literature reports cited in the previous chapter. Regarding the device application it is expected that the high crystalline quality leads to favorable gas sensing properties.

Moreover, electron energy loss spectroscopy was used as a complementary method in order to characterize the nanowire material properties. In particular, the near edge line structure of the Cu  $L_{23}$ -edge and the O K-edge (see Fig.4.4c) were compared to literature results [207–209]. The acquired spectra clearly differ from elemental Cu and cuprous oxide  $Cu_2O$  and are in excellent agreement with cupric oxide CuO. These findings further confirm the material composition of the synthesized CuO nanowires.

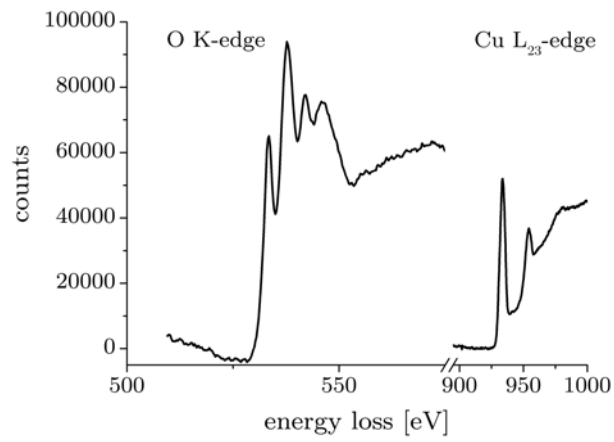




(a) High resolution TEM of bi-crystalline CuO nanowire



(b) Convergent beam electron diffraction on two CuO nanowire positions



(c) Electron energy loss spectroscopy of single CuO nanowire

Figure 4.4: Characterization of CuO nanowires synthesized by thermal oxidation of Cu wires by resistive heating

### 4.1.3 Thermal Oxidation of Electroplated Cu Structures

The fabrication of electroplated Cu structures was performed by Siemens Corporate Technology and comprised the following steps (see Fig.4.5a):

At first, thermal oxidation of a 4" Si wafer was performed in order to achieve a SiO<sub>2</sub> layer with a thickness of 500 nm. Next, a Ti/Cu seed layer (50 nm and 150 nm, respectively) was sputter-deposited and photolithography was performed (resist thickness 7 μm) in order to define the areas for the subsequent Cu deposition process. Cu structures with a thickness of 2.5 μm were achieved by site-selective electrodeposition. Next, the photoresist was removed and the residual Ti/Cu seed layer was wet-etched using sodium persulfate and a diluted 5% hydrofluoric acid solution. A microscope image for typical electroplated Cu structures (width 25 μm, length 215 μm, gap distance 5 μm) is shown in Fig.4.5b.

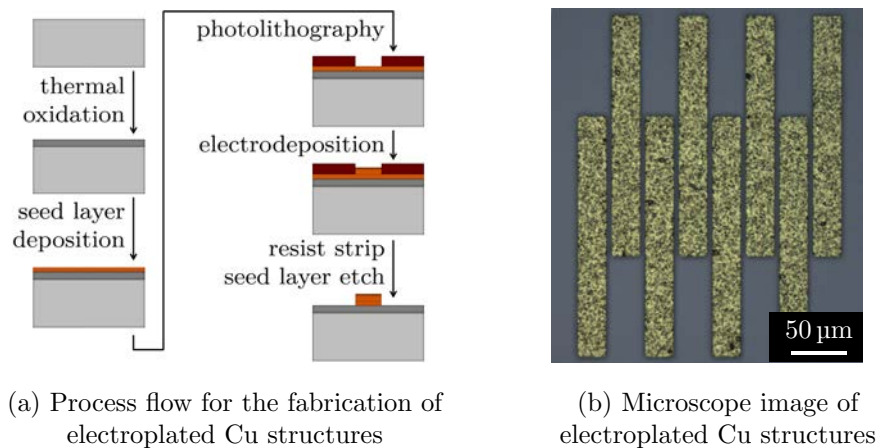


Figure 4.5: Fabrication of electroplated Cu structures (thickness 2.5 μm)

After dicing of the 4" wafer, an Ar ion etching process (Roth & Rau IonSys 500, 2 min) was performed for cleaning of the electroplated Cu structure surfaces. Subsequently, the samples were oxidized in a furnace under a constant flow of pure oxygen at 400 °C for three hours. During the thermal oxidation process the initial gap distance (5 μm) was first of all considerably reduced to around 2.5 μm due to the growth of two copper oxide layers (Cu<sub>2</sub>O and CuO). Moreover, CuO nanowires were synthesized homogeneously on the

oxidized Cu structures and the gap in between was bridged by suspended CuO nanowires (see Fig.4.6). Typically, CuO nanowires grown with this specific technology showed dimensions with lengths in the range of few  $\mu\text{m}$  and diameters between 15 nm and 70 nm.

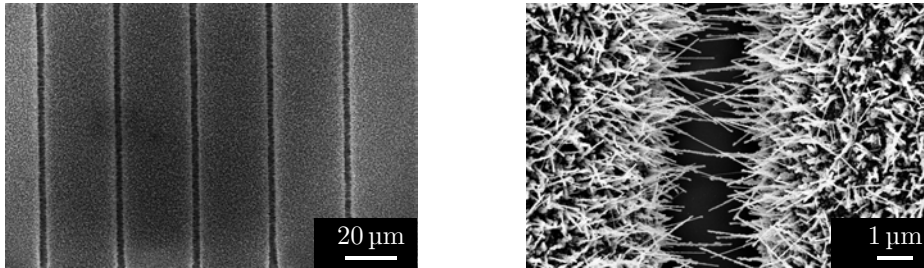


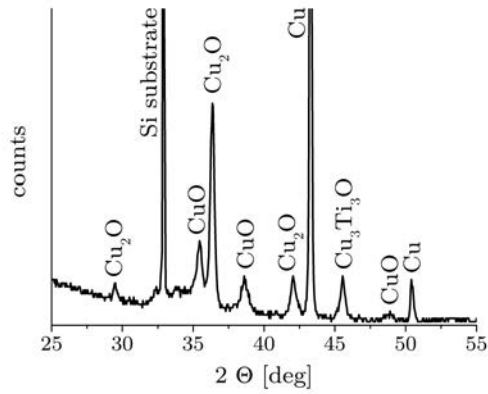
Figure 4.6: CuO nanowire synthesis by thermal oxidation (400 °C, O<sub>2</sub> atmosphere) of electroplated Cu structures

For characterization of the thermally oxidized Cu structures, X-ray diffraction (XRD) measurements were performed by the Institute of Solid State Physics, Graz University of Technology. Different samples containing electrodeposited Cu structures without and with the thermal oxidation process for CuO nanowire synthesis were analyzed by specular scans using a Siemens D501 diffractometer in Bragg-Brentano geometry. Diffraction peaks were compared with the database PDF2 from the International Center for Diffraction Data (ICDD). On samples with Cu structures before thermal oxidation XRD peaks for Ti and Cu (apart from the Si substrate) could be found, which is expected due to the Ti/Cu seed layer and the electrodeposited Cu layer. XRD results on samples with CuO nanowires synthesized on oxidized Cu structures are shown in Fig.4.7a. As can be seen, elemental Cu and the two different copper oxide phases Cu<sub>2</sub>O and CuO were present, which indicates similar oxidation behavior of the electrodeposited Cu structures compared to literature results. Furthermore, another diffraction peak is observed around 45.5°. It can be most likely attributed to Cu<sub>3</sub>Ti<sub>3</sub>O that is formed during the thermal oxidation process at the interface of the Ti adhesion layer and the Cu layer, which is supported by additional pole figure measurements that are not shown here.

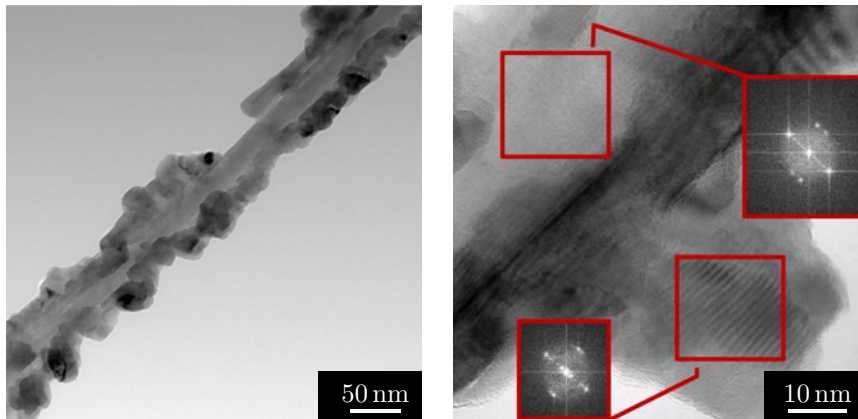
For TEM characterization, CuO nanowires were synthesized on electroplated Cu squares with an edge length of 5 mm in order to increase the total number of CuO nanowires and thus facilitate TEM sample preparation. The same parameters were used for the Cu deposition and the thermal oxidation process, which lead to comparable CuO nanowire synthesis results. The CuO nanowires were transferred to TEM grids (Quantifoil R 2/2) and were characterized using a FEI Tecnai F20 at an electron beam energy of 200 keV at the Institute for Electron Microscopy, Graz University of Technology. A typical TEM image can be seen in Fig.4.7b. The CuO nanowires showed polycrystalline structure with crystallites at the nanowire surface as was already presumed after SEM imaging. In literature, however, the synthesis of single crystalline or bi-crystalline CuO nanowires was reported during thermal oxidation of copper substrates (see Chapter 4.1.1). Moreover, the CuO nanowires synthesized by resistive heating of a Cu wire (Chapter 4.1.2) also showed single or bi-crystalline structure. As the morphology of the CuO nanowires synthesized by thermal oxidation of electroplated Cu structures clearly differs from other CuO nanowire synthesis results, potential reasons for this specific growth behavior need to be discussed.

In addition, the CuO nanowires were further characterized by EELS during the TEM measurements in order to gain additional information on their material composition. Identical results were achieved for several different CuO nanowires, which all exhibited near edge structures of both the O K-edge and the Cu L<sub>23</sub>-edge that are in good agreement with literature results for bulk CuO [207–209] and also with the spectra of CuO nanowires synthesized by thermal oxidation of Cu wires (see Fig.4.4c). On a single CuO nanowire, twenty EELS spectra were recorded across its diameter, which is indicated by the green line in Fig.4.7c). The different spectra showed nearly identical results confirming that the core of the CuO nanowire and the crystallites on the edges both consist of CuO.

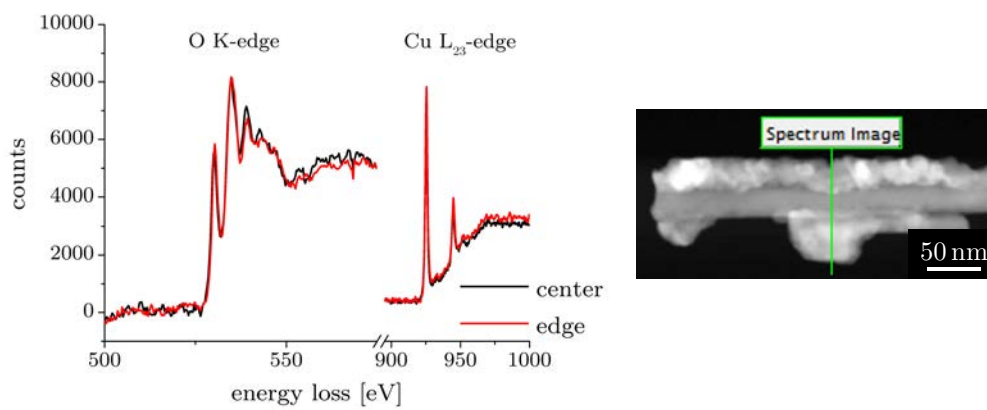
As mentioned earlier it was suggested in [193] that CuO grain facets serve as structure templates during initial CuO nanowire growth resulting in a



(a) X-ray diffraction



(b) TEM imaging of single CuO nanowire



(c) Electron energy loss spectroscopy across the diameter of a single CuO nanowire

Figure 4.7: Characterization of CuO nanowires synthesized by thermal oxidation of electroplated Cu structures

twin or multi-twin structure. Moreover, stress-induced grain boundary diffusion of Cu cations was claimed to be the driving force for the formation of CuO nanowires. According to this literature model, Cu cations diffuse along the CuO nanowire surface towards the tip and are incorporated into the nanowire after reaction with oxygen. In [189], CuO nanowire growth on thermally evaporated and electroplated Cu thin films was compared. In that study, electroplated Cu thin films were found to be better suited for CuO nanowire synthesis as longer nanowires at higher areal densities were achieved. The authors attributed the enhanced CuO nanowire growth to the morphology of the electroplated Cu thin film. Furthermore, it was found that a constant gas flow leads to a higher thermal oxidation rate compared to static air. In [194] preferred CuO nanowire growth on the structure edges of patterned evaporated Cu films was reported, where the authors emphasized the importance of stress gradients in the oxidized Cu structures.

After thermal oxidation of the electroplated Cu structures, homogeneous CuO nanowire growth was observed on the entire surface, which can be seen in Fig.4.6. The TEM results (Fig.4.7b) suggest that the CuO nanowires consist of a crystalline core and crystallites on the edges. As described in Chapter 4.1.1, it was claimed that the migration of Cu ions serves as continuous source for the formation of CuO nanowires [194]. Considering the literature results described in the previous paragraph, it is expected that the use of electroplated Cu films combined with the other experimental parameters as structure size and thermal oxidation conditions (constant flow of pure oxygen) resulted in a very high diffusion rate of Cu ions. It is assumed that these Cu ions were not fully incorporated during CuO nanowire growth but rather nucleated on the surface forming CuO crystallites. Thereby the polycrystalline structure of the CuO nanowires on the oxidized electroplated Cu structures could be potentially explained. However, additional synthesis experiments with varying Cu structure geometries and different thermal oxidation parameters are suggested in order to gain a more profound understanding on CuO nanowire growth on electroplated Cu structures.

#### 4.1.4 Thermal Oxidation of Evaporated Cu Structures

For the fabrication of Cu microstructures with different geometries, a photolithographic lift-off process (image reversal resist AZ5214E; process parameters in Appendix A) was performed on a Si substrate with 300 nm of thermal SiO<sub>2</sub>. A Ti/Cu thin film (5 nm and 500 nm thickness, respectively) was deposited by thermal evaporation. The intermediate Ti layer was used in order to improve thin film adhesion and reduce Cu diffusion in the subsequent thermal oxidation step. For the synthesis of CuO nanowires, the samples were thermally oxidized at 350 °C for three hours on a hotplate in ambient atmosphere.

In Fig.4.8 it can be seen that CuO nanowires were synthesized on various Cu structures such as lines, holes or squares with dimensions down to few  $\mu\text{m}$ . CuO nanowires were mainly found on the structure edges, where their lengths and areal density were significantly enhanced. In contrast to the synthesis results on electroplated Cu structures presented in the previous chapter, no signs of any crystallites were observed on the smooth and featureless surfaces of the CuO nanowires (Fig.4.8d). Thus single crystalline or bi-crystalline structure is assumed as is common for CuO nanowires grown by the thermal oxidation method. Typically, the CuO nanowires showed lengths between 500 nm and 2  $\mu\text{m}$  with very small diameters between 10 nm and 30 nm.

In [189] almost no CuO nanowires were found on thermally evaporated Cu thin films (thickness 500 nm) that were thermally oxidized at 500 °C for four hours in static air. The authors of [194] reported on CuO nanowire growth by thermal oxidation of electron beam evaporated Cu thin films with a thickness of 400 nm. At a nanowire synthesis temperature of 350 °C they achieved CuO nanowires with an average length of 1.6  $\mu\text{m}$  and an average diameter of 30 nm, which is very similar to the results presented here. According to [193], the facets of CuO grains serve as templates for initial CuO nanowire growth most commonly resulting in a twin or multi-twin structure. Therefore, the formation of CuO nanowires with very small diameters between 10 nm and

30 nm is attributed to the morphology of the evaporated Cu thin film. As was mentioned earlier, enhanced CuO nanowire growth on the edges of Cu microstructures was observed in literature as well as in this study. In [194] this was explained by reduced compressive stress at the structure edges, which was also supported by finite element thermo-mechanical simulations. This is consistent with other CuO nanowire synthesis results on bended Cu foils, where tensile stress was reported to promote CuO nanowire formation [197].

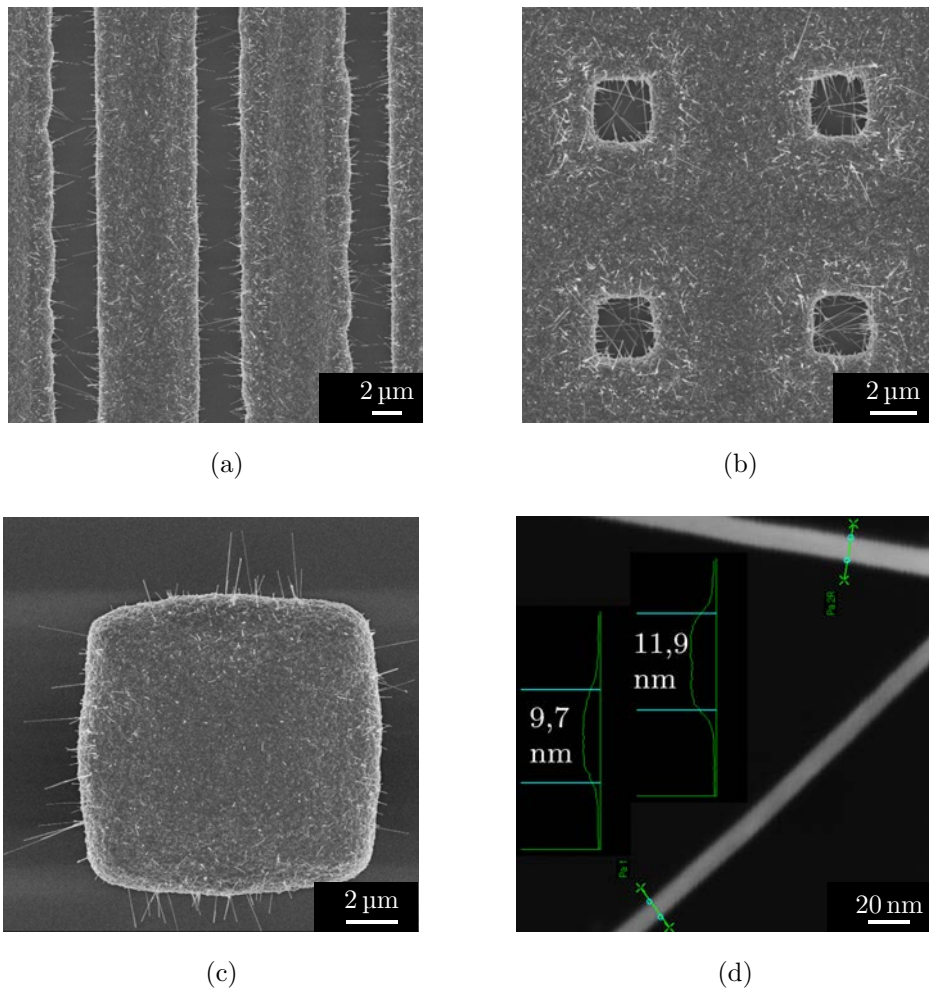


Figure 4.8: CuO nanowire synthesis by thermal oxidation (350 °C, ambient atmosphere) of evaporated Cu structures such as a) lines, b) holes and c) squares. Diameters down to 10 nm were observed as can be seen in d).



For XRD characterization large arrays of identical Cu structures (width 5  $\mu\text{m}$ , length 60  $\mu\text{m}$ ) were fabricated. The same substrates, process steps, material deposition methods and thermal oxidation parameters were used as described above leading to comparable CuO nanowire synthesis results. Measurements were performed by specular scans using a Siemens D501 diffractometer in Bragg-Brentano geometry by the Institute of Solid State Physics, Graz University of Technology. The database PDF2 from the International Center for Diffraction Data (ICDD) was used for peak identification.

The thermally evaporated Cu thin film structures showed preferential orientation of the [111] planes parallel to the substrate surface. After thermal oxidation the phases Cu, Cu<sub>2</sub>O and CuO were found on the sample with a random orientation of CuO grains and nanowires (see Fig.4.9). Thus CuO nanowire synthesis as well as XRD results achieved by thermal oxidation of thermally evaporated Cu structures are very well comparable to literature results and the growth characteristics can be explained by existing models.

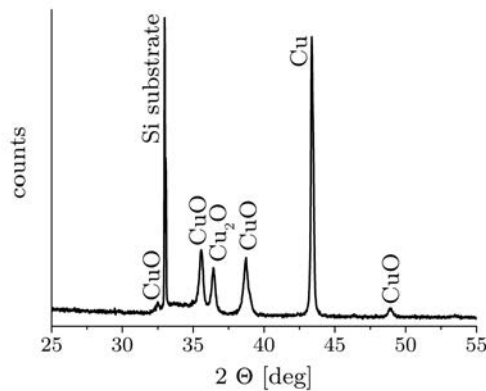


Figure 4.9: X-ray diffraction of CuO nanowire sample fabricated by thermal oxidation of evaporated Cu structures

## 4.2 ZnO Nanowires

Zinc oxide (ZnO) most commonly crystallizes in the  $C6mc$  hexagonal wurtzite structure. In certain crystallographic orientations ZnO is spontaneously polarized as surfaces perpendicular to the  $[001]$   $c$ -axis are entirely terminated by either positively charged Zn atoms or negatively charged O atoms (typically termed polar surfaces). Three types of preferred growth directions for single crystal growth were identified [210], i.e.  $\langle 2\bar{1}0 \rangle$ ,  $\langle 010 \rangle$  and  $[001]$ . ZnO has a wide direct band gap of 3.44 eV and was found to be particularly interesting for electronic and optoelectronic applications [211]. ZnO shows unintentional n-type doping, which was attributed to native point defects such as vacancies, interstitials or antisite defects. However, density functional theory calculations favored incorporation of impurities (e.g. H) as potential reason for shallow donor levels. Although p-type doping has been achieved using N, P, As or Sb, the results lack of reproducibility and theoretical understanding [212].

In most cases, ZnO nanowire synthesis has been reported by vapor phase methods (VLS as well as VS mechanism), metal-organic chemical vapor deposition, thermal oxidation, template-assisted methods or hydrothermal growth [210,213,214]. In addition, ZnO was found to grow in complex geometries such as hierarchical nanostructures, nanobelts, nanocombs, nanosprings or nanorings [215]. Here, focus is put on the mechanisms during VS, self-catalytic VLS and thermal oxidation nanowire synthesis due to their relevance for the experimental results for ZnO nanowire growth that will be presented later on.

### 4.2.1 Growth Mechanisms

The growth of ZnO nanowires in the absence of a catalyst metal particle has been observed under several different experimental conditions. Most commonly, Zn precursors are thermally evaporated in a tube furnace and are transported to the growth substrate using defined gas flow conditions.

Depending on local temperature, pressure, carrier gas, substrate and evaporation time, ZnO nanostructures with different geometries can be obtained [215]. Several groups have reported on ZnO nanowire synthesis by this technique [48,49,216] and the growth mechanism was attributed to the VS mechanism. Due to anisotropic surface energies, the surfaces of the  $\langle 2\bar{1}0 \rangle$  and  $\langle 010 \rangle$  crystal facets tend to be minimized leading to preferred growth in  $[001]$  direction [210]. One-dimensional growth may also be favored due to a large number of steps on the nanowire tips acting as preferred adsorption sites or due to specific gas flow conditions [213]. However, the importance of liquid Zn or suboxide  $\text{ZnO}_x$  ( $x < 1$ ) droplets for ZnO nanowire synthesis was highlighted in [217, 218] and the growth mechanism was attributed to a self-catalytic VLS process. Due to the low melting point of Zn and  $\text{ZnO}_x$  ( $419^\circ\text{C}$ ) it was proposed that liquid droplets are formed after condensation on the substrate. These droplets act as favored sites for absorption of vapor phase Zn,  $\text{O}_2$  or ZnO resulting in supersaturation and one-dimensional growth. In [219] ZnO nanowire synthesis was systematically studied at defined sample positions for different oxygen flow rates. The results were interpreted by a self-catalytic VLS mechanism, which was supported by comparison with classical nucleation theory. Moreover it was suggested that low Zn vapor supersaturation may lead to depletion of the Zn/ $\text{ZnO}_x$  droplet and continuation of growth via the VS mechanism.

As an alternative to the vapor phase transport method, ZnO nanowires can be synthesized by thermal oxidation of Zn substrates at temperatures above the Zn melting point at high oxygen partial pressures similar to atmospheric conditions. In [220] thermal oxidation of Zn powders and thin films was studied. ZnO nanowires were synthesized on the oxidized surfaces and the growth mechanism was explained by ZnO nucleation and one-dimensional growth on liquid Zn droplets, which act as source material. Similar experiments were performed in [221], where ZnO nanowires were grown by thermal oxidation of evaporated Zn nanoplates. In this case liquid Zn was also assumed to act as nucleation site, but Zn vapor was claimed to be the source during ZnO nanowire growth. The authors of [222] studied the thermal oxidation of sin-

gle Zn grains, which showed hexagonal faceting and polar top and bottom surfaces. Preferential ZnO nanowire growth from the grain edges, in particular the hexagon corners, was observed, whereas no nanowires were found on the top and bottom [001] surfaces. Based on these experiments, where a very well-defined substrate was employed for ZnO nanowire synthesis, a growth model was proposed relying on edge-enhanced oxidation of liquid Zn leading to the formation of ZnO nanoclusters and subsequent one-dimensional growth. In [223], thermal oxidation of Zn polyhedrals with flat [001] top faces and stepped side faces was studied. Again, no nanowires were observed on the polar surfaces, but dendritic ZnO nanostructure growth was found from the stepped side faces, which was explained by a self-catalytic VLS process.

However, other authors attributed ZnO nanowire growth during thermal oxidation of Zn substrates to solid state diffusion processes similar as for CuO nanowires described above (Chapter 4.1.1). The authors of [224] investigated thermal oxidation of Zn wires at temperatures around and above the melting point. A parabolic time dependence of ZnO nanowire growth rate with an Arrhenius-type temperature dependence was found. The results were interpreted by short-circuit diffusion of Zn interstitials and vacancies from the Zn substrate through a ZnO layer towards the surface. In [225] ZnO nanowire synthesis by thermal oxidation of evaporated thin films and single Zn grains was studied. Also in this case a parabolic time dependence of ZnO nanowire length was found and growth was attributed to a similar grain boundary diffusion-based model. In addition, bicrystalline structure of the ZnO nanowires with twin boundaries along the axis was observed. Twin formation was expected to be induced by stress and the twin boundary was assumed to be a short-circuit diffusion path for stress-driven transport of Zn cations towards the ZnO nanowire tip, where growth of the one-dimensional structures continues.

Similar ZnO nanowire synthesis results at temperatures below the Zn melting point were also attributed to short-circuit diffusion across ZnO grain boundaries [214, 226]. The influence of Zn substrate morphology during low

temperature thermal oxidation was investigated in [227] and ZnO nanowire synthesis was found to be dependent on surface roughness. In [228] evaporated Zn films were thermally oxidized in various dry and humid atmospheric conditions resulting in ZnO nanowires and thin films with different defect concentrations and electric resistivities.

#### 4.2.2 Vapor Phase Growth Using Zn Wires

In the following, ZnO nanowire synthesis experiments using vapor phase methods are described. A highly pure Zn wire (purity 99.994%, Alfa Aesar) with a diameter of 250  $\mu\text{m}$  was wrapped around a commercially available microheater (10x2 Pt6,8; Delta-R), which can be seen in Fig.4.10a. The sample was mounted inside a glass tube, which was connected on one side with a constant flow of Ar (1000sccm, 5.0, Linde Gas) and on the other side with ambient atmosphere through a stainless steel tube (inner diameter  $\sim 4$  mm). Electrical connections to the outside were established by wires soldered to the two microheater contacts. After 10 min of Ar purging, the microheater was biased at a constant current of 255 mA for one hour. The temperature during ZnO nanowire synthesis was estimated to lie between 450-500  $^{\circ}\text{C}$  by continuously measuring the resistance of the microheater, which has a known temperature dependence. Optical inspection revealed that a white layer had formed on the sample surface after the synthesis process. It was found that ZnO nanowires were successfully synthesized on the Zn wire (Fig.4.10b) as well as on the microheater substrate (Fig.4.10c). The nanowire diameters typically ranged from 30-150 nm and lengths up to several tens of  $\mu\text{m}$  were achieved.

The synthesis of ZnO nanowires can be attributed to the vapor phase VS or VLS mechanism as nanowires were also found on the microheater substrate at a distance of few mm to the Zn wire. Furthermore, the ZnO nanowire lengths of several tens of  $\mu\text{m}$  are an indication of vapor phase synthesis, whereas ZnO nanowires grown by solid state diffusion processes typically reach lengths of few  $\mu\text{m}$  [224]. In a control experiment, a constant flow of 1000 sccm of  $\text{O}_2$

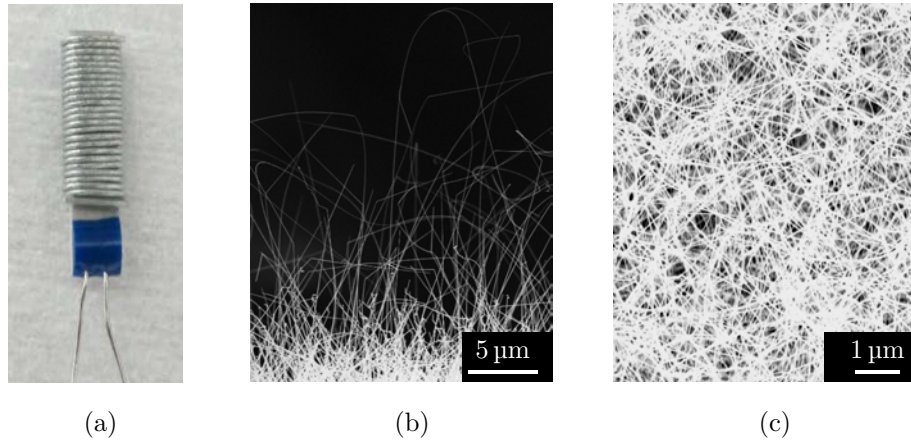


Figure 4.10: ZnO nanowire synthesis by heating of a Zn wire. a) Zn wire wrapped around a microheater. ZnO nanowires grown on the b) Zn wire and on the c) microheater substrate ( $I_{heat}=255$  mA, 1000 sccm Ar flow).

was used resulting in very short nanowires. It is assumed that in this case short-circuit grain boundary diffusion is the underlying mechanism due to the formation of a protective ZnO layer on the oxidized Zn wire surfaces.

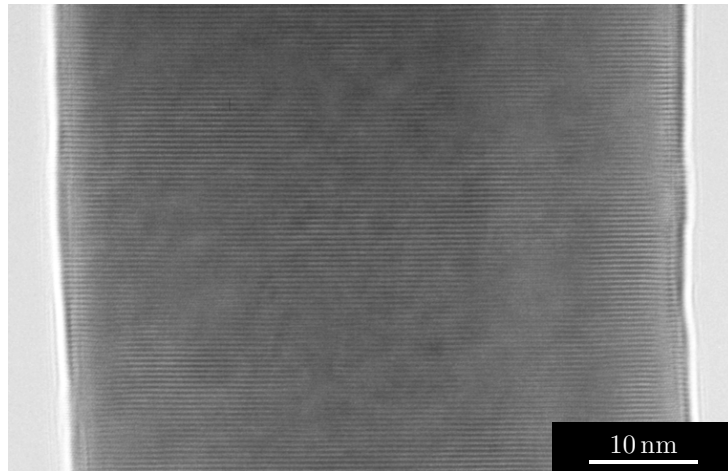
As proposed in [219], both VS and VLS mechanism may be responsible for ZnO nanowire growth depending on the ratio of Zn and  $O_2$  in the vapor phase precursors. Thus the VLS mechanism cannot be excluded, although no catalytic metal particles were used and no signs of droplet-like shapes were found on the ZnO nanowire tips. The presented ZnO nanowire synthesis method is comparable to [229], where Zn powder was evaporated at temperatures between 450-600 °C in a furnace under a constant Ar flow. Differences in nanowire morphology, density and vertical alignment compared to this study may be explained by the choice of different substrates and vapor transport conditions.

For structural characterization, ZnO nanowires were transferred to TEM grids (Quantifoil R 2/2) and were further characterized using a FEI Tecnai F20 at an electron beam energy of 200 keV by the Institute for Electron Microscopy, Graz University of Technology. In Fig.4.11a, a high resolution TEM image of a single ZnO nanowire can be seen validating the single crystalline structure. The growth direction was found to be [001], which was

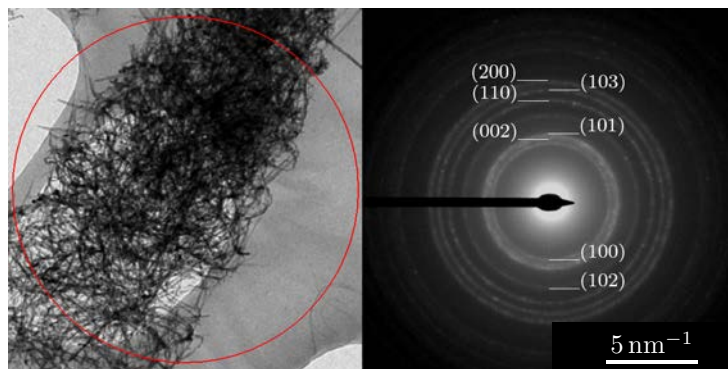
identified in literature as one of the preferred growth directions of ZnO [210]. Along the ZnO nanowire several planar defects perpendicular to the growth direction were observed, which may possibly be attributed to stacking faults as this type of two-dimensional defect is most frequently observed in ZnO nanowires [230]. However, further TEM analysis is proposed in this matter for proper interpretation of the defect structure.

Selected area electron diffraction was performed on a ZnO nanowire bundle and ring-shaped diffraction patterns were achieved (Fig.4.11b). The diameters of the rings could be related to different lattice planes of the hexagonal ZnO crystal structure thus confirming the material composition of the synthesized nanowires.

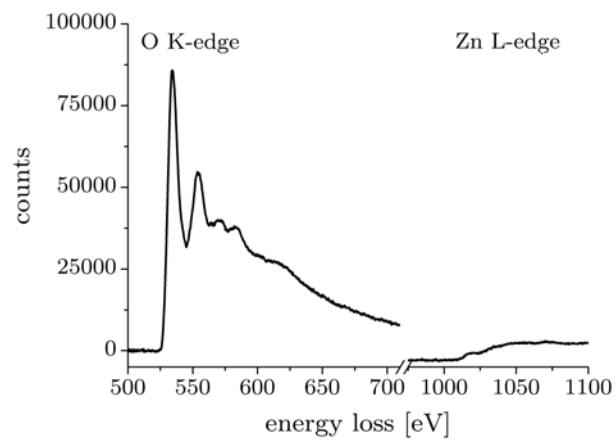
An electron energy loss spectrum of a single ZnO nanowire can be seen in Fig.4.11c. The results show excellent resolution of the near edge line structure (in particular for the O K-edge) and are in good agreement with literature reports [231–233].



(a) High resolution TEM of single ZnO nanowire



(b) Selected area electron diffraction of ZnO nanowire bundle



(c) Electron energy loss spectroscopy of single ZnO nanowire

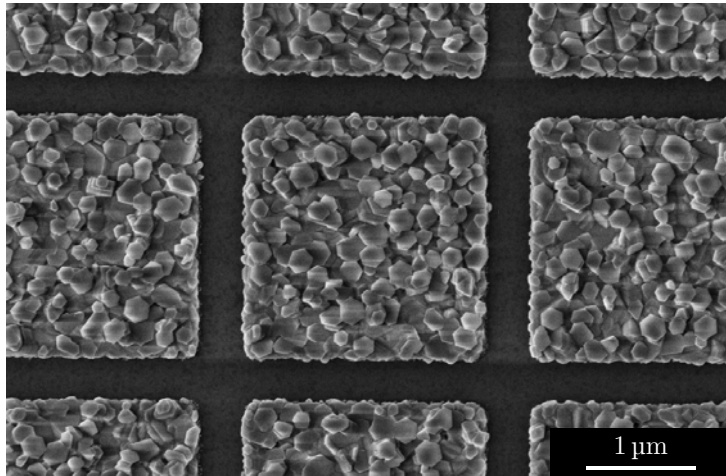
Figure 4.11: Characterization of ZnO nanowires synthesized by vapor phase growth



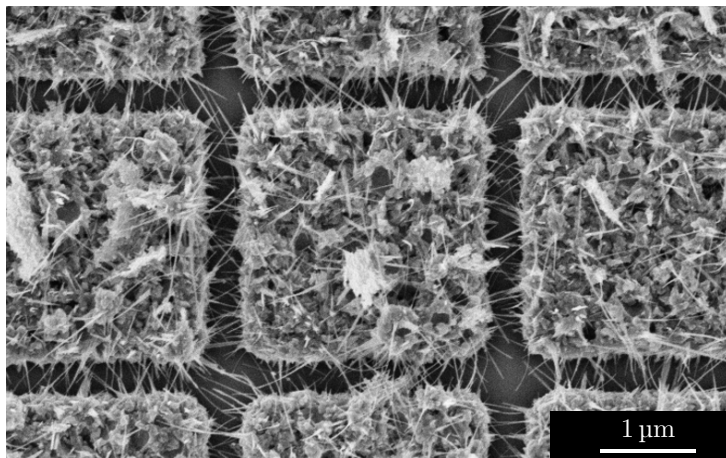
### 4.2.3 Thermal Oxidation of Evaporated Zn Structures

For the patterning of thermally evaporated Zn structures, a PMMA electron beam lithography step (writefield size  $100\times 100\ \mu\text{m}$ ) was performed on Si substrates with 300 nm thermal  $\text{SiO}_2$ . Prior to this process Ti/Au alignment markers were defined by a photolithographic lift-off process. The process parameters for both lithography processes can be found in Appendix A. After development, a Ti/Zn film (5 nm and 250 nm, respectively) was deposited by thermal evaporation and metal lift-off was performed. Regular arrays of quadratic Zn squares (Fig.4.12a) were achieved with an edge length of  $2.5\ \mu\text{m}$  and an initial gap distance around 500 nm. For ZnO nanowire synthesis, the samples were thermally oxidized on a hotplate in ambient atmosphere ( $T = 410\ ^\circ\text{C}$ , 1 h). As can be seen in Fig.4.12b, the gaps between the adjacent oxidized Zn structures were bridged by suspended ZnO nanowires. Their dimensions were estimated by SEM imaging; the diameters typically ranged from 10 nm to 30 nm, while lengths were most commonly below 1-2  $\mu\text{m}$ .

The presented ZnO nanowire synthesis results are very well comparable to literature reports [224,226]. In particular, the authors of [225] used an evaporated Zn film with a similar morphology as substrate for the formation of ZnO nanowires by thermal oxidation. The growth mechanism was explained by stress-driven mass diffusion of Zn ions towards the surface and ZnO nanowire growth from initial ZnO seeds at the surface (see Chapter 4.2.1). As the Zn thin film substrate, thermal oxidation parameters as well as ZnO nanowire growth are well comparable to the results presented here, it is reasonable to assume that similar growth mechanisms are present. However, the Zn thin film substrate in [225] was not microstructured, which might have an influence on mechanical stress distribution. Thus further experiments with different Zn structure sizes and shapes are suggested for evaluation of this influencing factor. Furthermore, additional TEM studies are proposed in order to characterize the crystalline structure of the synthesized ZnO nanowires, which could probably lead to further insights in the growth mechanism.



(a) Thermally evaporated Zn structures

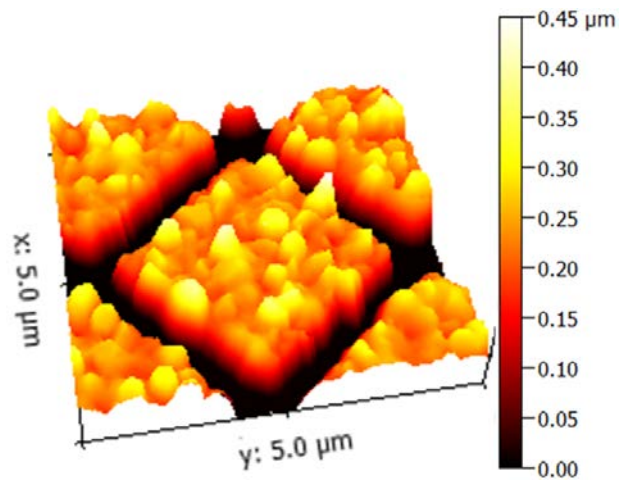


(b) ZnO nanowire growth between adjacent oxidized Zn structures

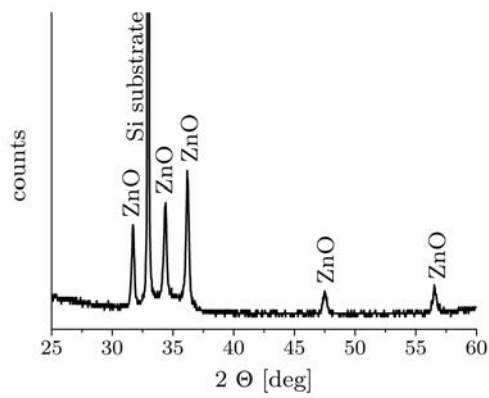
Figure 4.12: ZnO nanowire synthesis by thermal oxidation of Zn structures  
( $T = 410^{\circ}\text{C}$ , ambient atmosphere)

As can be seen from the SEM image of the Zn structures before thermal oxidation (Fig.4.12a), the thermally evaporated Zn film exhibited distinct faceting, large grain sizes and a rough surface topography. ZnO nanowire growth by thermal oxidation is strongly influenced by Zn substrate morphology as was reported in [227]. Therefore atomic force microscopy (AFM) measurements were used for characterization of the Zn structures. A Molecular Imaging Pico Plus AFM was used in acoustic AC mode for measurements of the surface topography, which can be seen in Fig.4.13a. An average film thickness around 250 nm and a root-mean-square value of the surface roughness of approximately 40-55 nm were found. For constant Zn deposition parameters reproducible thin film morphologies were achieved in repeated experiments. It is assumed that the high surface roughness plays an important role during ZnO nanowire synthesis as suggested in [227], which could be verified by additional experiments using different Zn deposition methods.

Similar as for the thermally oxidized Cu structures, additional samples with large area arrays of Zn structures were fabricated for XRD experiments. In order to achieve comparable ZnO nanowire synthesis results, the same substrates, process steps, material deposition methods and thermal oxidation parameters were used as described above. XRD measurements were performed by specular scans using a Siemens D501 diffractometer in Bragg-Brentano geometry. The database PDF2 from the International Center for Diffraction Data (ICDD) was used for qualitative phase analysis. The as-deposited Zn film showed preferred orientation in the [002] direction, which follows from the experimental peak intensity ratios, which were different compared to a polycrystalline reference (number 4-0381, PDF2 database, ICDD). On the thermally oxidized sample, polycrystalline ZnO with no preferred grain orientation was found (see Fig.4.13b).



(a) AFM characterization before thermal oxidation



(b) XRD characterization after thermal oxidation

Figure 4.13: Characterization of Zn structures before and after thermal oxidation

## 5 Gas Measurements: Methods and Target Gas Properties

### 5.1 Gas Sensor Assembly

The assembly of functional conductometric gas sensors comprised several steps: First of all, nanowire-based devices were fabricated on Si substrates, which will be described in detail later for the different types of sensors. In order to heat the nanowire devices to the desired operation temperature they were glued (Aremco Ceramabond 865) to the backside of a  $1 \times 1.5$  cm Si chip together with two commercially available microheaters (10x2 Pt6,8, Delta-R) and a Pt100 temperature sensor (4x1 Pt100, Delta-R). These discrete electronic components were connected to solder pads on a specifically designed ceramic sensor carrier (Fig.5.1), which was fabricated by the Institute of Sensor and Actuator Systems (Vienna University of Technology). The solder wires provided the required electrical connections and the mechanical support of the assembled gas sensor. Thermal conduction to the ceramic carrier and thus the whole measurement chamber was reduced due to this configuration, which is important in order to avoid undesired heating of the surrounding gas atmosphere. Electrical connections to the sensor devices were established by wedge bonding (F & K Delvotec 53XX-BDA; 25  $\mu\text{m}$  thick Au wire) between contact pads on the sensor chip and Au lines on the ceramic carrier.

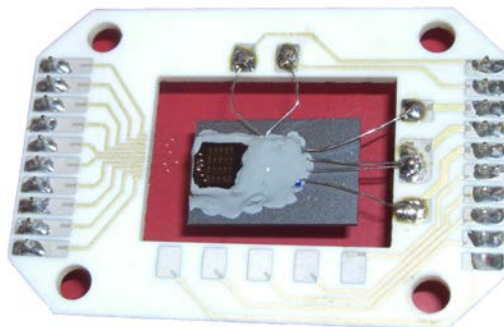


Figure 5.1: Assembled gas sensor connected to the ceramic sensor carrier

## 5.2 Gas Sensor Testing System

The investigated sensor devices were tested in an automated gas sensor testing system (Fig.5.2), which was controlled by a PC using a program written in the LabView development environment (National Instruments). Mass flow controllers (MFC Bronkhorst F-201CV) were used to control carrier gas flow, target gas concentration and relative humidity level. A detailed description of the test gas compositions can be found in Appendix B. The relative humidity of the carrier gas was measured by a commercial humidity sensor (Kobold AFK-E). All gas measurements in this thesis were carried out under a constant total gas flow of 1000 sccm. The gas sensor operation temperature was controlled by adjusting the current through the two microheaters (current source Thurbly Thandar Instruments PL330P) using the Pt100 temperature sensor signal (multimeter Agilent Technologies 34401A) and a PID control implemented in the measurement program. The electrical resistance of the sensor devices was measured by a Keithley 2400 SourceMeter in constant current operation in either two-point or four-point configuration.

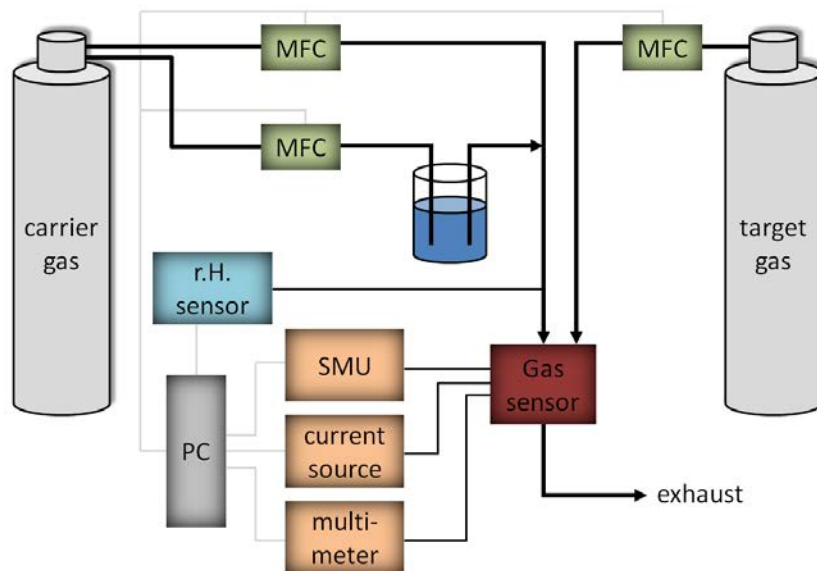


Figure 5.2: Schematics of the gas sensor setup

## 5.3 Properties of Selected Target Gases

In this thesis, several different nanowire-based devices will be presented for sensing of three target gas molecules:

- water vapor  $\text{H}_2\text{O}$
- carbon monoxide  $\text{CO}$
- hydrogen sulfide  $\text{H}_2\text{S}$

In the following, the interest for the detection of these species will be briefly motivated and their most basic properties will be summarized. Literature models for interaction mechanisms between the target gases and metal oxide surfaces will be discussed with the respective gas sensing results.

### 5.3.1 Water Vapor $\text{H}_2\text{O}$

Water vapor plays an important role in the majority of practical gas sensing applications due to its presence in ambient atmosphere. The interaction of  $\text{H}_2\text{O}$  molecules with metal oxide surfaces may be utilized for relative humidity monitoring, but, more important, influences the sensor response during the detection of other target gases and thus has to be taken into account in most cases.

The water molecule is characterized by a H-O-H bond angle of  $104.5^\circ$  and a bond length of  $0.96 \text{ \AA}$ . It is a polar molecule due to the stronger electronegativity of O compared to H resulting in partial charges and a net dipole moment of  $1.83 \text{ D}$  along the symmetry axis. The two H atoms form covalent bonds to the O atom, which has two non-bonding orbitals with two electrons each left. The O-H groups act as H-bond donors and the two non-bonding orbitals are H-bond acceptors, which means that one water molecule may establish four H-bonds [234]. The dissociation energy for removal of the first H atom from the water molecule is  $499 \text{ kJ/mol}$ , whereas it is  $428 \text{ kJ/mol}$  for the second H atom [235].

### 5.3.2 Carbon Monoxide CO

Carbon monoxide CO is a odorless, colorless and tasteless gas which is produced during the incomplete combustion of carbon compounds. Common environmental source are central heating, motor vehicle exhaust or open fires. The toxicity of CO arises from its much higher affinity to bond to hemoglobin (carrier molecule for oxygen transport in blood) compared to O<sub>2</sub>. In case of CO exposure the amount of O<sub>2</sub> carried by hemoglobin in the blood flow is reduced leading to hypoxia with various symptoms such as headaches, dizziness, nausea or even death [39]. Ambient air concentrations of CO in areas with insufficient ventilation (for instance multistorey car parks or road tunnels) or in homes with gas appliances may exceed 100 ppm. For comparison, the World Health Organization suggested a maximum eight hour time-weighted average exposure to CO of 10 ppm in an air quality guideline [40], which highlights the relevance of CO sensors for environmental monitoring applications.

The carbon monoxide molecule is formed due to a triple C-O bond with a bond length of 1.1 Å. It has a small dipole moment of 0.11 D with a negative partial charge of C. The dissociation energy of CO is comparatively high with a value of 1070 kJ/mol [235].

### 5.3.3 Hydrogen Sulfide H<sub>2</sub>S

Hydrogen sulfide H<sub>2</sub>S is formed by reactions of anaerobic bacteria with organic substances [236]. Typical sources are natural gas, swamps, sewers or geothermal activity. The human nose has a very low odor threshold to the rotten egg smell of H<sub>2</sub>S between 10 and 300 ppb. However, during exposure to higher concentrations the olfactory senses become paralyzed and thus insensitive to the distinct smell. After inhalation H<sub>2</sub>S is dissociated in blood leading to elevated S levels in tissue, which results in nausea, headaches, eye and lung irritation and respiratory paralysis at high concentrations. H<sub>2</sub>S exposure is the second most common cause of fatal gas inhalation intoxi-



cations at the working place (after CO poisoning) demonstrating the high relevance of H<sub>2</sub>S detection for safety applications [41]. According to an European Commission directive of 2009, the eight hour time-weighted average exposure to H<sub>2</sub>S must not exceed 5 ppm in order to ensure workers' health and safety [237].

The hydrogen sulfide molecule has a H-S-H bond angle of 92.5° [236] and a bond length of 1.34 Å [238]. Despite the structural similarities to the water molecule, H<sub>2</sub>S has different chemical properties. It does not form strong H-bonds due to the lower polarity (0.97 D [239]) and it typically shows higher reactivity because of the weaker S-H bonds compared to the O-H bonds [236]. The dissociation energy for the removal of the first and second H atom is 381 kJ/mol and 352 kJ/mol, respectively [240].

## 6 Single Nanowire Devices

In general, two different approaches were chosen for the fabrication of single nanowire devices in two-point and four-point configuration. Fig.6.1 shows a schematic illustration of the different process flows, which are also described in more detail in the chapters of the respective nanowire devices.

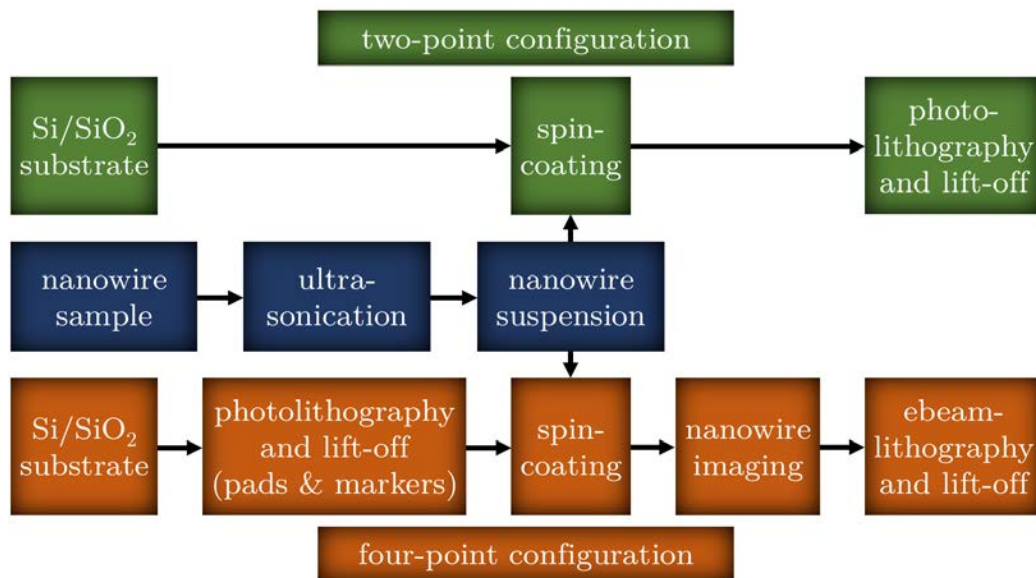


Figure 6.1: Process flows for single nanowire device fabrication (two-point and four-point configuration)

### 6.1 Single CuO Nanowire Devices

#### 6.1.1 Two-Point Configuration

Single CuO nanowire devices in a two-point configuration were fabricated by a single photolithographic step. First, a CuO nanowire suspension was obtained by ultrasonication of CuO nanowire samples (Cu wires thermally oxidized at 500 °C for 200 min as described in Chapter 4.1.2) in isopropanol. The nanowire suspension was then spin coated (Ramgraber M-Spin150; 1000 rpm, 35 s) on 2×2 cm Si substrates covered with 300 nm thermal SiO<sub>2</sub>. Next, pho-

tolithography was performed using an image reversal resist (see Appendix A for process parameters) followed by thermal evaporation and lift-off of the metal layer. The mask design consisted of comb-like electrodes with distances between 5  $\mu\text{m}$  and 25  $\mu\text{m}$ . In Fig.6.2, typical examples for such single CuO nanowire devices in a two-point configuration are shown.

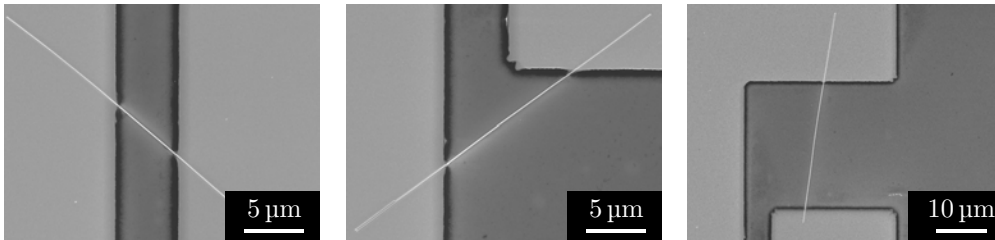


Figure 6.2: Single nanowire devices in a two-point configuration (Pt electrodes)

The advantages of this fabrication process are simplicity and the possibility for efficient realization of a large number of CuO nanowire devices. However, a certain degree of randomness is inherent to this method as can be seen from the CuO nanowire devices in Fig.6.2, where all contacts show different lengths of metal-semiconductor interfaces.

Various different contact materials and process parameters were investigated regarding linearity of the I-V characteristics, device-to-device reproducibility and thermal stability. Electrical measurements were performed at room temperature in ambient air conditions using a Sues Microtec probe station and an Agilent 4156C parameter analyzer. The best results were achieved using a Pt or a Ni/Au metallization and an annealing step at 400  $^{\circ}\text{C}$  for 5 min on a hotplate in ambient atmosphere. An example for the I-V characteristics of a single CuO nanowire device contacted by Pt electrodes (thickness around 40 nm) can be seen in Fig.6.3a. In this case, Ohmic properties were observed for a CuO nanowire with a diameter of 144 nm and a contact spacing of 25.4  $\mu\text{m}$ . The electrical conductivity was estimated assuming a cylindrical nanowire cross section using

$$\sigma = \frac{4GL}{D^2\pi}$$

with the nanowire length L, the diameter D and the device conductance G.

The conductivity was found to lie around 0.5 S/m. However, the contribution of the two contacts to the overall resistance could not be evaluated in this device configuration. Transconductance measurements were performed by contacting the Si substrate with conductive silver paste and using it as a back gate for nanowire field effect transistor operation. Results are shown in Fig.6.3b for a constant drain-source voltage of 1 V. The CuO nanowire device showed p-type semiconductor characteristics, which is consistent with literature reports [51, 52].

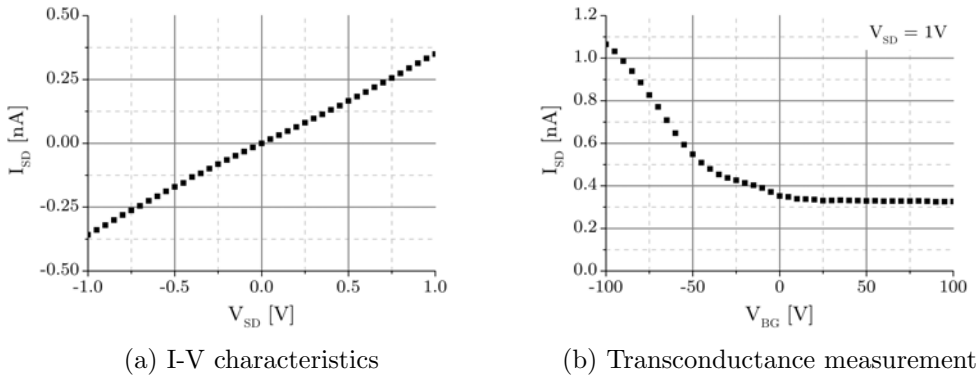


Figure 6.3: Electrical characterization of a single CuO nanowire (two-point configuration, channel length 25.4  $\mu\text{m}$ , diameter 144 nm, Pt electrodes)

The field effect mobility  $\mu$  was estimated using an analytical formula derived for a metallic cylinder-plane configuration [241, 242],

$$\mu = \frac{dI_{SD}}{dV_{BG}} \frac{L}{2\pi\epsilon_0\epsilon_{eff}V_{SD}} \operatorname{arcosh}\left(\frac{R+t}{R}\right)$$

with the transconductance  $dI_{SD}/dV_{BG}$ , the nanowire length  $L$  and radius  $R$ , the oxide thickness  $t$  and the source-drain voltage  $V_{SD}$ . An effective dielectric constant  $\epsilon_{eff} = 2.2$  was used [241] in order to take into account that the CuO nanowire was surrounded by  $\text{SiO}_2$  as well as air. For the particular device presented here, the field effect mobility was approximately  $6 \cdot 10^{-2} \text{ cm}^2 \text{ V}^{-1} \text{ s}^{-1}$ , which is well comparable with literature results for CuO single crystals [243] and CuO nanowires [31].

The estimated hole concentration was  $6 \cdot 10^{17} \text{ cm}^{-3}$  using

$$p = \frac{\sigma}{\mu e} = \frac{4GL}{D^2\pi\mu e}.$$

The electrical properties of several CuO nanowire devices on the same substrate with different diameters (75 - 211 nm) and channel lengths (5.2 - 25.4  $\mu\text{m}$ ) were characterized. Most commonly, the electrical conductivities  $\sigma$  ranged from 0.2 to 20 S/m and the extracted parameters  $\mu$  and  $p$  are shown in Fig.6.4. For both the field effect mobility and the hole concentration no significant dependence on the CuO nanowire diameter could be found.

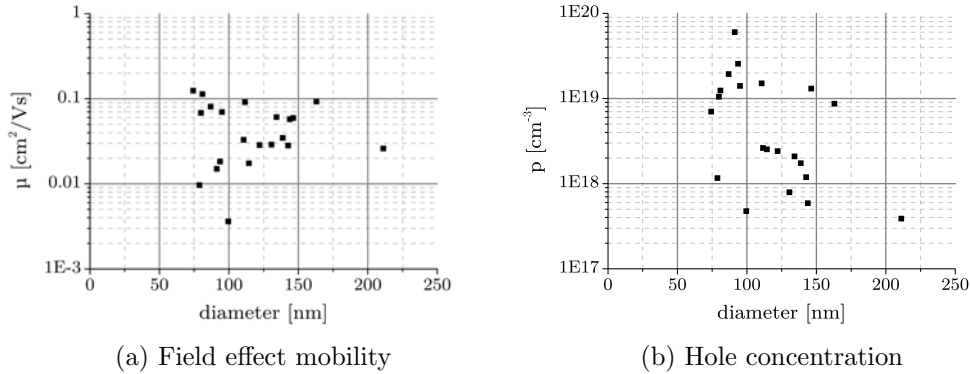


Figure 6.4: Transport parameters of single CuO nanowires (two-point configuration)

However, it has to be considered that there are various potential error sources inherent to this type of measurements [242]. The used model was derived for a infinitely long, metallic cylinder-plane configuration with a cylinder entirely embedded in a dielectric medium. In a CuO nanowire device with finite channel length the nanowire-gate coupling is perturbed due to stray electric fields in the vicinity of the source and drain contacts. Moreover, the semiconducting material properties may lead to a nonuniform potential and charge distribution within the nanowire, which possibly causes considerable deviations from the metallic model. Another uncertainty is the effective dielectric constant (literature values range from 1.95 [244] to 2.5 [245] in the case of  $\text{SiO}_2$ ), which was introduced to account for the inhomogeneous dielectric surrounding of the nanowire. Furthermore, faceted nanowire surfaces

may lead to differences in nanowire-gate coupling [241] and to errors in the determination of the cross-section area. As the single CuO nanowire devices used in this analysis were contacted in a two-point configuration, contact resistances also constitute a potential error source, which would lead to an underestimation of hole concentrations. In summary, the extracted parameters should be considered as rather rough estimations and device-to-device variations of the electrical transport parameters may be caused by different nanowire properties (e.g. due to distinct crystal orientations) but are certainly also influenced by the various error sources.

CuO nanowires in a two-point configuration were operated as conductometric gas sensing devices for the detection of water vapor and CO. However, results are not shown here as focus is put on CuO nanowires in a four-point configuration due to the possibility of more precise measurements without the influence of contact resistances.

### 6.1.2 Four-Point Configuration

Single nanowire devices in a four-point configuration were fabricated as follows: First, photolithography was performed on  $2 \times 2$  cm Si substrates covered with 300 nm thermal SiO<sub>2</sub> using an image reversal photoresist (see Appendix A for process parameters). Next, thermal evaporation of a Ti/Au layer (thickness 10 nm and 200 nm, respectively) and lift-off was performed in order to obtain an array of contact pads and electron beam alignment markers (see Fig.6.5a). Subsequently, nanowire samples (Cu wires thermally oxidized at 500 °C for 200 min; see Chapter 4.1.2) were ultrasonicated in isopropanol in order to obtain a nanowire suspension, which was spin coated (Ramgraber M-Spin150; 1000 rpm, 35 s) on the pre-patterned Si substrates. SEM imaging was used for choosing single nanowires at appropriate positions as can be exemplarily seen in Fig.6.5b. For each single nanowire, a specific layout was designed in order to contact it with the large Ti/Au pads in a four-point configuration. A PMMA electron beam lithography process (see Appendix A for process parameters) was performed using a writefield size of

100×100 μm. In order to compensate errors of the piezo stage in the SEM and ensure precise alignment, an automatic writefield alignment procedure was used. After development, the nanowire sample was mounted in the thermal evaporator and an Ar plasma cleaning was performed for 30 min before deposition of the contact electrodes. Finally, metal lift-off was performed resulting in a typical device as shown in Fig.6.5c.

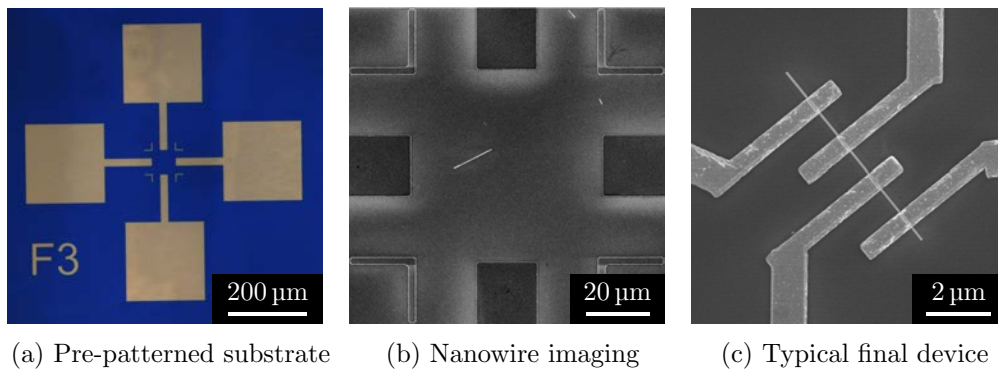


Figure 6.5: Fabrication of single CuO nanowire devices in a four-point configuration

The four-point configuration is advantageous as it allows the evaluation of the contributions of nanowire channel and metal-semiconductor contacts to the overall device resistance. Although a more precise characterization of the CuO nanowire electrical properties is possible, it has to be noted that the required fabrication technology is considerably more time-consuming than the process based on a single photolithographic step (Chapter 6.1.1). Furthermore, an influence of electron beam exposure on the CuO nanowire surface properties during imaging and electron beam lithography cannot be excluded.

In the following, results will be shown for single CuO nanowires contacted with a thermally evaporated Ni/Au layer (thickness 10 nm and 200 nm, respectively). The contact properties could be considerably improved by using a thermal annealing step at 400 °C for 5 min. This metallization showed excellent results in terms of long term stability at elevated temperatures, which is particularly important for the gas sensing operation. In Fig.6.6 a comparison of the IV characteristics in two-point and four-point configuration of a single CuO nanowire device (channel length 1.9 μm, diameter 113 nm) can

be seen. A Sues Microtec probe station and an Agilent 4156C parameter analyzer were used for the measurements at room temperature in ambient air conditions. The IV characteristics at 350 °C were measured on assembled gas sensor devices (Chapter 5.1) in the gas sensor testing system (Chapter 5.2) by means of a Keithley 2400 SourceMeter.

In the room temperature case (Fig.6.6a) symmetric non-linear behavior was found for two-point configuration measurements. These results can be interpreted by a back-to-back Schottky barrier model similar as was proposed in [246] for SnO<sub>2</sub> nanowires. The overall device resistance consists of a forward-biased Schottky barrier, the CuO nanowire resistance and a reverse-biased Schottky barrier. The current in the CuO nanowire is expected to be limited by thermionic emission in the reverse-biased Schottky barrier. It has to be noted that the channel lengths of CuO nanowires contacted in a four-point configuration were considerably lower than for the two terminal devices (0.9-1.9 μm compared to 5-25 μm). Thus a larger influence of the contacts was observed in two-point measurements. The IV characteristics in four-point configuration revealed the significant contact contribution to the overall device resistance and CuO nanowire conductivity was calculated to lie around 2 S/m. At T=350 °C (Fig.6.6b) small differences between measurements in two-point and four-point configuration were observed. The quasi-ohmic device characteristics are interpreted by enhanced thermionic emission at elevated temperatures. Moreover, CuO nanowire conductivity decreased by more than one order of magnitude.



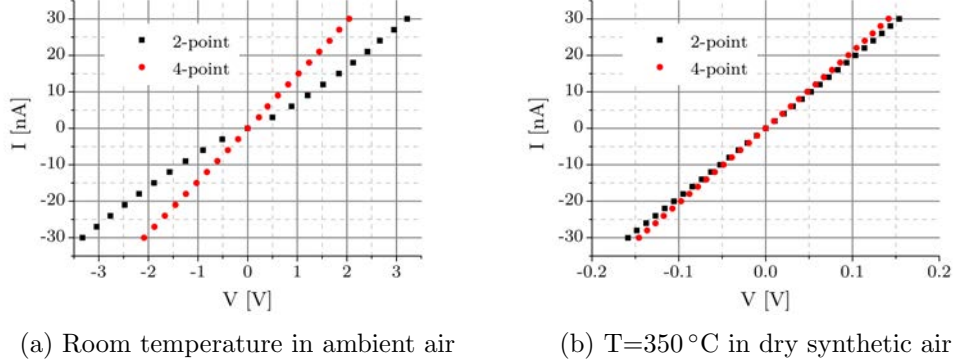


Figure 6.6: Two-point and four-point IV characteristics of a single CuO nanowire device (channel length 1.9  $\mu\text{m}$ , diameter 113 nm, Ni/Au electrodes)

For further characterization of the Ni/Au contact metallization fabricated by electron beam lithography, cross-sectional transmission electron microscopy was performed by the Institute for Electron Microscopy, Graz University of Technology. The sample was covered with  $\sim 500$  nm of Pt and a TEM lamella was prepared using a FIB/SEM Dual Beam Microscope FEI NOVA200. A FEI Tecnai F20 transmission electron microscope at an electron beam energy of 200 keV was used for image acquisition. In Fig.6.7, the cross-section of a single contacted CuO nanowire is shown. First of all, a twin boundary could be observed in the lower image half. This growth behavior is in accordance with the previous CuO nanowire characterization results (Chapter 4.1.2), which revealed repeated occurrence of twinning defects. Unfortunately, electron spectroscopy could not be performed due to sample damage during long-time electron beam exposure. From the imaging results it was inferred that the CuO nanowire was covered by two polycrystalline layers with a thickness around 10 nm and 200 nm, thus most probably metallic Ni and Au. The metal-semiconductor interface appeared sharp and consequently no ternary phases seemed to have formed during the annealing step. However, interdiffusion of Ni and Au was reported to occur on thin film samples in a temperature range of 200-500  $^{\circ}\text{C}$  [247] and thus also has to be assumed in this case.

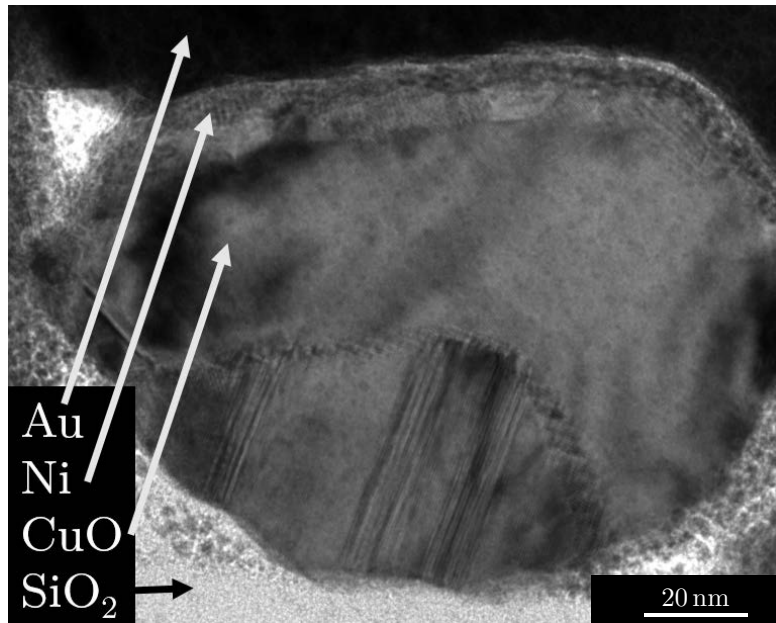


Figure 6.7: Cross-sectional transmission electron microscopy of Ni/Au contacts

The temperature dependence of CuO nanowire conductivity was further characterized by additional measurements on four devices in dry synthetic air (see Fig.6.8). CuO nanowire conductivity is expected to be influenced by changes of hole concentration and mobility as well as coverage with chemisorbed oxygen ions. The four devices with various diameters showed comparable temperature dependence of electrical conductivity with an increase of more than one order of magnitude at  $T=350\text{ }^{\circ}\text{C}$  compared to room temperature. The room temperature values for electrical conductivity were comparable to those estimated by two-point measurements (Chapter 6.1.1), which supports the validity of the previous measurements.

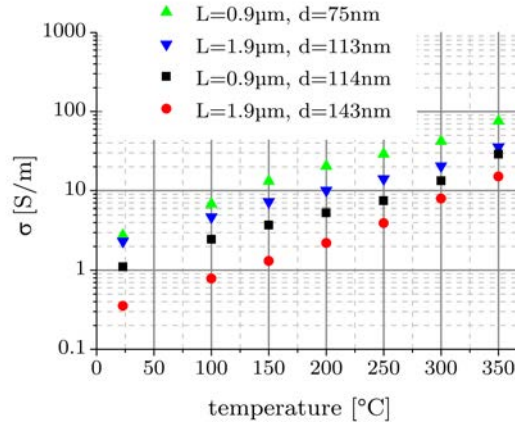


Figure 6.8: Temperature dependence of electrical conductivity of four CuO nanowires

Gas sensing characterization was performed on various CuO nanowires in four-point configuration. Typical results can be seen in Fig.6.9, where simultaneous resistance measurements on two devices during humidity as well as CO exposure are shown. Methods described in Chapter 5 were applied and sensor operation temperatures from 300-350 °C were chosen. As background gas synthetic air was used and the total gas flow was kept constant at 1000 sccm.

CuO nanowire resistance values were found to increase for increasing water vapor concentrations ranging from around 30% to 70% relative humidity, as can be seen in Fig.6.9a. The relative resistance changes of both CuO nanowire sensors were well comparable for all three investigated operation temperatures of  $T=300\text{ }^{\circ}\text{C}$ ,  $T=325\text{ }^{\circ}\text{C}$  and  $T=350\text{ }^{\circ}\text{C}$ . In repeated experiments reproducible results were achieved validating the long-term stability of the sensor response to humidity.

During CO exposure at  $T=350\text{ }^{\circ}\text{C}$  increasing CuO nanowire resistance values were observed for increasing concentrations from 50 to 300 ppm (see Fig.6.9b). Again no significant differences of the CO sensing properties of the two presented devices were found. However, repeated experiments lead to decreasing relative resistance changes during CO exposure.

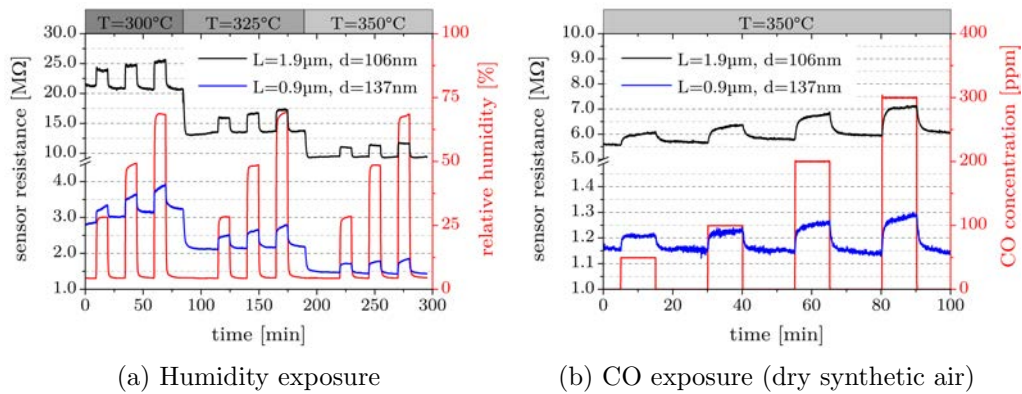


Figure 6.9: Gas measurements on two single CuO nanowires (four-point configuration)

### 6.1.3 Single Suspended CuO Nanowire

For the fabrication of single suspended CuO nanowire devices a novel method was developed, which comprised the following steps: First, CuO nanowires were synthesized by thermal oxidation of a copper wire at 500 °C for 200 min in ambient atmosphere by a resistive heating method, which is described in Chapter 4.1.2. Next, a CuO nanowire suspension in isopropanol was drop-coated on Si/SiO<sub>2</sub> substrates with electroplated Cu structures contacted by a Ti/Au (thickness 5 nm and 200 nm, respectively) metallization layer (see Fig.6.10a). The Cu structures had a width of 25 μm, a thickness of 2.5 μm and a gap distance of 5 μm in between. A detailed description of the fabrication process of the electroplated Cu structures can be found in Chapter 4.1.3. Single CuO nanowires bridging the Cu lines were realized (see Fig.6.10b) by choosing a proper nanowire concentration in the suspension. Eventually, the samples were heated up to 200 °C and 400 °C in ambient atmosphere for 30 min and 60 min, respectively. Due to thermal oxidation of the Cu structures copper oxide growth around the CuO nanowire (see inset of Fig.6.10b) lead to electrical contact formation.

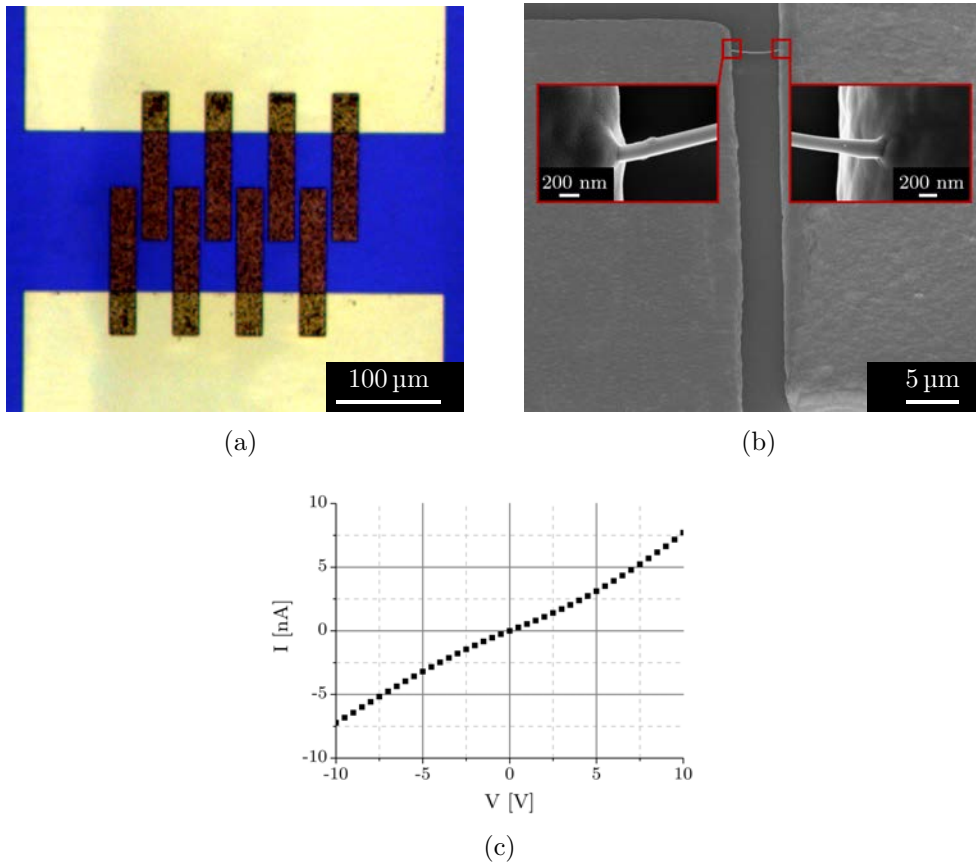


Figure 6.10: Fabrication and characterization of single suspended CuO nanowire devices. a) Cu structures with Ti/Au contact pads, b) suspended CuO nanowire bridging oxidized Cu structures and c) IV characteristics (room temperature, ambient atmosphere).

In the following, results on a single suspended CuO nanowire device (length  $\sim 5 \mu\text{m}$ , diameter 170 nm) will be presented. The room temperature IV characteristics were measured (Suess Microtec probe station, Agilent 4156C parameter analyzer) in ambient air conditions and are shown in Fig.6.10c. Only minor nonlinear behavior was observed around 0 V, which indicates that good contact properties can be achieved by this novel contacting method relying on growth of a copper oxide layer around a single CuO nanowire. The electrical resistance of the single suspended CuO nanowire was measured for different temperatures in dry synthetic air using the assembled gas sensor configuration (gas sensor testing system, Keithley 2400 SourceMeter). The temperature dependence was very comparable to the results on single

CuO nanowires in four-point configuration (Fig.6.8). However, electrical conductivity is not evaluated in this case due to uncertain series resistance of the oxidized Cu layer and imprecise length determination of the bent CuO nanowire.

The gas sensing performance of the single suspended CuO nanowire were characterized in a similar way as in the previous chapter. The sensor device was operated in a temperature range of 300-350 °C and was exposed to humidity as well as CO using synthetic air as background gas and a constant total gas flow of 1000 sccm.

Resistance changes of the single suspended CuO nanowire during humidity and CO exposure are shown in Fig.6.11a and Fig.6.11b, respectively. The results are well comparable to the gas sensing properties of single CuO nanowires in a four-point configuration (Chapter 6.1.2). Increasing resistance values for increasing water vapor as well as CO concentrations were again observed.

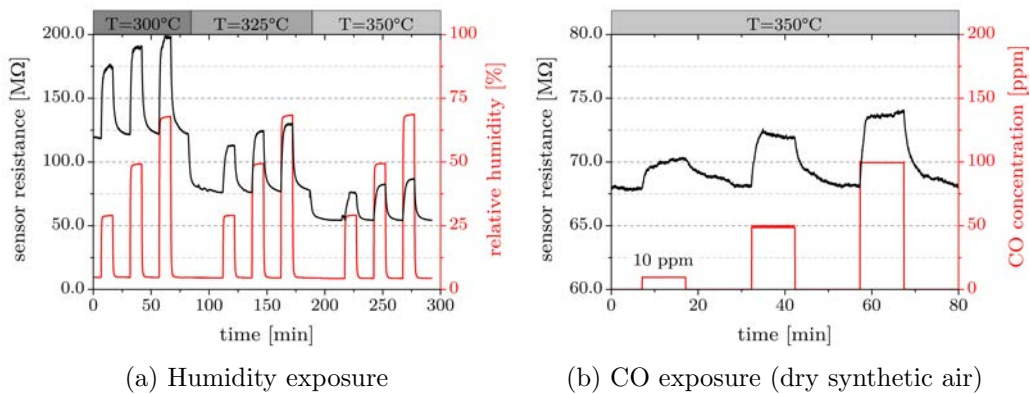
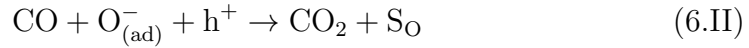
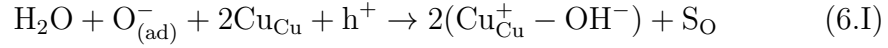


Figure 6.11: Gas measurements on single suspended CuO nanowire

#### 6.1.4 Discussion

The detection of water vapor and CO was explained by the following interaction mechanisms with chemisorbed oxygen species on CuO surfaces [78]:



As can be seen, a hole is consumed in both of the proposed reactions leading to a decrease of carrier concentration in the CuO surface accumulation layer and thus a decrease of conductivity. The experimentally observed resistance changes are in accordance with this sensing mechanism model.

The CO sensor response was evaluated using  $S = R_{\text{CO}}/R_{\text{air}}$  for four different single CuO nanowires in a four-point configuration and the single suspended CuO nanowire. The results shown in Fig.6.12 indicate a linear concentration dependence with similar slopes for all the investigated devices. For the suspended CuO nanowire it can be expected that the specific device configuration with a single nanowire entirely surrounded by the gas atmosphere is beneficial for the sensor performance. In general, no pronounced CuO nanowire diameter dependence of the sensor performances was observed. As a consequence, it is assumed that the differences in CO response result from distinct nanowire faceting and surface termination, as these factors are also known to have a large impact on metal oxide gas sensing properties [26].

For all the CuO nanowire devices in a four-point configuration a decrease in CO sensor response was observed in repeated experiments. It was proposed in literature that disproportionation of CO may lead to carbon poisoning of metal oxide surfaces due to a decrease in concentration of oxygen species [248]. Thus the reduced CO response in repeated experiments is attributed to a smaller number of active surface sites for CO oxidation. However, the long-term stability of CO sensing in dry and humid atmosphere will be studied in more detail in Chapter 8.1 using a different type of sensor device.

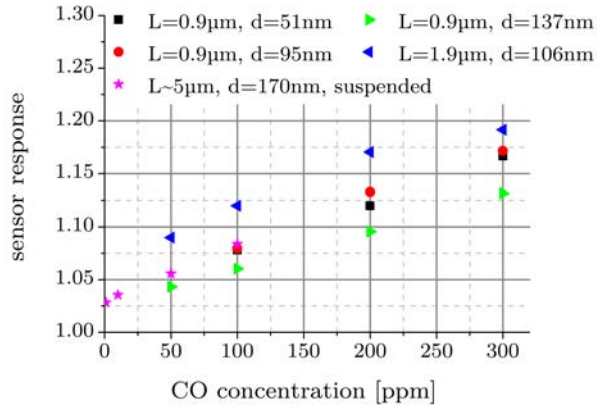


Figure 6.12: Comparison of CO response of five single CuO nanowire devices (dry synthetic air, operation temperature 350 °C)

## 6.2 Single ZnO Nanowire Devices

For the fabrication of single ZnO nanowire devices in a two-point configuration, similar process steps were used as in the case of single CuO nanowire devices (Chapter 6.1.1). ZnO nanowire samples (vapor phase ZnO nanowire synthesis as described in Chapter 4.2.2) were ultrasonicated in isopropanol resulting in a ZnO nanowire suspension, which was spin coated (Ramgraber M-Spin150; 1000 rpm, 35 s) on 2×2 cm Si substrates (300 nm thermal SiO<sub>2</sub>). Next, a lift-off process (image reversal resist; see Appendix A) was performed in order to structure the contact metallization. Again, a mask design with comb-like electrodes with distances between 5 µm and 25 µm was used.

The electrical properties of around 15 single ZnO nanowire devices contacted by either a thermally evaporated Al layer (thickness 100 nm) or a thermally evaporated Al/Au layer (thickness 100 nm/100 nm) were investigated. Room temperature IV characteristics were measured in ambient air using a Sues Microtec probe station and an Agilent 4156C parameter analyzer. All devices showed Ohmic behavior with resistance values between 45 kΩ and 4.2 MΩ. However, at high bias levels non-linearities and device failures were observed, which was attributed to Joule heating of the single ZnO nanowires. In or-



der to verify this assumption, additional measurements were carried out in controlled gas atmosphere as changes in surface reactivity for different bias levels are a strong indication for self-heating effects [34].

Results are shown for the single ZnO nanowire device (Al/Au electrodes) depicted in Fig.6.13a, which has a channel length around 6  $\mu\text{m}$  and a diameter of 228 nm. The room temperature IV characteristics in ambient atmosphere can be seen in Fig.6.13b. The electrical conductivity  $\sigma = 4GL/D^2\pi$  is approximately 15 S/cm, which is in fair agreement with the values in [249]. However, it has to be noted that literature results for ZnO nanowire conductivity differ by eight orders of magnitude due to several influencing factors [250].

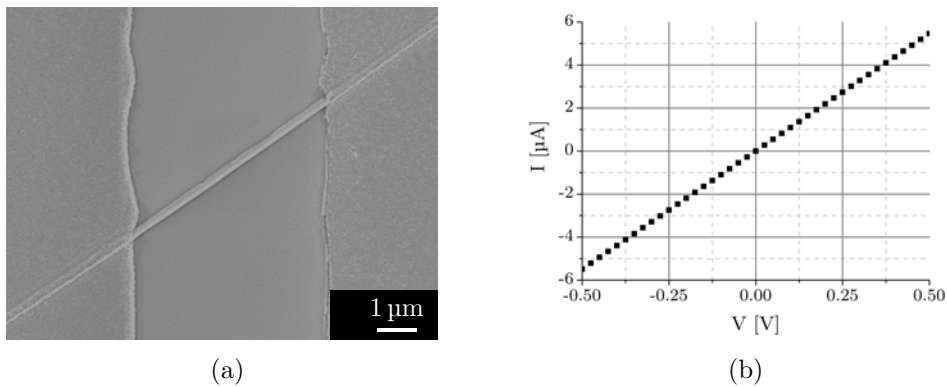


Figure 6.13: a) Single ZnO nanowire device (channel length 6  $\mu\text{m}$ , diameter 228 nm, Al/Au contacts) in a two-point configuration and b) the IV characteristics (room temperature, ambient air)

Before the gas sensing experiments, the sample was cleaned by an oxygen plasma treatment in order to remove photoresist residues. The Si substrate was glued to a printed circuit board and electrical connections to the ZnO nanowire were established by wedge bonding to the Al/Au contact pads (F & K Delvotec 53XX-BDA; 25  $\mu\text{m}$  thick Au wire). Appropriate device biasing conditions were determined empirically. In Fig.6.14, the normalized electrical resistance of the single ZnO nanowire during exposure to three humidity pulses is shown. Three measurements were performed with different power dissipations of 11.5  $\mu\text{W}$ , 1.6 mW and 2.2 mW. During humidity exposure no significant resistance change was observed for the lowest bias level, whereas

nanowire conductivity increased in the other two cases. This sensor behavior is attributed to enhanced surface reactivity due to Joule heating of the ZnO nanowire, which is also supported by the faster response kinetics for the power dissipation of 2.2 mW compared to the measurement at 1.6 mW. The interaction with water vapor typically results in a resistance decrease of n-type metal oxide semiconductors, which was also reported for other ZnO nanowire based devices [251]. The comparatively low gas response of only few percent can be explained by the low surface to volume ratio due to the large ZnO nanowire diameter of 228 nm. For a more detailed discussion of the sensing mechanism additional measurements for estimation of the surface temperature would be needed, for instance by correlation of sensing results obtained with nanowire self-heating and with external heating elements [35].

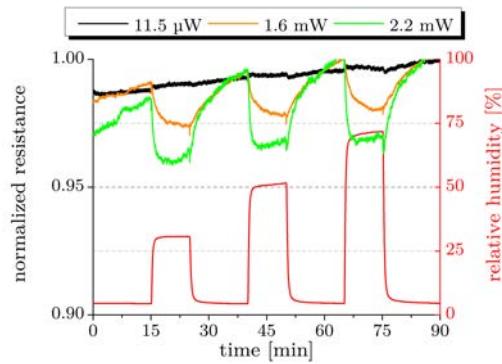


Figure 6.14: Electrical resistance of single ZnO nanowire for three different biasing conditions during exposure to three humidity pulses

In [36], self-heated SnO<sub>2</sub> nanowire gas sensors with a power consumption of only few tens of  $\mu\text{W}$  were reported, which is almost two orders of magnitude lower than in the described ZnO nanowire devices. However, these substantial differences appear reasonable when considering the nanowire diameters (228 nm compared to 35 - 45 nm in [36]).

The self-heated ZnO nanowire device was operated at a maximum current density around  $3 \cdot 10^9 \text{ A/m}^2$ , which is consistent with the electrical characterization results on three other ZnO devices (diameters 88 - 130 nm) that could sustain maximum current densities between  $3 \cdot 10^9 \text{ A/m}^2$  and  $2 \cdot 10^{10} \text{ A/m}^2$ . These values are considerably higher compared to the critical current den-

sities of  $2 - 6 \cdot 10^7$  A/m<sup>2</sup> of single ZnO nanowires reported in [252]. However, it is known from literature that single-crystalline nanowires can carry such high current densities as other authors reported  $10^{10}$  A/m<sup>2</sup> for SnO<sub>2</sub> nanowires [253] or even  $3 \cdot 10^{12}$  A/m<sup>2</sup> for NiSi<sub>2</sub> nanowires [254]. As a consequence it can be concluded that the described ZnO nanowires show excellent material properties in terms of sustaining large current densities and are thus very promising candidates for the realization of self-heated nanowire gas sensor devices, which was demonstrated in first measurements.

## 7 Nanowire Array Devices

### 7.1 CuO Nanowire Arrays:

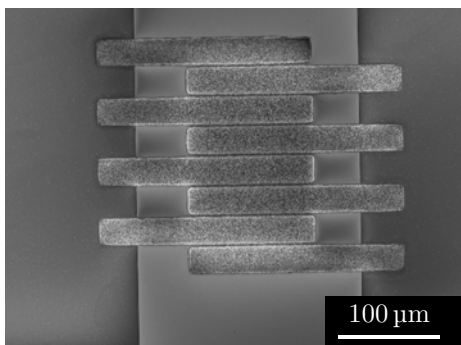
#### Thermal Oxidation of Electroplated Cu

Electroplated Cu structures were fabricated using the same process steps as described in Chapter 4.1.3. In order to realize gas sensing devices, the electroplated Cu structures were contacted by a sputtered Ti/Au layer (5 nm and 200 nm thickness, respectively), which was structured by a photolithographic lift-off process (Appendix A). These steps were performed on 4" wafer scale followed by dicing to 5×5 mm chips. After an Ar ion etching process (Roth & Rau IonSys 500, 2 min) for surface cleaning, the samples were oxidized in a furnace under a constant flow of pure oxygen at 400 °C for three hours.

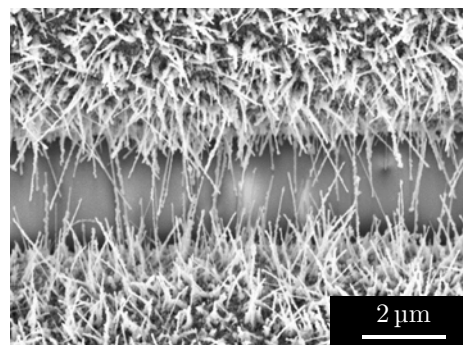
A typical device (see Fig.7.1a) employed eight parallel oxidized Cu lines (width 25 μm, gap distance 5 μm before thermal oxidation) with four of them connected in parallel by two separate Ti/Au contact pads. The thermal oxidation process lead to a reduction of the gap distance between adjacent Cu lines and CuO nanowire growth on the oxidized Cu structure, similar as described in Chapter 4.1.3. The gap was bridged by suspended CuO nanowires (see Fig.7.1b), which form an electrical connection between the oxidized Cu lines and thus between the two Ti/Au contact pads. As mentioned above, CuO nanowires synthesized with this specific technology typically showed dimensions with lengths in the range of few μm and diameters between 15 nm and 70 nm. Most commonly, polycrystalline CuO nanowires with crystallites at the surface were observed.

The IV characteristics of a typical CuO nanowire array device are presented in Fig.7.1c. Measurements were performed at room temperature in ambient atmosphere using a Suss Microtech probe station and an Agilent 4156C parameter analyzer. The nonlinear behavior indicates that potential barriers between CuO nanowires contacting each other or the adjacent oxidized Cu structure play an important role for the room temperature electrical device

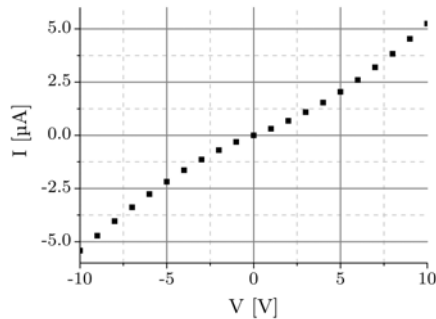
properties. The contribution of the CuO nanowire arrays to the overall resistance was estimated by means of test structures on the same substrate. Measurements revealed that the Ti/Au contact resistance to the oxidized Cu lines and the series resistance of the oxidized Cu lines were several orders of magnitude lower than the total resistance of a typical CuO nanowire array device. Therefore the electrical device resistance could be almost exclusively attributed to the bridging CuO nanowires between the oxidized Cu lines.



(a) Typical device design: eight oxidized Cu lines contacted by Ti/Au pads



(b) CuO nanowires bridging adjacent oxidized Cu lines



(c) Typical IV characteristics at room temperature in ambient atmosphere

Figure 7.1: CuO nanowire array devices (electroplated Cu)

Electrical measurements were also performed on devices with a different layout of the Cu lines (same dimensions, but arranged in four pairs of adjacent Cu structures). Due to similar IV characteristics the two device designs were considered to be well comparable in terms of gas sensing properties.

Conductometric gas sensors were realized according to methods described in Chapter 5.1 and gas measurements were performed at different operation temperatures at a constant total gas flow of 1000 sccm. As the predominant part of the overall sensor resistance was attributed to the suspended CuO nanowires, the latter constitute the gas sensitive part of the CuO nanowire array devices. In principle, gas-induced resistance changes can be expected from modulation of carrier concentrations in the nanowire channels and of the potential barriers at grain boundaries.

Electrical resistance changes of CuO nanowire array devices during exposure to humidity and CO are shown in Fig.7.2a and Fig.7.2b. First of all, it has to be noted that the device resistance decreased between one and two orders of magnitude at the elevated sensor operation temperatures (300-350 °C) compared to room temperature. This finding can be explained by CuO material properties, changes in coverage with chemisorbed oxygen ions and enhanced thermal excitation across grain-grain potential barriers. In the presence of water vapor and small concentrations of CO (10-300 ppm), the CuO nanowire array resistance increased in both cases, which is consistent with the results on single CuO nanowire devices presented in the last Chapter. It can be assumed that the sensing mechanism is again governed by reactions of ionosorbed oxygen species with H<sub>2</sub>O and CO, respectively. Considering the reactions in Eq.6.I and Eq.6.II, the increased CuO nanowire device resistance may be explained by a decrease of hole concentration in the CuO surface accumulation layer.

In addition, the H<sub>2</sub>S sensing properties of the CuO nanowire array devices were investigated. In Fig.7.2c, a measurement during exposure to increasing ppb-level concentrations of H<sub>2</sub>S at an operation temperature of 150 °C is shown. An initial sensor resistance increase is followed by a steep resistance decrease of the CuO nanowire array device. The ratio of sensor resistance after and before H<sub>2</sub>S exposure was found to be as low as  $6.5 \cdot 10^{-4}$ . After exposure to dry synthetic air (not shown in the graph) the CuO nanowire array device did not recover its initial resistance value.

At an operation temperature of 325 °C, a different sensor behavior was found. During exposure to ppb-level H<sub>2</sub>S pulses reversible sensor signals were observed depending on the different concentrations from 10-500 ppb, as can be seen in Fig.7.2d. The sensor response, defined as ratio  $R_{H_2S} / R_{air}$ , ranged from 1.07 to 2.05 demonstrating the excellent sensor performance for H<sub>2</sub>S detection in the ppb-level range.

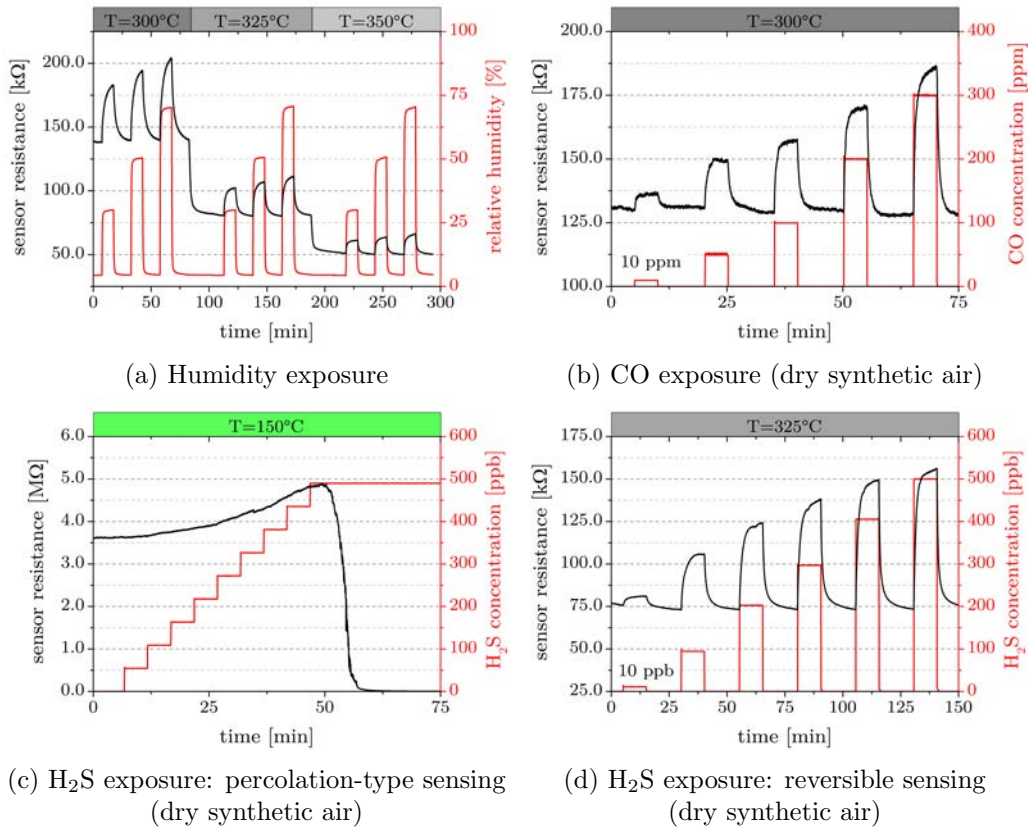
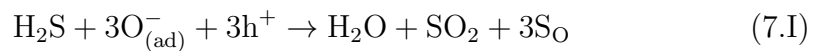
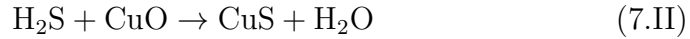


Figure 7.2: Gas measurements on CuO nanowire array devices (electroplated Cu)

The distinct sensor behavior for the two sensor operation temperatures may be explained by different chemical reactions at the CuO surface. On the one hand, it was proposed that H<sub>2</sub>S molecules react with ionosorbed oxygen species according to [255]:



On the other hand, it is known that CuO may be converted to CuS during H<sub>2</sub>S exposure, whereas reaction of CuS with O<sub>2</sub> results in the re-oxidation to CuO. The corresponding chemical equations were suggested as follows [54, 256]:



In case of the sensor operation temperature of 150 °C, the initial resistance increase may be explained by the reaction of H<sub>2</sub>S with ionosorbed oxygen (Eq.7.I). After prolonged H<sub>2</sub>S exposure the formation of CuS according to Eq.7.II was reported to result in a steep resistance decrease due to percolating CuS pathways with metallic behavior [256]. It is expected that the elevated operation temperature of 325 °C leads to increased CuO surface coverage with ionosorbed oxygen ions and to enhanced rates of CuS re-oxidation (Eq.7.III). Both these factors are assumed to contribute to the observed reversible H<sub>2</sub>S sensing characteristics.

## 7.2 CuO Nanowire Arrays: Thermal Oxidation of Evaporated Cu

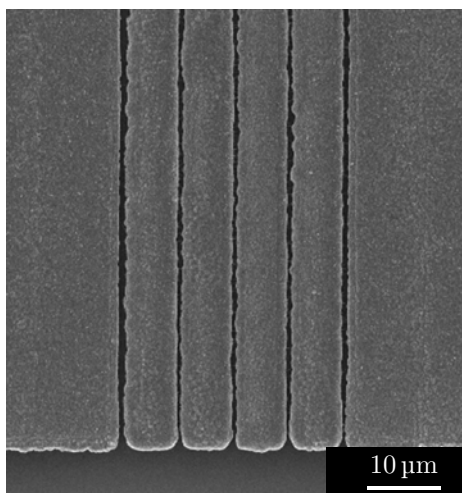
Based on the results in Chapter 4.1.4, specific Cu structures were designed, which enable the direct integration of CuO nanowires into a resistive device, similar as in the previous Chapter. The fabrication of CuO nanowire gas sensors by thermal oxidation of evaporated Cu structures comprised the following steps: First, a photolithographic lift-off process (Appendix A) was performed on 2×2 cm Si substrates with 300 nm of thermal SiO<sub>2</sub> in order to structure a thermally evaporated Ti/Au layer (thickness 5 nm and 200 nm, respectively). As a result, quadratic contact pads with an edge length of 150 μm were realized. Afterwards, specifically designed Cu microstructures were fabricated by a second photolithographic lift-off step of a Ti/Cu layer (thickness 5 nm and 500 nm, respectively). Finally, CuO nanowires were syn-



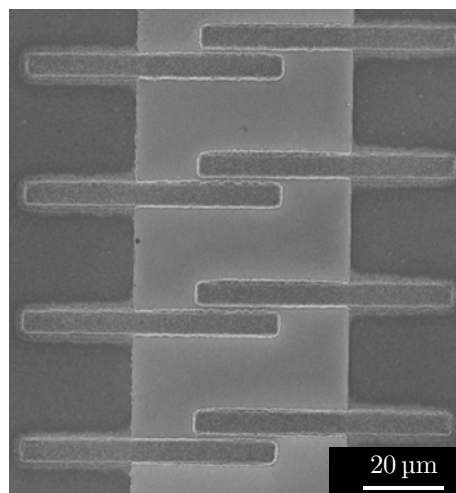
thesized by thermal oxidation of the Cu structures at 350 °C for three hours on a hotplate in ambient atmosphere. As the same Ti/Cu layer and the same thermal oxidation parameters were used as described in Chapter 4.1.4, very similar results for CuO nanowire synthesis were achieved. The thermal oxidation process again resulted in the growth of CuO nanowires with very small diameters between 10 nm and 30 nm and presumably single crystalline or bi-crystalline structure.

The CuO nanowire array devices relied on different designs of Cu lines, as can be seen in Fig.7.3a and Fig.7.3b. The distance between adjacent Cu microstructures was carefully chosen as their dimensions increased considerably during the thermal oxidation process, similar as for electroplated Cu structures (Chapter 4.1.3). A Cu line width of 5  $\mu\text{m}$  and a gap distance of 2  $\mu\text{m}$  in between was chosen resulting in bridging CuO nanowires (Fig.7.3c), which formed an electrical connection between adjacent oxidized Cu structures. Thus each gap consists of a multitude of suspended CuO nanowires in parallel. The device in Fig.7.3a can be considered as series circuit of five CuO nanowire arrays, whereas the device in Fig.7.3a is a parallel circuit of four CuO nanowire arrays.

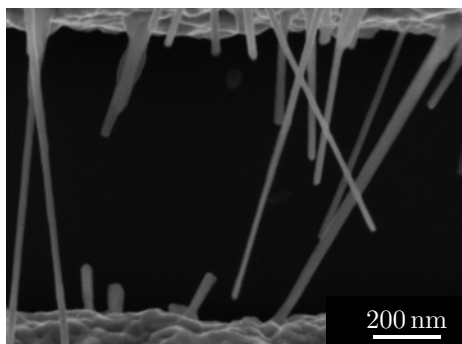
The IV characteristics were characterized at room temperature in ambient atmosphere using a Süss Microtech probe station and an Agilent 4156C parameter analyzer. Typical results are shown in Fig.7.3d for both a series circuit type as well as a parallel circuit type device. It has to be noted that the two device designs do not only differ in equivalent circuit, but also in lengths of opposing oxidized Cu lines and thus number of employed CuO nanowires. However, in general no qualitative differences between the IV characteristics of the two types of devices were found. Nonlinear behavior was observed similar as for the CuO nanowire array devices presented in the last Chapter, which again indicates the presence of potential barriers. Measurements on several test structures were performed, which also confirmed in this case that the CuO nanowire arrays contributed to a large part of the overall device resistance.



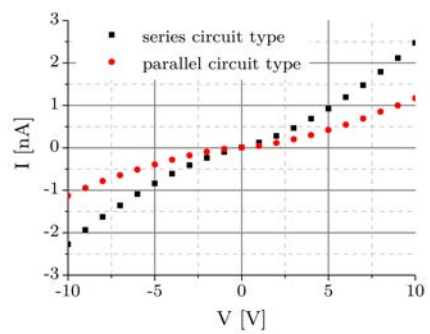
(a) Series circuit type device



(b) Parallel circuit type device



(c) CuO nanowires bridging adjacent oxidized Cu lines



(d) Typical IV characteristics at room temperature in ambient atmosphere

Figure 7.3: CuO nanowire array devices (evaporated Cu)

The gas sensing properties of these CuO nanowire array devices were characterized in a similar way as in Chapter 7.1 and measurements are shown in Fig.7.4. The resistance changes during humidity, CO and H<sub>2</sub>S exposure are qualitatively well comparable to the results presented before. The sensing mechanism is attributed to reactions with ionosorbed oxygen species according to Eqs.6.I, 6.II and 7.I.

In particular, the CuO nanowire array device realized by thermal oxidation of evaporated Cu structures showed extraordinary sensor performance for H<sub>2</sub>S detection as the largest sensor signals were observed in this case. A detailed comparative study using different types of sensor devices, which were exposed to H<sub>2</sub>S in dry and humid atmosphere, will be discussed in the next Chapter. In addition, very low H<sub>2</sub>S concentrations from 1-10 ppb could be detected in repeated measurements on three CuO nanowire array sensors (see Fig.7.4d for a representative measurement). It can be expected that the H<sub>2</sub>S detection limit of the presented sensor technology lies in the ppt range but cannot be evaluated with the current experimental setup.

In Table 7.1, the H<sub>2</sub>S sensing results achieved in this work are compared to literature reports on conductometric gas sensors. As can be seen, the presented CuO nanowire array devices are among the most sensitive chemiresistive H<sub>2</sub>S sensors, especially in comparison with results based on CuO.

<i>Material</i>	<i>Detection limit</i> [ppb]	<i>Ref.</i>
Au decorated SWCNT	3	[257]
CuO nanowires	2.5 (calculated)	[55]
CuO nanosheet	2 (calculated)	[255]
CuO doped BSST	1	[258]
Au decorated polyaniline nanowires	0.1	[259]
CuO nanowire array	<1	this work

Table 7.1: H<sub>2</sub>S detection: comparison of CuO nanowire array with literature results

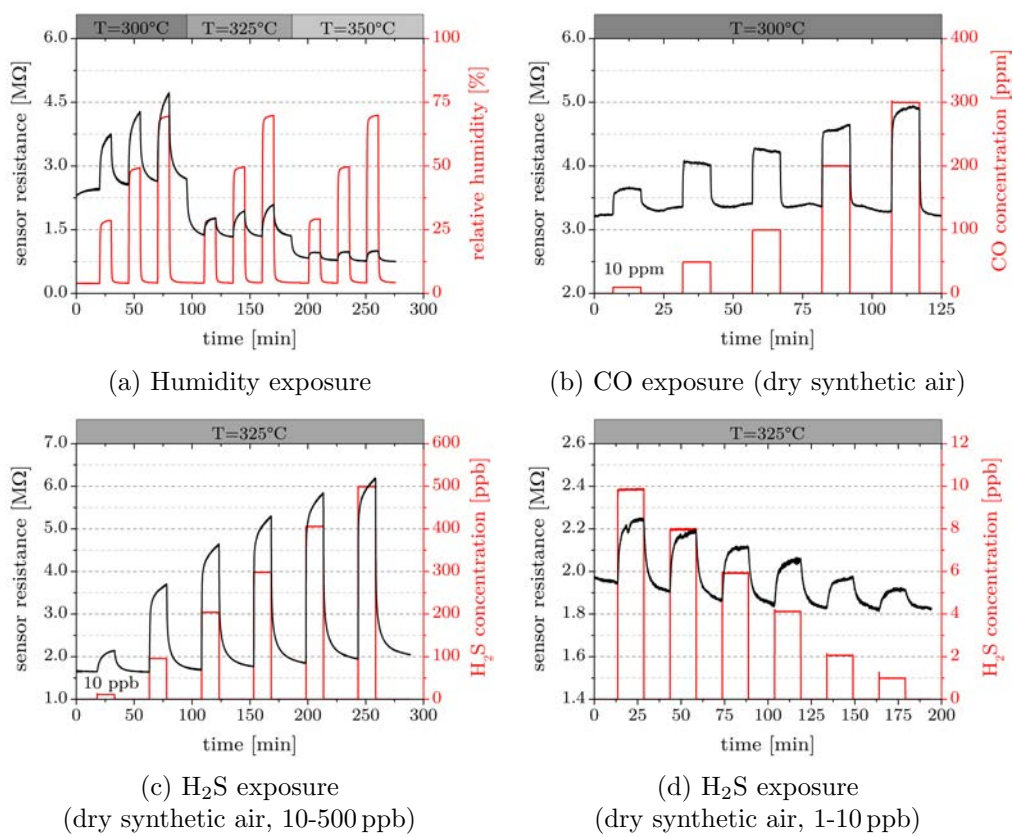


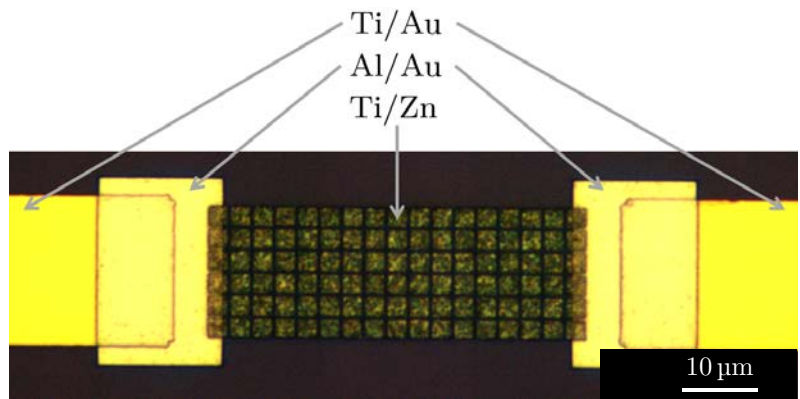
Figure 7.4: Gas measurements on CuO nanowire array devices (evaporated Cu)

### 7.3 ZnO Nanowire Arrays: Thermal Oxidation of Evaporated Zn

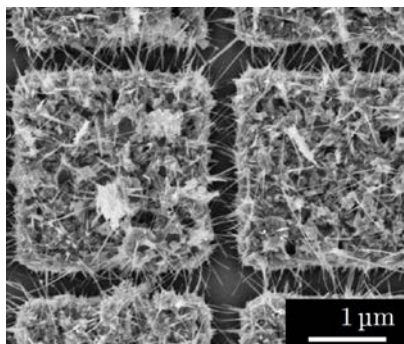
ZnO nanowire array devices were realized as follows: In a first step, contact pads and electron beam alignment markers were fabricated by a photolithographic lift-off process (Appendix A) of a thermally evaporated Ti/Au layer (thickness 5nm and 200nm, respectively). Quadratic 2×2cm Si chips covered with 300 nm of thermal SiO<sub>2</sub> were used as substrates. Next, electron beam lithography was performed using a PMMA lift-off process (Appendix A) and a writefield size of 100×100 μm. After thermal evaporation regular arrays of Zn squares (edge length 2.5 μm, gap distance ~500 nm, thickness ~250 nm) were realized as already described earlier in Chapter 4.2.3. Subsequently, a second electron beam lithography step was used for the fabrication of Al/Au structures (thickness 150 nm and 100 nm, respectively), which were deposited by thermal evaporation after 30 s of oxygen plasma treatment for improved electrical contact properties. As can be seen in Fig.7.5a, the Al/Au structures formed the electrical contacts between the outer elements of the regular Zn square array and the Ti/Au pads. For ZnO nanowire synthesis, the substrates were thermally oxidized at a temperature of 410 °C for 1 h on a hotplate in ambient atmosphere. A typical example of ZnO nanowires bridging adjacent oxidized Zn squares is shown in Fig.7.5b. As mentioned above, ZnO nanowires synthesized by this specific technology most commonly have diameters ranging from 10-30 nm and lengths below 1-2 μm. Several samples were afterwards functionalized by a thin Au layer with a thickness of around 2 nm. The deposition was performed by thermal evaporation and was controlled by a quartz crystal microbalance. The functionalized samples were annealed at temperatures around 400 °C resulting in Au nanoparticle formation, which can be seen in a SEM image in Fig.7.5c.

A Sues Microtech probe station and an Agilent 4156C parameter analyzer were used for electrical characterization of the ZnO nanowire array and the ZnO/Au nanowire array devices at room temperature in ambient atmosphere. Linear IV characteristics were observed in the large majority of measure-

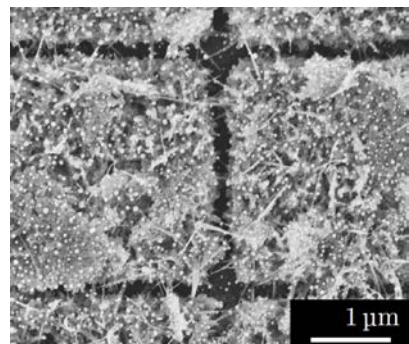
ments. It is assumed that the overall electrical device resistance was mainly dominated by the thermally oxidized Zn structures and the ZnO nanowires bridging the gaps in between. In Fig.7.5d, the IV characteristics of a ZnO nanowire array before and after Au evaporation are compared. As is obvious, no short circuit was formed, but device resistance was increased after metal deposition. It is expected that Au functionalization has two effects on ZnO conductivity, as was proposed in [13]. The ZnO nanowires are presumably depleted from electrons due to nanoscale Schottky junctions at the surface and due to catalytic dissociation of O<sub>2</sub> molecules and thus enhanced electron trapping at chemisorbed oxygen ions.



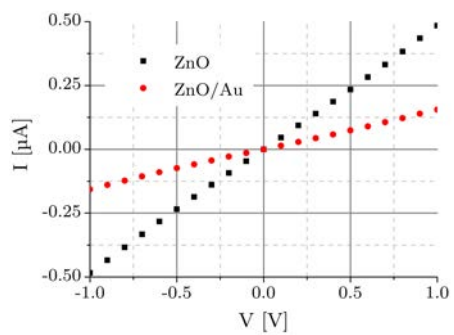
(a) Device design of ZnO nanowire array devices



(b) ZnO nanowires bridging adjacent oxidized structures



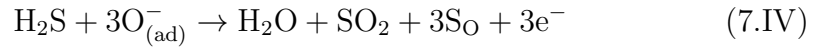
(c) ZnO/Au nanowires bridging adjacent oxidized structures



(d) IV characteristics at room temperature in ambient atmosphere

Figure 7.5: ZnO nanowire and ZnO/Au nanowire array devices

Conductometric gas sensors were realized and characterized as described in Chapter 5.1. Fig.7.6 shows a typical resistance change of a ZnO nanowire array device during H<sub>2</sub>S exposure at an operation temperature of 300 °C using humid synthetic air as background gas (50% relative humidity). Considerable sensor signals up to around a factor of two could be achieved during exposure to H<sub>2</sub>S concentrations from 250-750 ppb validating the notable sensor performance. The sensing mechanism is expected to be based on surface reactions with ionosorbed oxygen species as suggested in [260]:



The reaction of H<sub>2</sub>S with oxygen ions leads to the release of electrons into the semiconducting metal oxide material. When considering the ionosorption model this leads to a decreased width of the ZnO surface depletion layer and thus a decrease of resistivity, which is in accordance with the presented gas measurement results. However, S diffusion into ZnO nanostructures leading to the formation of an additional donor level was proposed for elevated operation temperatures above 300 °C [261]. Thus this potential coexistent mechanism cannot be excluded for the presented measurement results. Supplemental gas measurements accompanied with spectroscopic characterization techniques are proposed for further clarification.

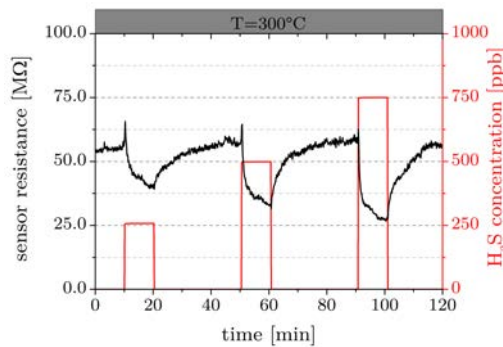
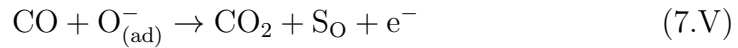


Figure 7.6: H<sub>2</sub>S sensing with ZnO nanowire array device (50% relative humidity)



As is known from literature, Au nanoparticle decoration may lead to improved performance of ZnO nanowire gas sensors regarding CO detection [262]. Thus the gas sensing properties of the ZnO/Au nanowire array devices were especially evaluated during CO exposure in dry and humid atmosphere. Measurements were performed at an operation temperature of 350 °C in dry synthetic air as well as at 50% relative humidity and results are shown in Fig.7.7a and Fig.7.7b, respectively. In both cases CO concentrations from 10-100 ppm could be clearly detected. Increased gas response was observed in the case of dry synthetic air and the detection of 1 ppm CO was possible.

The presented measurements of the ZnO/Au nanowire array devices are well comparable to CO sensing results reported in [263]. Decreased sensor resistance was attributed to electron release during CO reaction with chemisorbed oxygen ions and the reaction was suggested as follows:



It can be expected that competing surface reactions are responsible for the differences in sensor performance between dry and humid synthetic air. Additional experiments on ZnO nanowire array and ZnO/Au nanowire array devices are suggested for the future in order to further explore humidity interference effects, which will be more thoroughly studied in the following using different types of CuO nanowire sensors.

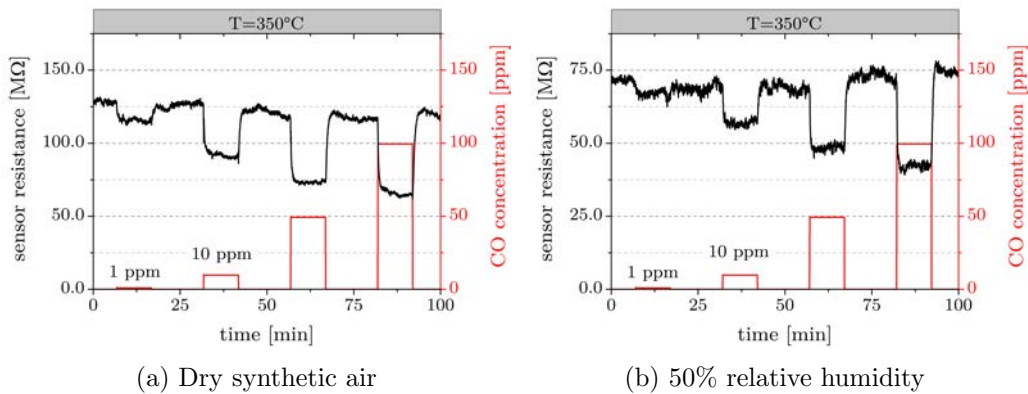


Figure 7.7: CO sensing with ZnO/Au nanowire array device

## 8 CuO Nanowire Gas Sensors: Humidity Interference

As water vapor is present in ambient atmosphere, humidity interference effects on the gas sensor performance have to be thoroughly studied regarding practical applications. In literature, few experimental data on the influence of humidity on the performance of CuO based gas sensors can be found. In the following, the CO and H<sub>2</sub>S response in dry and humid synthetic air of several different realizations of CuO nanowire gas sensors will be studied.

### 8.1 CO Sensing in Dry and Humid Atmosphere

The CO response of single CuO nanowires in a four point configuration (Chapter 6.1.2) was studied at an operation temperature of 350 °C in dry synthetic air and at 50% relative humidity. Decreased CO response in the presence of water vapor was observed, which is in accordance with literature results on CuO thick film sensors [78]. When considering the surface reactions Eq.6.I and Eq.6.II, competition between H<sub>2</sub>O and CO molecules for CO reaction partners can be assumed. However, reduced CO sensitivity of the single CuO nanowire devices was observed in repeated experiments and attributed to carbon poisoning of the CuO surface (see Chapter 6.1.4). As a consequence, no extended systematic studies could be performed.

Furthermore, humidity interference effects during CO exposure was studied using CuO nanowire array devices realized by thermal oxidation of evaporated Cu structures (Chapter 7.2). In this case measurements were performed at a constant operation temperature of 350 °C using the following procedure: the CuO nanowire sensor was first exposed to ten repeated pulses of CO (concentration 100 ppm) in dry synthetic air followed by ten pulses in humid synthetic air (50% relative humidity) and then ten pulses in dry synthetic air again. The sensor response was evaluated according to  $R_{CO}/R_{air}$  and the results are shown in Fig.8.1.

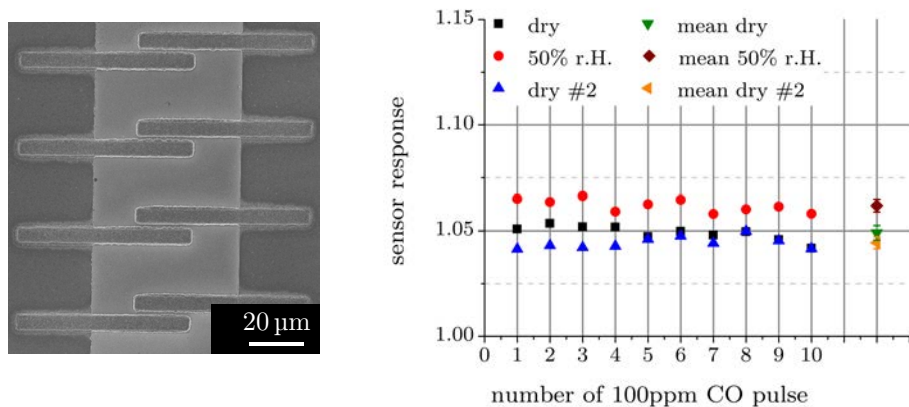


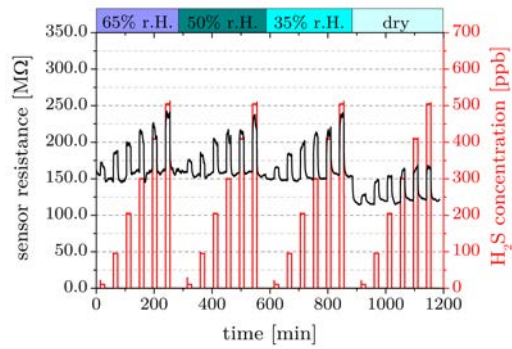
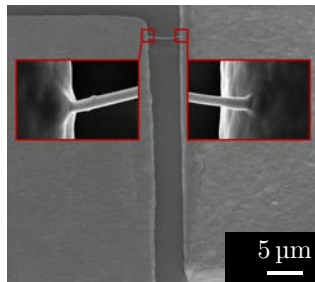
Figure 8.1: Evaluation of CO sensor response in dry and humid atmosphere (sensor operation temperature 350 °C)

First of all, no significant sensor poisoning was observed during the total measurement time of 23 hours. Thus the CuO nanowire array device showed superior long term stability of the CO response compared to the single CuO nanowire devices in a four point configuration. These results may be potentially explained by varying surface properties of CuO nanowires synthesized by different growth techniques.

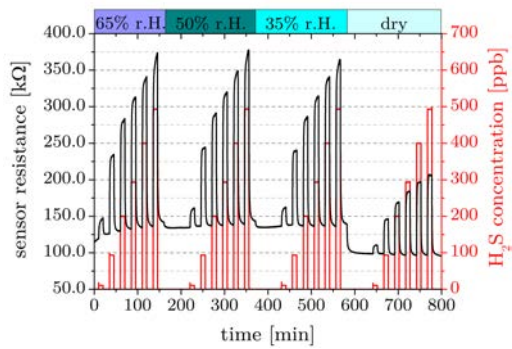
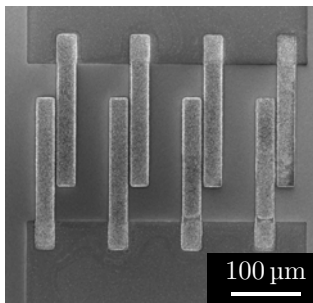
As can be seen in Fig.8.1, the CO response of the CuO nanowire array devices was only slightly influenced by the presence of water vapor molecules, which is highly beneficial regarding a practical sensor application. Most interestingly, the CO response was slightly increased in humid atmosphere, which is in contrast to [78] where the opposite behavior was observed for CuO thick film sensors at an operation temperature of 150 °C. Apart from varying CuO surface properties two main reasons are assumed to be responsible for the differing results: Firstly, the comparatively high operation temperature of 350 °C is expected to lead to fast kinetics of the chemical reactions at the CuO nanowire surfaces. Secondly, gas species can be readily adsorbed at/desorbed from the sensor surface due to the specific sensor configuration employing suspended CuO nanowires. Both these factors should lead to high adsorption/desorption rates and thus reduced competition between CO and H<sub>2</sub>O molecules for O<sup>-</sup> reaction partners.

## 8.2 H<sub>2</sub>S Sensing in Dry and Humid Atmosphere

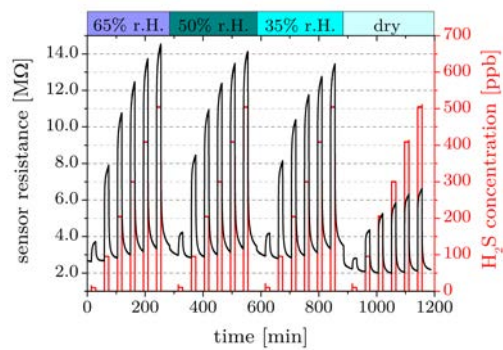
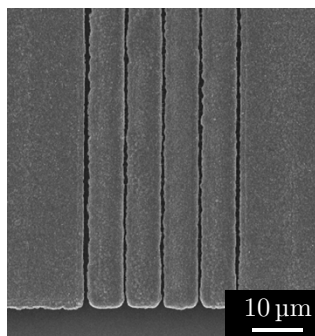
Humidity interference effects during H<sub>2</sub>S exposure were studied by comparing three different types of CuO nanowire gas sensors, i.e. the single suspended CuO nanowire (Chapter 6.1.3), a CuO nanowire array device fabricated by thermal oxidation of electroplated Cu (Chapter 7.1; in the following termed interdigitated CuO nanowire sensor) and a CuO nanowire array device fabricated by thermal oxidation of evaporated Cu (Chapter 7.2; in the following termed bridge-to-bridge CuO nanowire sensor). The sensors were operated at a constant temperature of 325 °C and were exposed to different concentrations of H<sub>2</sub>S (10-500 ppb) in dry as well as humid (35%, 50% and 65% relative humidity) synthetic air. Measurement results are presented in Fig.8.2. As can be seen, all the three investigated CuO nanowire gas sensors were capable of detecting low H<sub>2</sub>S concentrations ranging from 10 ppb to 500 ppb. In general both CuO nanowire array devices exhibited more stable sensor signals compared to the single suspended CuO nanowire in dry as well as humid atmosphere. It is assumed that this advantage of the multiple CuO nanowire devices results from the fact that the device resistance depends on a large number of CuO nanowires.



(a) Single suspended CuO nanowire



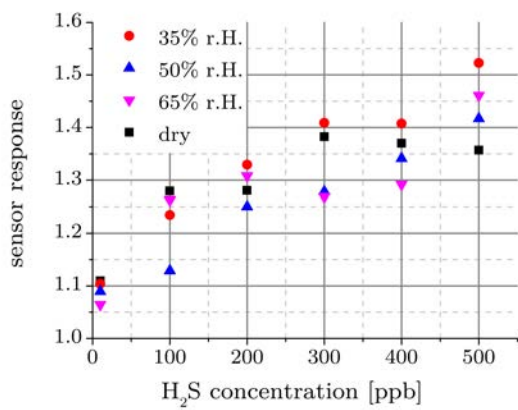
(b) Interdigitated CuO nanowire sensor



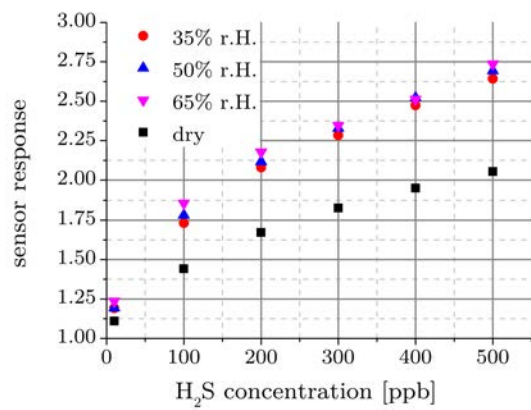
(c) Bridge-to-bridge CuO nanowire sensor

Figure 8.2: ppb-level  $H_2S$  sensing in dry and humid atmosphere (sensor operation temperature  $325^\circ C$ )

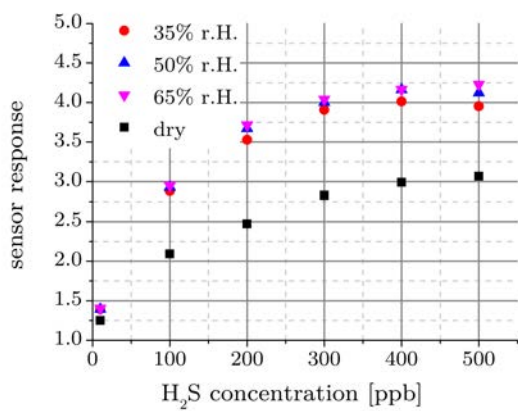
The sensor performance of the three CuO nanowire devices was quantified and compared by calculating the sensor response according to  $R_{H_2S}/R_{air}$ . Results for the single suspended CuO nanowire are presented in Fig.8.3a for different relative humidity levels. In this case, resistance drifts were considered by calculating the sensor resistance mean value of 300 data points (corresponding to approximately 5 minutes) before each H<sub>2</sub>S pulse and at the end of each H<sub>2</sub>S pulse. No distinct increase or decrease in H<sub>2</sub>S response was observed when comparing the results for dry and humid synthetic air. For the case of the interdigitated CuO nanowire sensor and the bridge-to-bridge CuO nanowire sensor, the H<sub>2</sub>S response for different relative humidity levels is shown in Fig.8.3b and Fig.8.3c, respectively. Both CuO nanowire array devices exhibited significantly enhanced H<sub>2</sub>S response in humid synthetic air, rather independent of relative humidity level. Results at 50% relative humidity are compared for all three CuO nanowire sensors in Fig.8.3d. The bridge-to-bridge CuO nanowire sensor, which employed CuO nanowires with the smallest diameters, clearly showed the highest H<sub>2</sub>S response in the investigated concentration range.



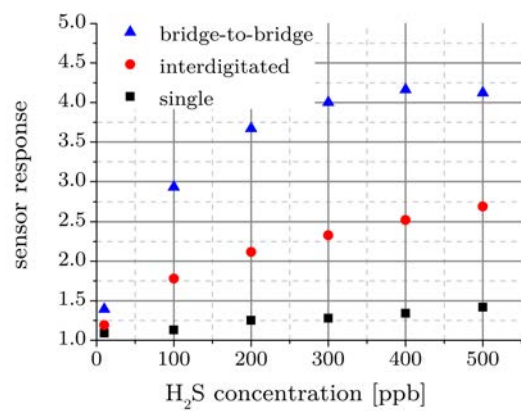
(a) Single suspended CuO nanowire



(b) Interdigitated CuO nanowire sensor



(c) Bridge-to-bridge CuO nanowire sensor



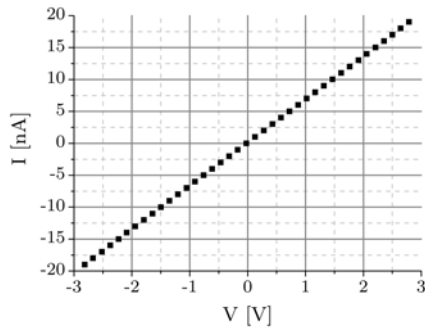
(d) Sensor comparison (50% relative humidity)

Figure 8.3: Evaluation of H<sub>2</sub>S sensor response in dry and humid atmosphere (sensor operation temperature 325 °C)

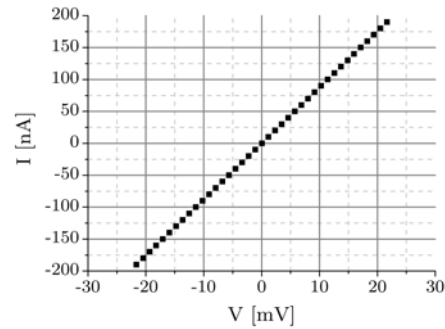
The device designs of the three investigated CuO nanowire gas sensors obviously showed significant differences, which has to be considered for proper interpretation of the measurement results. The IV characteristics were measured in ambient atmosphere at the sensor operation temperature of 325 °C for all three CuO nanowire sensors (see Fig.8.4). Due to the Ohmic behavior it is assumed that the CuO nanowire channels dominated the sensor resistance rather than potential barriers between CuO nanowires contacting each other or the adjacent oxidized Cu structure. Consequently, it is expected that the same transduction mechanism of the H<sub>2</sub>S reaction was dominant in all three investigated devices. However, the results on the interdigitated CuO nanowire gas sensor and the bridge-to-bridge CuO nanowire gas sensor cannot be directly compared with literature reports on CuO nanowire arrays, which were mechanically contacted after synthesis [54]. In that case, nonlinear IV characteristics were found and the H<sub>2</sub>S response was attributed to potential barrier modulation between touching CuO nanowires.

Gas molecule impingement rates on the CuO nanowire surfaces were estimated using similar assumptions as in [150]. It can be expected that the conductivities of the multiple CuO nanowire channels were modulated homogeneously across the whole sensor area due to the high number of H<sub>2</sub>S molecules impinging on the CuO nanowire surfaces. Consequently the differences in equivalent circuit model of the interdigitated CuO nanowire sensor (parallel circuit of CuO nanowire arrays) and the bridge-to-bridge CuO nanowire sensor (series circuit of CuO nanowire arrays) should have no influence on the gas sensing mechanism.

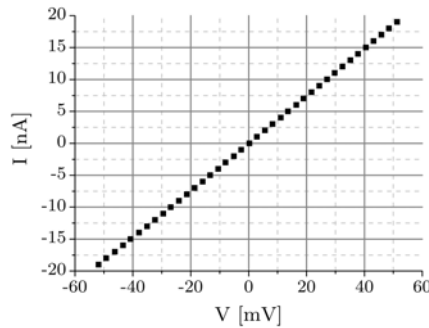




(a) Single suspended CuO nanowire



(b) Interdigitated CuO nanowire sensor



(c) Bridge-to-bridge CuO nanowire sensor

Figure 8.4: IV characteristics of the three CuO nanowire sensors at  $T=325\text{ }^{\circ}\text{C}$

Therefore the differences in  $\text{H}_2\text{S}$  sensing properties of the three investigated devices is attributed to the diameter of the employed CuO nanowire sensing elements. It can be assumed that the diameter of the single suspended CuO nanowire (170 nm) considerably exceeds the Debye length for CuO, which was estimated to lie between 3 nm and 23 nm [78]. In this case, the CuO nanowire resistance consists of a bulk contribution and a surface accumulation layer contribution with the latter being influenced by the surrounding gas atmosphere. Thus the  $\text{H}_2\text{S}$  response is exclusively attributed to a modulation of the carrier concentration in the accumulation layer at the CuO nanowire surface.

Due to the large diameter of the single suspended CuO nanowire of 170 nm, a lower gas response is observed compared to both multiple CuO nanowire sensors, which employ nanowires with much smaller diameters. In literature [84],

single SnO<sub>2</sub> nanowires with diameters from 41-117 nm were compared. Differences in gas response up to a factor of 2 were found, which is in qualitative agreement with the results presented here.

In literature, the interaction of CuO surfaces with H<sub>2</sub>O and H<sub>2</sub>S was explained in both cases by reactions with chemisorbed O<sup>-</sup> species (see Eq.6.I and Eq.7.I). Thus a decreased H<sub>2</sub>S response is intuitively expected in the presence of water vapor molecules due to a competition for reaction partners. However, increased H<sub>2</sub>S response in humid synthetic air was clearly observed for both CuO nanowire array devices. In order to explain the measurement results, the following model is proposed: It is assumed that the bulk carrier concentration in the CuO nanowires is influenced by humidity, similar as was reasoned in [264] for SnO<sub>2</sub> gas sensors. In the case of the p-type semiconductor CuO, the initial density of bulk free holes  $N_h$  is modified to a reduced density of free holes  $N_{h,rH}$ . As the Debye length is inversely proportional to the square root of the free hole density (Eq.2.I), it is increased in the presence of humidity due to chemisorption of water vapor molecules. If the surface space charge layer does not extend into the whole nanowire, the conductance consists of a bulk and a surface contribution. In this case, a humidity induced Debye length increase would lead to a more efficient modulation of the CuO nanowire gas sensor resistance by H<sub>2</sub>S.

The single suspended CuO nanowire showed no distinct increase or decrease of H<sub>2</sub>S response in dry or humid atmosphere. It is expected that the modulation of the Debye length by humidity is not observed in this case as this effect should be small compared to the large nanowire diameter (170 nm). However, for the interdigitated CuO nanowire sensor (nanowire diameter 15-70 nm) and the bridge-to-bridge CuO nanowire sensor (nanowire diameter 10-30 nm) it can be assumed that the proposed humidity induced Debye length increase is comparable to the nanowire diameters and is therefore observed in the electrical resistance measurements.

Due to the large number of water vapor molecules in humid synthetic air, the CuO nanowire surfaces were almost saturated for all relative humidity

levels. Therefore, only a minor influence on the free hole density  $N_{h,rH}$  is expected leading to small differences in the H<sub>2</sub>S response for the different relative humidity levels. Moreover, the ratio of the H<sub>2</sub>S responses  $S_{humid}/S_{air}$  is larger for the bridge-to-bridge CuO nanowire sensor. This indicates that the increase of H<sub>2</sub>S response in humid synthetic air depends on the nanowire diameter, which would support the discussed H<sub>2</sub>S sensing model.

# 9 CuO Nanowire Integration on CMOS Microhotplates

## 9.1 CMOS Microhotplates: General Description

Within the CATRENE COCOA project, CMOS microhotplates were designed and fabricated in a collaborative work of AIT Austrian Institute of Technology, ams AG and the Department of Micro- and Nanosystems at the University of Applied Sciences Wiener Neustadt. Detailed characterization and performance results of the developed CMOS microhotplates can be found in [265].

In principle the presented microhotplate devices were based on a polysilicon heating resistor in a standard CMOS layer stack (see Fig.9.1a). Thermal conduction through the bulk Si had to be minimized by Si removal beneath the dielectric layers in order to achieve low power consumption heating to elevated temperatures up to 400 °C. The simplest microhotplate design, i.e. a suspended membrane, is schematically depicted in Fig.9.1b for a better understanding of the general working principle. However, more sophisticated MEMS devices were realized in order to achieve improved heating efficiency and homogeneous temperature distribution.

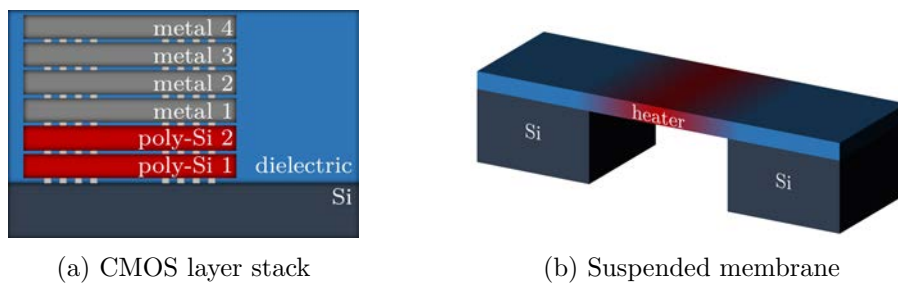
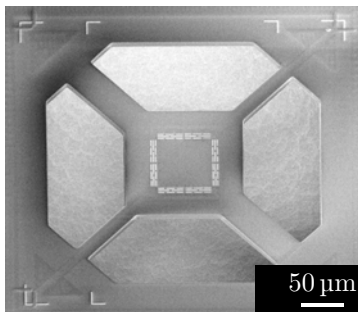


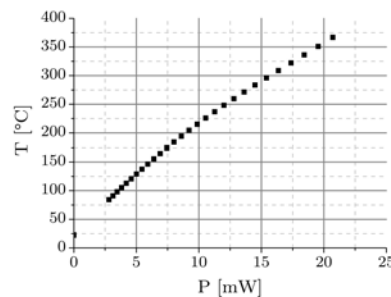
Figure 9.1: CMOS microhotplate schematics

Standard 0.35  $\mu\text{m}$  CMOS technology was used for the fabrication of the microhotplate devices used in this thesis. The design was based on a suspended microbridge supported by four arms, which is shown in Fig.9.2a. Metal contacts protruding out of the passivated surface were realized by few additional process steps, which were all performed in a CMOS environment on wafer-scale. The cavity was fabricated by a front side etching step of the dielectric layers and an isotropic  $\text{XeF}_2$ -based Si dry etching process.

Specifically designed polysilicon heaters were used in order to ensure a homogeneous temperature distribution all over the suspended microbridge. Due to minimized thermal conduction through the four suspension arms the surroundings of the microhotplate remained at ambient temperature, which was confirmed by thermographic measurements [265]. The local microhotplate temperature could be measured by means of integrated thermistor or thermocouple sensors. Fig.9.2b shows a typical temperature versus power consumption curve of a CMOS microhotplate device. For a heating power of only approximately 20 mW a local temperature around 350  $^\circ\text{C}$  was achieved.



(a) Microhotplate device (30°tilted)



(b) Temperature versus power consumption

Figure 9.2: CMOS microhotplate and its device performance

## 9.2 CuO Nanowire Synthesis by Local Microhotplate Heating

Integrated gas sensor devices were achieved by using a similar technology as for CuO nanowire array devices (Chapter 7.2). However, the process technology had to be adapted in order to account for particularities of the CMOS substrate and because of process flow restrictions. In the following, the required steps are described and results on the synthesis of CuO nanowires by local heating on CMOS microhotplates are presented.

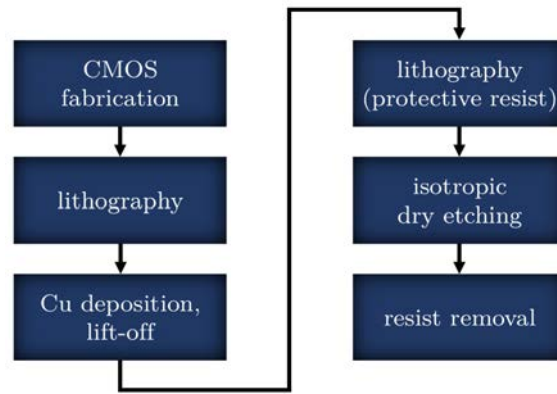


Figure 9.3: Device fabrication process flow

A schematic diagram of the device fabrication process flow is shown in Fig.9.3. After CMOS fabrication the wafer was diced to samples with a size of around  $2 \times 2$  cm. Next, electron beam lithography and lift-off was used for structuring of a thermally evaporated Ti/Cu layer (thickness 5 nm and 500 nm, respectively). Furthermore, a protective resist was applied and patterned in a second electron beam lithography process. Subsequently, an isotropic XeF<sub>2</sub>-based Si dry etching process was performed for under-etching of the suspended microbridge. Fig.9.4a shows the final CMOS microhotplate supported by four arms after removal of the protective resist. Eight Cu lines (width 5  $\mu$ m, gap distance 2  $\mu$ m) contacted the metal layer underneath in a specific configuration and thus could be interfaced by standard CMOS bond pads on the sample chip.

Local heating of the CMOS microhotplates was used for thermal oxidation of the Cu lines resulting in the growth of CuO nanowires. A constant current of 4.5 mA was applied to the polysilicon heater resulting in a power dissipation of 19.7 mW, which corresponds to a temperature around  $\sim 350^\circ\text{C}$ . After the thermal oxidation process was performed for one hour in ambient atmosphere, CuO nanowires were observed on the oxidized Cu surfaces (see Fig.9.4b).

The CuO nanowire synthesis results achieved by local heating on CMOS microhotplates are well comparable to those presented in Chapter 4.1.4, where heating of the whole Si substrate was used for the thermal oxidation process. Similar CuO nanowire dimensions (diameters 10-30 nm) and areal density were observed. As can be seen in Fig.9.4b, CuO nanowires bridged the gap between adjacent oxidized Cu structures and thus form an electrical connection, similar as described in Chapter 7.2. As a result, CuO nanowires were successfully integrated as components of resistive devices on CMOS microhotplates.

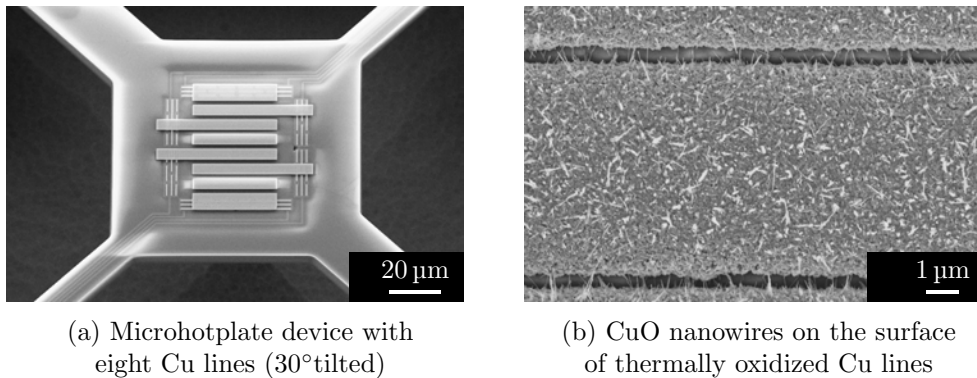


Figure 9.4: Integration of CuO nanowire arrays on CMOS microhotplates

### 9.3 Gas Sensing Results

From the device design (see Fig.9.4a) it can be seen that the electrical resistance could be measured between several different contact electrodes. In the following, gas sensing results are shown for the case of two CuO nanowire arrays in series contributing to the overall sensor resistance. The polysilicon heater was biased with a constant current of 4.35 mA, which corresponded to a power consumption of 18.2 mW and a microhotplate temperature around 325 °C. Electrical resistance changes of the CuO nanowire gas sensor during exposure to three pulses of humidity are shown in Fig.9.5a. Increasing CuO nanowire array resistance in the presence of water vapor with large sensor responses up to a factor of two were observed. The gas sensing properties of the CMOS integrated CuO nanowire device was also investigated during exposure to three CO pulses with concentrations between 10 ppm and 100 ppm (Fig.9.5b). The measurement demonstrated that the presented gas sensor was able to detect CO in the investigated concentration range with sensor responses up to around 17%. These findings are well comparable with results on similar CuO nanowire array devices on Si substrates assembled with external heating elements (Chapter 7.2). The increased sensor resistance in the presence of water vapor and CO was again attributed to reactions with ionosorbed oxygen species (Eq.6.I and Eq.6.II, respectively) leading to a decrease of charge carriers in the CuO surface accumulation layer.

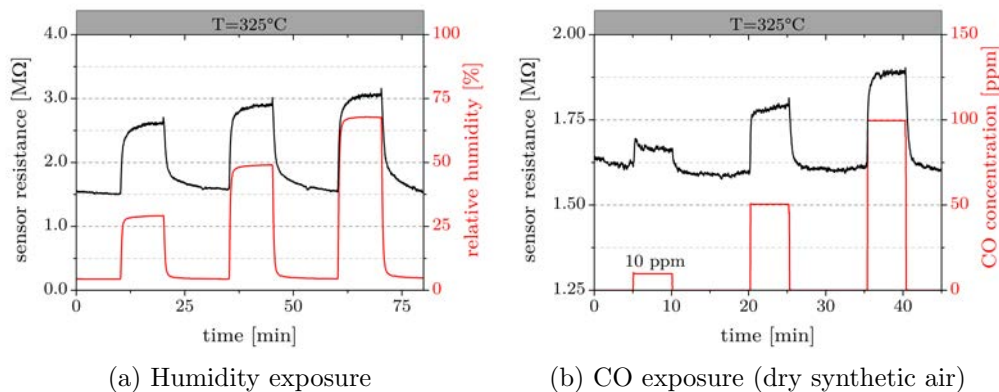


Figure 9.5: Gas measurements on CMOS integrated CuO nanowire array



## 10 Outlook

Decoration of metal oxide nanowires with metal nanoparticles is known as powerful technique in order to achieve improved gas selectivity, in particular in combination with electronic nose approaches [18]. Results on Au nanoparticle decorated ZnO nanowires have been presented in Chapter 7.3 of this thesis. For the future, nanowire decoration with nanoparticles by means of magnetron sputter gas aggregation is proposed. First experiments were conducted at Okinawa Institute of Science and Technology (Japan) on single CuO nanowires and multiple CuO nanowire array devices (Fig.10.1). This method is expected to be ideally suited for the gas sensing application due to its versatility and the high degree of deposition parameter control.

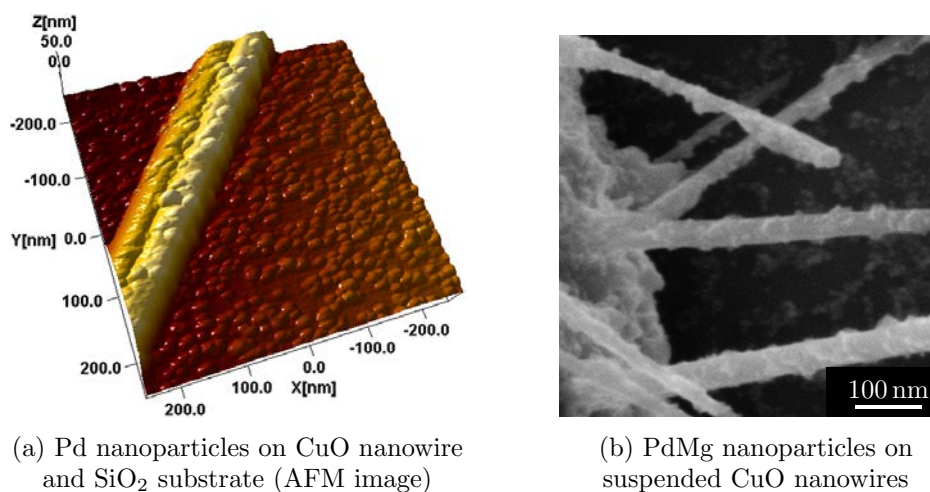


Figure 10.1: CuO nanowires decorated with metal nanoparticles

Heterostructures of different metal oxide materials are known as potential candidates for chemiresistive devices with improved performance. For instance, CuO deposition on ZnO nanowire based sensors was reported to lead to a considerable increase in gas response [159]. First experiments showed that the metal oxide nanowire synthesis techniques presented within this thesis may be easily adapted for the realization of CuO-ZnO heterostructures. CuO nanowire synthesis and subsequent ZnO nanostructure deposition could be achieved in a single synthesis step by changing gas environments. SEM

images and EDX characterization of preliminary experiments are shown in Fig.10.2. Due to the promising initial results additional studies are suggested for the future.

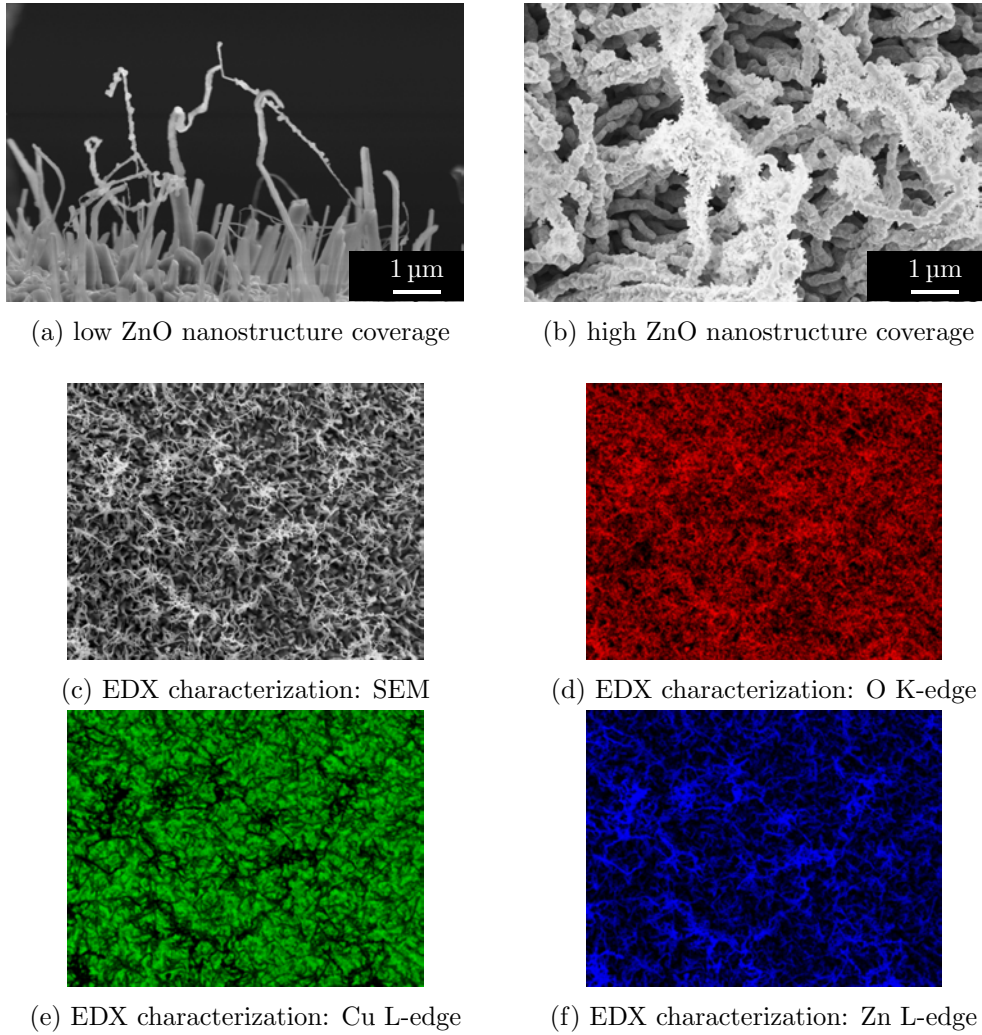


Figure 10.2: Synthesis of CuO-ZnO heterostructures

In addition, heterojunctions on CuO nanowires through surface functionalization with SnO<sub>2</sub> nanocrystals were reported to improve the gas sensing properties [161]. Within the research work of this thesis a novel self-aligned fabrication method for longitudinal SnO<sub>2</sub> heterojunctions on CuO nanowires has been demonstrated. Spray pyrolysis of SnO<sub>2</sub> thin films [266] was performed on SiO<sub>2</sub> substrates with randomly dispersed single CuO nanowires.

A cross-sectional TEM image of a CuO-SnO<sub>2</sub> heterostructure is shown in Fig.10.3a. After an additional Ar ion etching step the top CuO nanowire surface could be exposed and longitudinal SnO<sub>2</sub> heterojunctions remained at both sides of the CuO nanowire (Fig.10.3b). Further investigations on the gas sensing properties of such devices is expected to be highly promising in terms of sensitivity and selectivity improvements.

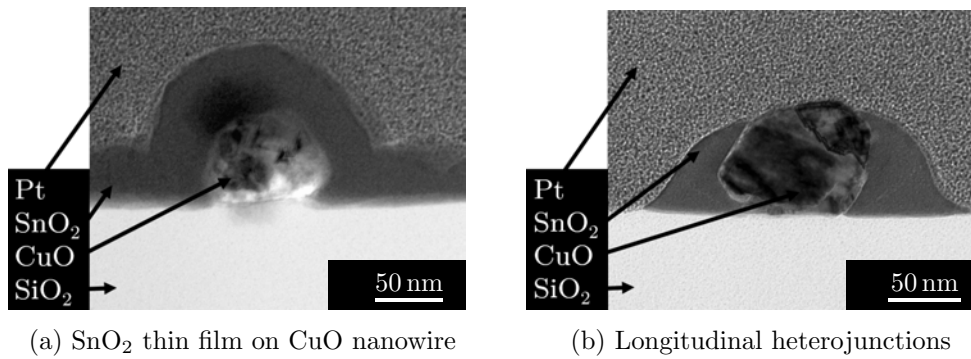


Figure 10.3: Self-aligned fabrication of CuO-SnO<sub>2</sub> heterojunctions by Ar ion etching

CMOS integration is a crucial step for the realization of miniaturized, inexpensive gas sensor systems with high performance [104]. Within this thesis CuO nanowire array devices integrated on CMOS fabricated microhotplates have been demonstrated and their gas sensing performance has been validated. The low thermal time constant of the microhotplate devices enables the possibility of fast operation temperature modulation of the CuO nanowire array devices, which is expected to lead to enhanced gas selectivity. Furthermore, the simultaneous integration of CuO nanowire arrays, ZnO nanowire arrays and nanocrystalline SnO<sub>2</sub> thin films is envisaged in the future and is considered as major step towards the realization of electronic nose systems based on CMOS integrated nanomaterials. The combination of on-chip electronics and low power consumption microhotplates is predicted to result in efficient gas sensor devices suitable for daily life applications.

## 11 Conclusion

Within the framework of this thesis, CuO and ZnO nanowires were studied in terms of synthesis, characterization, device fabrication, CMOS integration and electrical as well as gas sensing characterization. The main findings may be recapitulated as follows:

CuO and ZnO nanowires were successfully synthesized using thermal oxidation and vapor phase methods. Different growth substrates and synthesis parameters resulted in adjustable nanowire diameters and lengths ranging from few  $\mu\text{m}$  up to several tens of  $\mu\text{m}$ . Various techniques were employed for nanomaterial characterization and the synthesis results could be correlated with established literature growth models. In particular nanowire synthesis by thermal oxidation of microstructured Cu and Zn thin films was found to be suitable for growth of nanowires with small diameters between 10 nm and 30 nm at defined substrate positions.

Based on the nanowire synthesis results, several different types of devices were realized. Single CuO nanowire devices were fabricated in two-point, four-point and suspended configuration and the electrical properties were extensively characterized. The gas sensing properties of single CuO nanowires were studied during exposure to water vapor and CO in the ppm-level concentration range. The CO response of several different single CuO nanowire devices was compared and implications on the sensing mechanism were discussed.

Single ZnO nanowires were employed in a two-point configuration and were studied regarding self-heated gas sensing by utilizing the Joule effect. The devices showed reproducible linear IV characteristics and the single ZnO nanowires could sustain high maximum current densities up to approximately  $10^{10} \text{ A/m}^2$ , which is an excellent result compared to other literature reports. Gas sensing experiments during humidity exposure for three different biasing conditions confirmed that the presented single ZnO nanowire devices are suitable for self-heated gas sensor operation.

Although single nanowire sensors are well suited as model system for the characterization of the gas sensitivity of a single nanowire channel, the nanowire transfer process step and variations of nanowire diameters make this sensor concept problematic in terms of device reproducibility. Therefore a specific fabrication technology was used for direct integration of CuO and ZnO nanowire arrays by thermal oxidation of Cu and Zn microstructures. The main advantages of thermal oxidation synthesis are low cost, simplicity and moderate process temperatures around 400 °C, which makes this technique compatible with CMOS backend integration. Due to specific geometric configurations, the gaps between adjacent thermally oxidized structures were bridged by multiple CuO or ZnO nanowires, which could be thus employed as resistive device components. Consequently, no additional nanowire transfer process and no further fabrication steps were required after nanowire synthesis, which avoids potential surface contamination. CuO nanowire, ZnO nanowire and ZnO/Au nanowire array devices were realized and their gas sensing properties for the detection of CO and H<sub>2</sub>S were extensively characterized. In particular CuO nanowire array devices were found to be suitable for highly sensitive H<sub>2</sub>S detection down to concentrations as low as 1 ppb, which is among the best literature results reported for conductometric H<sub>2</sub>S sensors.

Humidity interference effects during CO and H<sub>2</sub>S exposure were thoroughly studied using different types of CuO nanowire gas sensors. In general, favorable gas sensing properties in humid atmosphere were found and thus CuO nanowire devices are a promising candidate for sensor operation under realistic ambient air conditions in the presence of water vapor. Furthermore, a sensing mechanism model was proposed in order to explain the observed experimental results for the different sensor realizations. As the influence of humidity on the gas sensor response of CuO based devices is hardly explored in literature, the presented findings may contribute to an improved understanding of the gas sensing mechanism in dry and humid atmosphere.

Most importantly, the integration of CuO nanowire arrays on CMOS microhotplates was demonstrated. Thermal oxidation of evaporated Cu microstructures and the resulting CuO nanowire growth was achieved by local heating of the microhotplate devices. In contrast to heating of the whole substrate for nanowire synthesis, the proposed method could be possibly performed on already packaged samples directly before gas sensor operation. Consequently, potential surface contaminations are avoided as no further processing steps are required after CuO nanowire growth. Furthermore, local nanowire synthesis may enable the simultaneous integration with other sensing materials not suitable for high temperature treatments, such as conductive polymers for instance. However, thermal oxidation synthesis of CuO nanowires is CMOS backend compatible due to the low process temperature (350 °C) and can be in principle performed on wafer-scale. The gas sensing properties of the CuO nanowire array devices on CMOS microhotplates were found to be well comparable with results achieved on samples heated by means of external microheaters, which validates the feasibility of the overall sensor integration concept.

In summary several different types of conductometric gas sensors based on metal oxide nanowires could be realized. The gas sensing properties were extensively characterized, in particular for the detection of the toxic gases CO (ppm-level range) and H<sub>2</sub>S (ppb-level range). Due to the excellent sensor performances potential applications in industrial occupational health and safety or in environmental air quality monitoring can be envisaged. CMOS compatible fabrication technologies for efficient nanowire device integration were developed, which are suitable for high volume industrial production on wafer scale. The integration of CuO nanowire arrays on CMOS microhotplates resulted in miniaturized gas sensing devices which could be operated at a low power consumption of less than 20 mW. It is expected that the combination of CMOS technology and nanomaterials will lead to the realization of next-generation smart gas sensor systems for daily life applications.

Finally it has to be noted that several results achieved within this thesis contributed to the successful submission of the project proposal "Multi Sensor Platform for Smart Building Management" (MSP), which is funded by the European Union under Framework Programme 7, Grant Agreement No.611887 (see <http://www.multisensorplatform.eu>). The three-year project focuses on Key Enabling Technologies such as 3D system integration using through-silicon vias as well as CMOS integration of nanotechnology-based sensors. These novel technologies are expected to result in innovative sensor systems for smart building management or smartphone-integrated air quality monitoring devices. MSP is coordinated by the Materials Center Leoben and comprises 17 partners from six European countries.

## References

- [1] N. Yamazoe, “Toward innovations of gas sensor technology,” *Sensors and Actuators B: Chemical*, vol. 108, pp. 2–14, 2005.
- [2] K. Wetchakun, T. Samerjai, N. Tamaekong, C. Liewhiran, C. Siriwong, V. Kruefu, A. Wisitsoraat, A. Tuantranont, and S. Phanichphant, “Semiconducting metal oxides as sensors for environmentally hazardous gases,” *Sensors and Actuators B: Chemical*, vol. 160, pp. 580–591, 2011.
- [3] S. De Vito, “Challenges in wireless chemical sensor networks,” in *Building Sensor Networks: from Design to Applications* (I. Nikolaidis and K. Iniewski, eds.), Boca Raton: CRC Press, 2014. ISBN: 978-1-4665-6272-1.
- [4] E. Comini, G. Faglia, and G. Sberveglieri, *Solid State Gas Sensing*. New York: Springer, 2009. ISBN: 978-0-387-09664-3.
- [5] I.-D. Kim, A. Rothschild, and H. L. Tuller, “Advances and new directions in gas-sensing devices,” *Acta Materialia*, vol. 61, pp. 974–1000, 2013.
- [6] C. Griessler, E. Brunet, T. Maier, S. Steinhauer, A. Köck, T. Jordi, F. Schrank, and M. Schrems, “Tin oxide nanosensors for highly sensitive toxic gas detection and their 3D system integration,” *Microelectronic Engineering*, vol. 88, pp. 1779–1781, 2011.
- [7] E. Comini and G. Sberveglieri, “Metal oxide nanowires as chemical sensors,” *Materials Today*, vol. 13, pp. 36–44, 2010.
- [8] V. V. Sysoev, T. Schneider, J. Goschnick, I. Kiselev, W. Habicht, H. Hahn, E. Strelcov, and A. Kolmakov, “Percolating SnO<sub>2</sub> nanowire network as a stable gas sensor: Direct comparison of long-term performance versus SnO<sub>2</sub> nanoparticle films,” *Sensors and Actuators B: Chemical*, vol. 139, pp. 699–703, 2009.
- [9] E. Comini, G. Faglia, M. Ferroni, A. Ponzoni, A. Vomiero, and G. Sberveglieri, “Metal oxide nanowires: Preparation and application in gas sensing,” *Journal of Molecular Catalysis A: Chemical*, vol. 305, pp. 170–177, 2009.
- [10] A. Kolmakov, D. O. Klenov, Y. Lilach, S. Stemmer, and M. Moskovits, “Enhanced gas sensing by individual SnO<sub>2</sub> nanowires and nanobelts



- functionalized with Pd catalyst particles,” *Nano Letters*, vol. 5, pp. 667–673, 2005.
- [11] L. Liao, H. X. Mai, Q. Yuan, H. B. Lu, J. C. Li, C. Liu, C. H. Yan, Z. X. Shen, and T. Yu, “Single CeO<sub>2</sub> nanowire gas sensor supported with Pt nanocrystals: Gas sensitivity, surface bond states, and chemical mechanism,” *The Journal of Physical Chemistry C*, vol. 112, pp. 9061–9065, 2008.
- [12] S.-W. Choi and S. S. Kim, “Room temperature CO sensing of selectively grown networked ZnO nanowires by Pd nanodot functionalization,” *Sensors and Actuators B: Chemical*, vol. 168, pp. 8–13, 2012.
- [13] N. S. Ramgir, P. K. Sharma, N. Datta, M. Kaur, A. K. Debnath, D. K. Aswal, and S. K. Gupta, “Room temperature H<sub>2</sub>S sensor based on Au modified ZnO nanowires,” *Sensors and Actuators B: Chemical*, vol. 186, pp. 718–726, 2013.
- [14] D. C. Meier, S. Semancik, B. Button, E. Strelcov, and A. Kolmakov, “Coupling nanowire chemiresistors with MEMS microhotplate gas sensing platforms,” *Applied Physics Letters*, vol. 91, p. 063118, 2007.
- [15] E. N. Dattoli, A. V. Davydov, and K. D. Benkstein, “Tin oxide nanowire sensor with integrated temperature and gate control for multi-gas recognition,” *Nanoscale*, vol. 4, pp. 1760–1769, 2012.
- [16] V. V. Sysoev, B. K. Button, K. Wepsiec, S. Dmitriev, and A. Kolmakov, “Toward the nanoscopic “electronic nose”: Hydrogen vs carbon monoxide discrimination with an array of individual metal oxide nano- and mesowire sensors,” *Nano Letters*, vol. 6, pp. 1584–1588, 2006.
- [17] P.-C. Chen, F. N. Ishikawa, H.-K. Chang, K. Ryu, and C. Zhou, “A nanoelectronic nose: A hybrid nanowire/carbon nanotube sensor array with integrated micromachined hotplates for sensitive gas discrimination,” *Nanotechnology*, vol. 20, p. 125503, 2009.
- [18] J. M. Baik, M. Zielke, M. H. Kim, K. L. Turner, A. M. Wodtke, and M. Moskovits, “Tin-oxide-nanowire-based electronic nose using heterogeneous catalysis as a functionalization strategy,” *ACS Nano*, vol. 4, pp. 3117–3122, 2010.
- [19] V. V. Sysoev, E. Strelcov, M. Sommer, M. Bruns, I. Kiselev, W. Habicht, S. Kar, L. Gregoratti, M. Kiskinova, and A. Kolmakov,

- “Single-nanobelt electronic nose: Engineering and tests of the simplest analytical element,” *ACS Nano*, vol. 4, pp. 4487–4494, 2010.
- [20] V. V. Sysoev, J. Goschnick, T. Schneider, E. Strelcov, and A. Kolmakov, “A gradient microarray electronic nose based on percolating SnO<sub>2</sub> nanowire sensing elements,” *Nano Letters*, vol. 7, pp. 3182–3188, 2007.
- [21] Z. Fan and J. G. Lu, “Metal oxide nanowires: Fundamentals and sensor applications,” in *Metal Oxide Nanomaterials for Chemical Sensors* (M. A. Carpenter, S. Mathur, and A. Kolmakov, eds.), New York: Springer, 2013. ISBN: 978-1-4614-5394-9.
- [22] Y. Zhang, A. Kolmakov, S. Chretien, H. Metiu, and M. Moskovits, “Control of catalytic reactions at the surface of a metal oxide nanowire by manipulating electron density inside it,” *Nano Letters*, vol. 4, pp. 403–407, 2004.
- [23] Z. Fan and J. G. Lu, “Gate-refreshable nanowire chemical sensors,” *Applied Physics Letters*, vol. 86, p. 123510, 2005.
- [24] A. Gurlo and R. Riedel, “In situ and operando spectroscopy for assessing mechanisms of gas sensing,” *Angewandte Chemie International Edition*, vol. 46, pp. 3826–3848, 2007.
- [25] G. Korotcenkov, “The role of morphology and crystallographic structure of metal oxides in response of conductometric-type gas sensors,” *Materials Science and Engineering R*, vol. 61, pp. 1–39, 2008.
- [26] A. Gurlo, “Nanosensors: Towards morphological control of gas sensing activity. SnO<sub>2</sub>, In<sub>2</sub>O<sub>3</sub>, ZnO and WO<sub>3</sub> case studies,” *Nanoscale*, vol. 3, pp. 154–65, 2011.
- [27] J. D. Prades, R. Jimenez-Diaz, F. Hernandez-Ramirez, J. Pan, A. Romano-Rodriguez, S. Mathur, and J. R. Morante, “Direct observation of the gas-surface interaction kinetics in nanowires through pulsed self-heating assisted conductometric measurements,” *Applied Physics Letters*, vol. 95, p. 053101, 2009.
- [28] J. R. Morante, “Chemical to electrical transduction mechanisms from single metal oxide nanowire measurements: Response time constant analysis,” *Nanotechnology*, vol. 24, p. 444004, 2013.

- [29] F. Hernandez-Ramirez, J. D. Prades, A. Tarancon, S. Barth, O. Casals, R. Jimenez-Diaz, E. Pellicer, J. Rodriguez, J. R. Morante, M. A. Juli, S. Mathur, and A. Romano-Rodriguez, "Insight into the role of oxygen diffusion in the sensing mechanisms of SnO<sub>2</sub> nanowires," *Advanced Functional Materials*, vol. 18, pp. 2990–2994, 2008.
- [30] M. Spencer, "Gas sensing applications of 1D-nanostructured zinc oxide: Insights from density functional theory calculations," *Progress in Materials Science*, vol. 57, pp. 437–486, 2012.
- [31] D. Li, J. Hu, R. Wu, and J. G. Lu, "Conductometric chemical sensor based on individual CuO nanowires," *Nanotechnology*, vol. 21, p. 485502, 2010.
- [32] A. Maiti, J. A. Rodriguez, M. Law, P. Kung, J. R. McKinney, and P. Yang, "SnO<sub>2</sub> nanoribbons as NO<sub>2</sub> sensors: Insights from first principles calculations," *Nano Letters*, vol. 3, pp. 1025–1028, 2003.
- [33] F. Shao, M. Hoffmann, J. D. Prades, J. R. Morante, N. Lopez, and F. Hernandez-Ramirez, "Interaction mechanisms of ammonia and tin oxide: A combined analysis using single nanowire devices and DFT calculations," *The Journal of Physical Chemistry C*, vol. 117, pp. 3520–3526, 2013.
- [34] E. Strelcov, S. Dmitriev, B. Button, J. Cothren, V. V. Sysoev, and A. Kolmakov, "Evidence of the self-heating effect on surface reactivity and gas sensing of metal oxide nanowire chemiresistors," *Nanotechnology*, vol. 19, p. 355502, 2008.
- [35] J. D. Prades, R. Jimenez-Diaz, F. Hernandez-Ramirez, S. Barth, A. Cirera, A. Romano-Rodriguez, S. Mathur, and J. R. Morante, "Ultralow power consumption gas sensors based on self-heated individual nanowires," *Applied Physics Letters*, vol. 93, p. 123110, 2008.
- [36] J. D. Prades, F. Hernandez-Ramirez, T. Fischer, M. Hoffmann, R. Müller, N. Lopez, S. Mathur, and J. R. Morante, "Quantitative analysis of CO-humidity gas mixtures with self-heated nanowires operated in pulsed mode," *Applied Physics Letters*, vol. 97, p. 243105, 2010.
- [37] J. D. Prades, R. Jimenez-Diaz, F. Hernandez-Ramirez, A. Cirera, A. Romano-Rodriguez, and J. R. Morante, "Harnessing self-heating in nanowires for energy efficient, fully autonomous and ultra-fast gas sensors," *Sensors and Actuators B: Chemical*, vol. 144, pp. 1–5, 2010.

- [38] J. Smedley, F. Dick, and S. Sadhra, *Oxford Handbook of Occupational Health*. Oxford: Oxford University Press, 2013. ISBN: 978-0-19-965162-7.
- [39] S. T. Omaye, “Metabolic modulation of carbon monoxide toxicity,” *Toxicology*, vol. 180, pp. 139–150, 2002.
- [40] World Health Organization, *Air Quality Guidelines for Europe*. Copenhagen: WHO Regional Office for Europe, 2000. ISBN: 92-890-1358-3.
- [41] T. L. Guidotti, “Hydrogen sulfide: Advances in understanding human toxicity,” *International Journal of Toxicology*, vol. 29, pp. 569–581, 2010.
- [42] S. N. Das, J. P. Kar, J.-H. Choi, T. I. Lee, K.-J. Moon, and J.-M. Myoung, “Fabrication and characterization of ZnO single nanowire-based hydrogen sensor,” *The Journal of Physical Chemistry C*, vol. 114, pp. 1689–1693, 2010.
- [43] O. Lupan, V. V. Ursaki, G. Chai, L. Chow, G. A. Emelchenko, I. M. Tiginyanu, A. N. Gruzintsev, and A. N. Redkin, “Selective hydrogen gas nanosensor using individual ZnO nanowire with fast response at room temperature,” *Sensors and Actuators B: Chemical*, vol. 144, pp. 56–66, 2010.
- [44] N. Mohseni Kiasari, S. Soltanian, B. Gholamkhash, and P. Servati, “Room temperature ultra-sensitive resistive humidity sensor based on single zinc oxide nanowire,” *Sensors and Actuators A: Physical*, vol. 182, pp. 101–105, 2012.
- [45] T.-J. Hsueh, Y.-W. Chen, S.-J. Chang, S.-F. Wang, C.-L. Hsu, Y.-R. Lin, T.-S. Lin, and I.-C. Chen, “ZnO nanowire-based CO sensors prepared on patterned ZnO:Ga/SiO<sub>2</sub>/Si templates,” *Sensors and Actuators B: Chemical*, vol. 125, pp. 498–503, 2007.
- [46] T.-J. Hsueh, C.-L. Hsu, S.-J. Chang, and I.-C. Chen, “Laterally grown ZnO nanowire ethanol gas sensors,” *Sensors and Actuators B: Chemical*, vol. 126, pp. 473–477, 2007.
- [47] S. Santra, P. K. Guha, S. Z. Ali, P. Hiralal, H. E. Unalan, J. A. Covington, G. Amaratunga, W. I. Milne, J. W. Gardner, and F. Udrea, “ZnO nanowires grown on SOI CMOS substrate for ethanol sensing,” *Sensors and Actuators B: Chemical*, vol. 146, pp. 559–565, 2010.

- [48] Z. W. Pan, Z. R. Dai, and Z. L. Wang, "Nanobelts of semiconducting oxides," *Science*, vol. 291, pp. 1947–1949, 2001.
- [49] B. D. Yao, Y. F. Chan, and N. Wang, "Formation of ZnO nanostructures by a simple way of thermal evaporation," *Applied Physics Letters*, vol. 81, p. 757, 2002.
- [50] F. Shao, F. Hernandez-Ramirez, J. D. Prades, C. Fabrega, T. Andreu, and J. R. Morante, "Copper (II) oxide nanowires for p-type conductometric NH<sub>3</sub> sensing," *Applied Surface Science*, vol. 311, pp. 177–181, 2014.
- [51] L. Liao, Z. Zhang, B. Yan, Z. Zheng, Q. L. Bao, T. Wu, C. M. Li, Z. X. Shen, J. X. Zhang, H. Gong, J. C. Li, and T. Yu, "Multifunctional CuO nanowire devices: p-type field effect transistors and CO gas sensors," *Nanotechnology*, vol. 20, p. 085203, 2009.
- [52] B. J. Hansen, N. Kouklin, G. Lu, I.-K. Lin, J. Chen, and X. Zhang, "Transport, analyte detection, and opto-electronic response of p-type CuO nanowires," *The Journal of Physical Chemistry C*, vol. 114, pp. 2440–2447, 2010.
- [53] Y.-S. Kim, I.-S. Hwang, S.-J. Kim, C.-Y. Lee, and J.-H. Lee, "CuO nanowire gas sensors for air quality control in automotive cabin," *Sensors and Actuators B: Chemical*, vol. 135, pp. 298–303, 2008.
- [54] J. Chen, K. Wang, L. Hartman, and W. Zhou, "H<sub>2</sub>S detection by vertically aligned CuO nanowire array sensors," *The Journal of Physical Chemistry C*, vol. 112, pp. 16017–16021, 2008.
- [55] X. Li, Y. Wang, Y. Lei, and Z. Gu, "Highly sensitive H<sub>2</sub>S sensor based on template-synthesized CuO nanowires," *RSC Advances*, vol. 2, pp. 2302–2307, 2012.
- [56] I. Simon, N. Bârsan, M. Bauer, and U. Weimar, "Micromachined metal oxide gas sensors: Opportunities to improve sensor performance," *Sensors and Actuators B: Chemical*, vol. 73, pp. 1–26, 2001.
- [57] S. Z. Ali, F. Udrea, W. I. Milne, and J. W. Gardner, "Tungsten-based SOI microhotplates for smart gas sensors," *Journal of Microelectromechanical Systems*, vol. 17, pp. 1408–1417, 2008.
- [58] P. K. Guha, S. Santra, and J. W. Gardner, "CMOS integrated gas sensors," in *Measurement, Instrumentation, and Sensors Handbook*

- (J. G. Webster and H. Eren, eds.), Boca Raton: CRC Press, 2014. ISBN: 978-1-4398-4891-3.
- [59] K. Grossmann, U. Weimar, and N. Bârsan, “Semiconducting metal oxides based gas sensors,” in *Oxide Semiconductors* (B. G. Svensson, S. J. Pearton, and C. Jagadish, eds.), London: Academic Press, 2013. ISBN: 978-0-12-396489-2.
- [60] F.-G. Banica, *Chemical Sensors and Biosensors*. Chichester: John Wiley & Sons, 2012. ISBN: 978-0-470-71066-1.
- [61] R. Lalauze, *Physical Chemistry of Solid-Gas Interfaces*. Hoboken: John Wiley & Sons, 2008. ISBN: 978-1-84821-041-7.
- [62] S. R. Morrison, *The Chemical Physics of Surfaces*. New York: Plenum Press, 1990. ISBN: 978-1-4615-8009-6.
- [63] P. Atkins and J. de Paula, *Physical Chemistry*. Oxford: Oxford University Press, 2006. ISBN: 978-0-19-954337-3.
- [64] R. G. Mortimer, *Physical Chemistry*. London: Elsevier Academic Press, 2008. ISBN: 978-0-12-370617-1.
- [65] M. J. Madou and S. R. Morrison, *Chemical Sensing with Solid State Devices*. London: Academic Press, 1989. ISBN: 978-0-12-464965-1.
- [66] M. Batzill and U. Diebold, “The surface and materials science of tin oxide,” *Progress in Surface Science*, vol. 79, pp. 47–154, 2005.
- [67] W. Goepel and K. D. Schierbaum, “SnO<sub>2</sub> sensors: Current status and future prospects,” *Sensors and Actuators B: Chemical*, vol. 26, pp. 1–12, 1995.
- [68] N. Bârsan and U. Weimar, “Conduction model of metal oxide gas sensors,” *Journal of Electroceramics*, vol. 7, pp. 143–167, 2001.
- [69] N. Bârsan and U. Weimar, “Understanding the fundamental principles of metal oxide based gas sensors; the example of CO sensing with SnO<sub>2</sub> sensors in the presence of humidity,” *Journal of Physics: Condensed Matter*, vol. 15, pp. 813–839, 2003.
- [70] N. Bârsan, C. Simion, T. Heine, S. Pokhrel, and U. Weimar, “Modeling of sensing and transduction for p-type semiconducting metal oxide based gas sensors,” *Journal of Electroceramics*, vol. 25, pp. 11–19, 2010.

- [71] N. Bârsan, M. Hübner, and U. Weimar, “Conduction mechanisms in SnO<sub>2</sub> based polycrystalline thick film gas sensors exposed to CO and H<sub>2</sub> in different oxygen backgrounds,” *Sensors and Actuators B: Chemical*, vol. 157, pp. 510–517, 2011.
- [72] L. J. Brillson, *Surfaces and Interfaces of Electronic Materials*. Weinheim: Wiley-VCH, 2010. ISBN: 978-3-527-40915-0.
- [73] N. Yamazoe and K. Shimano, “Theory of power laws for semiconductor gas sensors,” *Sensors and Actuators B: Chemical*, vol. 128, pp. 566–573, Jan. 2008.
- [74] G. Eranna, *Metal Oxide Nanostructures as Gas Sensing Devices*. Boca Raton: CRC Press, 2012. ISBN: 978-1-4398-6340-4.
- [75] J. N. Zemel, “Theoretical description of gas-film interaction on SnO<sub>x</sub>,” *Thin Solid Films*, vol. 163, pp. 189–202, 1988.
- [76] X. Du, Y. Du, and S. M. George, “CO gas sensing by ultrathin tin oxide films grown by atomic layer deposition using transmission FTIR spectroscopy,” *The Journal of Physical Chemistry A*, vol. 112, pp. 9211–9219, 2008.
- [77] A. Gurlo, “Insights into the mechanism of gas sensor operation,” in *Metal Oxide Nanomaterials for Chemical Sensors* (M. A. Carpenter, S. Mathur, and A. Kolmakov, eds.), New York: Springer, 2013. ISBN: 978-1-4614-5394-9.
- [78] M. Hübner, C. E. Simion, A. Tomescu-Stănoiu, S. Pokhrel, N. Bârsan, and U. Weimar, “Influence of humidity on CO sensing with p-type CuO thick film gas sensors,” *Sensors and Actuators B: Chemical*, vol. 153, pp. 347–353, 2011.
- [79] G. Korotcenkov, “Metal oxides for solid-state gas sensors: What determines our choice?,” *Materials Science and Engineering B*, vol. 139, pp. 1–23, 2007.
- [80] M. Graf, A. Gurlo, N. Bârsan, U. Weimar, and A. Hierlemann, “Microfabricated gas sensor systems with sensitive nanocrystalline metal-oxide films,” *Journal of Nanoparticle Research*, vol. 8, pp. 823–839, 2006.
- [81] M. Kaur, D. Aswal, and J. Yakhmi, “Chemiresistor gas sensors: Materials, mechanisms and fabrication,” in *Science and Technology of*

*Chemiresistor Gas Sensors* (D. Aswal and S. Gupta, eds.), New York: Nova Science, 2007. ISBN: 978-1-60021-514-8.

- [82] N. Yamazoe and K. Shimano, “Theoretical approach to the gas response of oxide semiconductor film devices under control of gas diffusion and reaction effects,” *Sensors and Actuators B: Chemical*, vol. 154, pp. 277–282, 2011.
- [83] G. Korotcenkov, “Gas response control through structural and chemical modification of metal oxide films: State of the art and approaches,” *Sensors and Actuators B: Chemical*, vol. 107, pp. 209–232, 2005.
- [84] M. Tonezzer and N. V. Hieu, “Size-dependent response of single-nanowire gas sensors,” *Sensors and Actuators B: Chemical*, vol. 163, pp. 146–152, 2012.
- [85] S. Ahlers, G. Müller, and T. Doll, “A rate equation approach to the gas sensitivity of thin film metal oxide materials,” *Sensors and Actuators B: Chemical*, vol. 107, pp. 587–599, 2005.
- [86] M. A. Kozhushner, L. I. Trakhtenberg, A. C. Landerville, and I. I. Oleynik, “Theory of sensing response of nanostructured tin-dioxide thin films to reducing hydrogen gas,” *The Journal of Physical Chemistry C*, vol. 117, pp. 11562–11568, 2013.
- [87] G. Korotcenkov and B. K. Cho, “Engineering approaches for the improvement of conductometric gas sensor parameters; Part 1. Improvement of sensor sensitivity and selectivity,” *Sensors and Actuators B: Chemical*, vol. 188, pp. 709–728, 2013.
- [88] A. Cabot, A. Dieguez, A. Romano-Rodriguez, J. R. Morante, and N. Bârsan, “Influence of the catalytic introduction procedure on the nano-SnO<sub>2</sub> gas sensor performances; Where and how stay the catalytic atoms?,” *Sensors and Actuators B: Chemical*, vol. 79, pp. 98–106, 2001.
- [89] T. A. Miller, S. D. Bakrania, C. Perez, and M. S. Wooldridge, “Nanostructured tin dioxide materials for gas sensor applications,” in *Functional Nanomaterials* (K. E. Geckeler and E. Rosenberg, eds.), Valencia: American Scientific Publishers, 2006. ISBN: 978-1-58883-067-8.
- [90] M. E. Franke, T. J. Koplín, and U. Simon, “Metal and metal oxide nanoparticles in chemiresistors: Does the nanoscale matter?,” *Small*, vol. 2, pp. 36–50, 2006.



- [91] N. Yamazoe, G. Sakai, and K. Shimano, "Oxide semiconductor gas sensors," *Catalysis Surveys from Asia*, vol. 7, pp. 63–75, 2003.
- [92] A. P. Lee and B. J. Reedy, "Temperature modulation in semiconductor gas sensing," *Sensors and Actuators B: Chemical*, vol. 60, pp. 35–42, 1999.
- [93] A. Fort, M. Gregorkiewitz, N. Machetti, S. Rocchi, B. Serrano, L. Tondi, N. Ulivieri, V. Vignoli, G. Faglia, and E. Comini, "Selectivity enhancement of SnO<sub>2</sub> sensors by means of operating temperature modulation," *Thin Solid Films*, vol. 418, pp. 2–8, 2002.
- [94] J. Ding, T. J. McAvoy, R. E. Cavicchi, and S. Semancik, "Surface state trapping models for SnO<sub>2</sub>-based microhotplate sensors," *Sensors and Actuators B: Chemical*, vol. 77, pp. 597–613, 2001.
- [95] R. Ionescu, E. Llobet, S. Al-Khalifa, J. W. Gardner, X. Vilanova, J. Brezmes, and X. Correig, "Response model for thermally modulated tin oxide-based microhotplate gas sensors," *Sensors and Actuators B: Chemical*, vol. 95, pp. 203–211, 2003.
- [96] A. Fort, S. Rocchi, M. B. Serrano-Santos, R. Spinicci, and V. Vignoli, "Surface state model for conductance responses during thermal-modulation of SnO<sub>2</sub>-based thick film sensors: Part I - model derivation," *IEEE Transactions on Instrumentation and Measurement*, vol. 55, pp. 2102–2106, 2006.
- [97] A. Fort, M. Mugnaini, S. Rocchi, M. B. Serrano-Santos, R. Spinicci, and V. Vignoli, "Surface state model for conductance responses during thermal-modulation of SnO<sub>2</sub>-based thick film sensors: Part II - experimental verification," *IEEE Transactions on Instrumentation and Measurement*, vol. 55, pp. 2107–2117, 2006.
- [98] A. Vergara, E. Llobet, J. Brezmes, P. Ivanov, C. Cané, I. Gràcia, X. Vilanova, and X. Correig, "Quantitative gas mixture analysis using temperature-modulated micro-hotplate gas sensors: Selection and validation of the optimal modulating frequencies," *Sensors and Actuators B: Chemical*, vol. 123, pp. 1002–1016, 2007.
- [99] J. Fonollosa, L. Fernández, R. Huerta, A. Gutiérrez-Gálvez, and S. Marco, "Temperature optimization of metal oxide sensor arrays using mutual information," *Sensors and Actuators B: Chemical*, vol. 187, pp. 331–339, 2013.

- [100] E. Martinelli, D. Polese, A. Catini, A. D'Amico, and C. Di Natale, "Self-adapted temperature modulation in metal-oxide semiconductor gas sensors," *Sensors and Actuators B: Chemical*, vol. 161, pp. 534–541, 2012.
- [101] A. Hierlemann and R. Gutierrez-Osuna, "Higher-order chemical sensing," *Chemical Reviews*, vol. 108, pp. 563–613, 2008.
- [102] T. C. Pearce, S. S. Schiffman, H. T. Nagle, and J. W. Gardner, eds., *Handbook of Machine Olfaction: Electronic Nose Technology*. Weinheim: Wiley-VCH, 2003. ISBN: 978-3-527-60563-7.
- [103] K. J. Albert, N. S. Lewis, C. L. Schauer, G. A. Sotzing, S. E. Stitzel, T. P. Vaid, and D. R. Walt, "Cross-reactive chemical sensor arrays," *Chemical Reviews*, vol. 100, pp. 2595–2626, 2000.
- [104] S.-W. Chiu and K.-T. Tang, "Towards a chemiresistive sensor - integrated electronic nose: A review," *Sensors*, vol. 13, pp. 14214–14247, 2013.
- [105] A. Ponzoni, E. Comini, I. Concina, M. Ferroni, M. Falasconi, E. Gobbi, V. Sberveglieri, and G. Sberveglieri, "Nanostructured metal oxide gas sensors, a survey of applications carried out at SENSOR lab, Brescia (Italy) in the security and food quality fields," *Sensors*, vol. 12, pp. 17023–17045, 2012.
- [106] K. Brudzewski, S. Osowski, and W. Pawlowski, "Metal oxide sensor arrays for detection of explosives at sub-parts-per million concentration levels by the differential electronic nose," *Sensors and Actuators B: Chemical*, vol. 161, pp. 528–533, 2012.
- [107] Z. Haddi, A. Amari, H. Alami, N. El Bari, E. Llobet, and B. Bouchikhi, "A portable electronic nose system for the identification of cannabis-based drugs," *Sensors and Actuators B: Chemical*, vol. 155, pp. 456–463, 2011.
- [108] K. T. Ng, F. Boussaid, and A. Bermak, "A CMOS single-chip gas recognition circuit for metal oxide gas sensor arrays," *IEEE Transactions on Circuits and Systems I: Regular Papers*, vol. 58, pp. 1569–1580, 2011.
- [109] C. Thelander, P. Agarwal, S. Brongersma, J. Eymery, L. F. Feiner, A. Forchel, M. Scheffler, W. Riess, B. J. Ohlsson, U. Gösele, and L. Samuelson, "Nanowire-based one-dimensional electronics," *Materials Today*, vol. 9, pp. 28–35, 2006.

- [110] R. G. Hobbs, N. Petkov, and J. D. Holmes, “Semiconductor nanowire fabrication by bottom-up and top-down paradigms,” *Chemistry of Materials*, vol. 24, pp. 1975–1991, 2012.
- [111] N. Ramgir, N. Datta, M. Kaur, S. Kailasaganapathi, A. K. Debnath, D. K. Aswal, and S. K. Gupta, “Metal oxide nanowires for chemiresistive gas sensors: Issues, challenges and prospects,” *Colloids and Surfaces A: Physicochemical and Engineering Aspects*, vol. 439, pp. 101–116, 2013.
- [112] S. Raychaudhuri, S. A. Dayeh, D. Wang, and E. T. Yu, “Precise semiconductor nanowire placement through dielectrophoresis,” *Nano Letters*, vol. 9, pp. 2260–2266, 2009.
- [113] Y. Liu, J.-H. Chung, W. K. Liu, and R. S. Ruoff, “Dielectrophoretic assembly of nanowires,” *The Journal of Physical Chemistry B*, vol. 110, pp. 14098–14106, 2006.
- [114] X. Li, E. Chin, H. Sun, P. Kurup, and Z. Gu, “Fabrication and integration of metal oxide nanowire sensors using dielectrophoretic assembly and improved post-assembly processing,” *Sensors and Actuators B: Chemical*, vol. 148, pp. 404–412, 2010.
- [115] E. M. Freer, O. Grachev, and D. P. Stumbo, “High-yield self-limiting single-nanowire assembly with dielectrophoresis,” *Nature Nanotechnology*, vol. 5, pp. 525–530, 2010.
- [116] Z. Fan, J. C. Ho, T. Takahashi, R. Yerushalmi, K. Takei, A. C. Ford, Y.-L. Chueh, and A. Javey, “Toward the development of printable nanowire electronics and sensors,” *Advanced Materials*, vol. 21, pp. 3730–3743, 2009.
- [117] J. Yao, H. Yan, and C. M. Lieber, “A nanoscale combing technique for the large-scale assembly of highly aligned nanowires,” *Nature Nanotechnology*, vol. 8, pp. 329–335, 2013.
- [118] P. J. Pauzauskie, A. Radenovic, E. Trepagnier, H. Shroff, P. Yang, and J. Liphardt, “Optical trapping and integration of semiconductor nanowire assemblies in water,” *Nature Materials*, vol. 5, pp. 97–101, 2006.
- [119] F. Holzner, C. Kuemin, P. Paul, J. L. Hedrick, H. Wolf, N. D. Spencer, U. Duerig, and A. W. Knoll, “Directed placement of gold nanorods

- using a removable template for guided assembly,” *Nano Letters*, vol. 11, pp. 3957–3962, 2011.
- [120] X. Liu, Y.-Z. Long, L. Liao, X. Duan, and Z. Fan, “Large-scale integration of semiconductor nanowires for high-performance flexible electronics,” *ACS Nano*, vol. 6, pp. 1888–1900, 2012.
- [121] T. Bryllert, L.-E. Wernersson, T. Löwgren, and L. Samuelson, “Vertical wrap-gated nanowire transistors,” *Nanotechnology*, vol. 17, pp. S227–S230, 2006.
- [122] D. R. Kim, C. H. Lee, and X. Zheng, “Direct growth of nanowire logic gates and photovoltaic devices,” *Nano Letters*, vol. 10, pp. 1050–1054, 2010.
- [123] C. P. T. Svensson, T. Mårtensson, J. Trägårdh, C. Larsson, M. Rask, D. Hessman, L. Samuelson, and J. Ohlsson, “Monolithic GaAs/InGaP nanowire light emitting diodes on silicon,” *Nanotechnology*, vol. 19, p. 305201, 2008.
- [124] M. C. McAlpine, H. Ahmad, D. Wang, and J. R. Heath, “Highly ordered nanowire arrays on plastic substrates for ultrasensitive flexible chemical sensors,” *Nature Materials*, vol. 6, pp. 379–384, 2007.
- [125] Y.-J. Choi, I.-S. Hwang, J.-G. Park, K. J. Choi, J.-H. Park, and J.-H. Lee, “Novel fabrication of an SnO<sub>2</sub> nanowire gas sensor with high sensitivity,” *Nanotechnology*, vol. 19, p. 095508, 2008.
- [126] B. Wang, L. F. Zhu, Y. H. Yang, N. S. Xu, and G. W. Yang, “Fabrication of a SnO<sub>2</sub> nanowire gas sensor and sensor performance for hydrogen,” *The Journal of Physical Chemistry C*, vol. 112, pp. 6643–6647, 2008.
- [127] L. V. Thong, N. D. Hoa, D. T. T. Le, D. T. Viet, P. D. Tam, A.-T. Le, and N. V. Hieu, “On-chip fabrication of SnO<sub>2</sub>-nanowire gas sensor: The effect of growth time on sensor performance,” *Sensors and Actuators B: Chemical*, vol. 146, pp. 361–367, 2010.
- [128] S.-H. Jung, S.-W. Choi, and S. S. Kim, “Fabrication and properties of trench-structured networked SnO<sub>2</sub> nanowire gas sensors,” *Sensors and Actuators B: Chemical*, vol. 171-172, pp. 672–678, 2012.
- [129] G.-J. Sun, S.-W. Choi, S.-H. Jung, A. Katoch, and S. S. Kim, “V-groove SnO<sub>2</sub> nanowire sensors: Fabrication and Pt-nanoparticle decoration,” *Nanotechnology*, vol. 24, p. 025504, 2013.

- [130] A. Vomiero, A. Ponzoni, E. Comini, M. Ferroni, G. Faglia, and G. Sberveglieri, “Direct integration of metal oxide nanowires into an effective gas sensing device,” *Nanotechnology*, vol. 21, p. 145502, 2010.
- [131] M.-W. Ahn, K.-S. Park, J.-H. Heo, J.-G. Park, D.-W. Kim, K. J. Choi, J.-H. Lee, and S.-H. Hong, “Gas sensing properties of defect-controlled ZnO-nanowire gas sensor,” *Applied Physics Letters*, vol. 93, p. 263103, 2008.
- [132] M.-W. Ahn, K.-S. Park, J.-H. Heo, D.-W. Kim, K. Choi, and J.-G. Park, “On-chip fabrication of ZnO-nanowire gas sensor with high gas sensitivity,” *Sensors and Actuators B: Chemical*, vol. 138, pp. 168–173, 2009.
- [133] J. X. Wang, X. W. Sun, Y. Yang, H. Huang, Y. C. Lee, O. K. Tan, and L. Vayssieres, “Hydrothermally grown oriented ZnO nanorod arrays for gas sensing applications,” *Nanotechnology*, vol. 17, pp. 4995–4998, 2006.
- [134] J. S. Lloyd, C. M. Fung, D. Deganello, R. J. Wang, T. G. G. Maffei, S. P. Lau, and K. S. Teng, “Flexographic printing-assisted fabrication of ZnO nanowire devices,” *Nanotechnology*, vol. 24, p. 195602, 2013.
- [135] A. G. Milnes and D. L. Feucht, *Heterojunctions and metal semiconductor junctions*. New York: Academic Press, 1972. ISBN: 978-0-12-498050-1.
- [136] H. Lueth, *Solid Surfaces, Interfaces and Thin Films*. Heidelberg: Springer, 2010. ISBN: 978-3-642-13591-0.
- [137] S. M. Sze and K. K. Ng, *Physics of semiconductor devices*. Hoboken: John Wiley & Sons, 2007. ISBN: 978-0-471-14323-9.
- [138] S. S. Li, *Semiconductor physical electronics*. New York: Springer, 2006. ISBN: 978-0387-28893-2.
- [139] M. Razeghi, *Technology of quantum devices*. New York: Springer, 2010. ISBN: 978-1-4419-1055-4.
- [140] F. Léonard and A. A. Talin, “Size-dependent effects on electrical contacts to nanotubes and nanowires,” *Physical Review Letters*, vol. 97, p. 026804, 2006.

- [141] F. Léonard and A. A. Talin, “Electrical contacts to one- and two-dimensional nanomaterials,” *Nature Nanotechnology*, vol. 6, pp. 773–783, 2011.
- [142] E. Stern, G. Cheng, J. F. Klemic, E. Broomfield, D. Turner-Evans, C. Li, C. Zhou, and M. A. Reed, “Methods for fabricating ohmic contacts to nanowires and nanotubes,” *Journal of Vacuum Science & Technology B*, vol. 24, pp. 231–236, 2006.
- [143] Y. Hu, J. Zhou, P.-H. Yeh, Z. Li, T.-Y. Wei, and Z. L. Wang, “Super-sensitive, fast-response nanowire sensors by using Schottky contacts,” *Advanced Materials*, vol. 22, pp. 3327–3332, 2010.
- [144] N. S. Ramgir, Y. Yang, and M. Zacharias, “Nanowire-based sensors,” *Small*, vol. 6, pp. 1705–1722, 2010.
- [145] X. Chen, C. K. Y. Wong, C. A. Yuan, and G. Zhang, “Nanowire-based gas sensors,” *Sensors and Actuators B: Chemical*, vol. 177, pp. 178–195, 2013.
- [146] F. Hernandez-Ramirez, J. D. Prades, A. Tarancon, S. Barth, O. Casals, R. Jimenez-Diaz, E. Pellicer, J. Rodriguez, M. A. Juli, A. Romano-Rodriguez, J. R. Morante, S. Mathur, A. Helwig, J. Spannhake, and G. Mueller, “Portable microsensors based on individual SnO<sub>2</sub> nanowires,” *Nanotechnology*, vol. 18, p. 495501, 2007.
- [147] L. V. Thong, L. T. N. Loan, and N. Van Hieu, “Comparative study of gas sensor performance of SnO<sub>2</sub> nanowires and their hierarchical nanostructures,” *Sensors and Actuators B: Chemical*, vol. 150, pp. 112–119, 2010.
- [148] J. Prades, R. Jimenez-Diaz, F. Hernandez-Ramirez, S. Barth, A. Cirera, A. Romano-Rodriguez, S. Mathur, and J. R. Morante, “Equivalence between thermal and room temperature UV light-modulated responses of gas sensors based on individual SnO<sub>2</sub> nanowires,” *Sensors and Actuators B: Chemical*, vol. 140, pp. 337–341, 2009.
- [149] E. Comini, G. Faglia, G. Sberveglieri, D. Calestani, L. Zanotti, and M. Zha, “Tin oxide nanobelts electrical and sensing properties,” *Sensors and Actuators B: Chemical*, vol. 111–112, pp. 2–6, 2005.
- [150] E. Brunet, T. Maier, G. Mutinati, S. Steinhauer, A. Köck, C. Gspan, and W. Grogger, “Comparison of the gas sensing performance of SnO<sub>2</sub>

- thin film and SnO<sub>2</sub> nanowire sensors,” *Sensors and Actuators B: Chemical*, vol. 165, pp. 110–118, 2012.
- [151] F. Shao, M. Hoffmann, J. D. Prades, R. Zamani, J. Arbiol, J. R. Morante, E. Varechkina, M. Rumyantseva, A. Gaskov, I. Giebelhaus, T. Fischer, S. Mathur, and F. Hernandez-Ramirez, “Heterostructured p-CuO (nanoparticle)/n-SnO<sub>2</sub> (nanowire) devices for selective H<sub>2</sub>S detection,” *Sensors and Actuators B: Chemical*, vol. 181, pp. 130–135, 2013.
- [152] I.-S. Hwang, J.-K. Choi, S.-J. Kim, K.-Y. Dong, J.-H. Kwon, B.-K. Ju, and J.-H. Lee, “Enhanced H<sub>2</sub>S sensing characteristics of SnO<sub>2</sub> nanowires functionalized with CuO,” *Sensors and Actuators B: Chemical*, vol. 142, pp. 105–110, 2009.
- [153] I.-S. Hwang, S.-J. Kim, J.-K. Choi, J.-J. Jung, D. J. Yoo, K.-Y. Dong, B.-K. Ju, and J.-H. Lee, “Large-scale fabrication of highly sensitive SnO<sub>2</sub> nanowire network gas sensors by single step vapor phase growth,” *Sensors and Actuators B: Chemical*, vol. 165, pp. 97–103, 2012.
- [154] T.-Y. Wei, P.-H. Yeh, S.-Y. Lu, and Z. L. Wang, “Gigantic enhancement in sensitivity using Schottky contacted nanowire nanosensor,” *Journal of the American Chemical Society*, vol. 131, pp. 17690–17695, 2009.
- [155] S. K. Youn, N. Ramgir, C. Wang, K. Subannajui, V. Cimalla, and M. Zacharias, “Catalyst-free growth of ZnO nanowires based on topographical confinement and preferential chemisorption and their use for room temperature CO detection,” *The Journal of Physical Chemistry C*, vol. 114, pp. 10092–10100, 2010.
- [156] L. Li, H. Yang, H. Zhao, J. Yu, J. Ma, L. An, and X. Wang, “Hydrothermal synthesis and gas sensing properties of single-crystalline ultralong ZnO nanowires,” *Applied Physics A*, vol. 98, pp. 635–641, 2009.
- [157] S. J. Chang, W. Y. Weng, C. L. Hsu, and T. J. Hsueh, “High sensitivity of a ZnO nanowire-based ammonia gas sensor with Pt nano-particles,” *Nano Communication Networks*, vol. 1, pp. 283–288, 2010.
- [158] E. Comini, C. Baratto, G. Faglia, M. Ferroni, and G. Sberveglieri, “Single crystal ZnO nanowires as optical and conductometric chemical sensor,” *Journal of Physics D: Applied Physics*, vol. 40, pp. 7255–7259, 2007.

- [159] N. Datta, N. Ramgir, M. Kaur, S. Kailasa Ganapathi, A. K. Debnath, D. K. Aswal, and S. K. Gupta, "Selective H<sub>2</sub>S sensing characteristics of hydrothermally grown ZnO-nanowires network tailored by ultrathin CuO layers," *Sensors and Actuators B: Chemical*, vol. 166-167, 2012.
- [160] Q. Wan, Q. H. Li, Y. J. Chen, T. H. Wang, X. L. He, J. P. Li, and C. L. Lin, "Fabrication and ethanol sensing characteristics of ZnO nanowire gas sensors," *Applied Physics Letters*, vol. 84, p. 3654, 2004.
- [161] M. Mashock, K. Yu, S. Cui, S. Mao, G. Lu, and J. Chen, "Modulating gas sensing properties of CuO nanowires through creation of discrete nanosized p-n junctions on their surfaces," *ACS Applied Materials & Interfaces*, vol. 4, pp. 4192–4199, 2012.
- [162] D. Zappa, E. Comini, R. Zamani, J. Arbiol, J. R. Morante, and G. Sberveglieri, "Preparation of copper oxide nanowire-based conductometric chemical sensors," *Sensors and Actuators B: Chemical*, vol. 182, pp. 7–15, 2013.
- [163] P. Raksa, A. Gardchareon, T. Chairuangri, P. Mangkorntong, N. Mangkorntong, and S. Choopun, "Ethanol sensing properties of CuO nanowires prepared by an oxidation reaction," *Ceramics International*, vol. 35, pp. 649–652, 2009.
- [164] K. Ryu, D. Zhang, and C. Zhou, "High-performance metal oxide nanowire chemical sensors with integrated micromachined hotplates," *Applied Physics Letters*, vol. 92, p. 093111, 2008.
- [165] N. Singh, R. K. Gupta, and P. S. Lee, "Gold-nanoparticle-functionalized In<sub>2</sub>O<sub>3</sub> nanowires as CO gas sensors with a significant enhancement in response," *ACS Applied Materials & Interfaces*, vol. 3, pp. 2246–2252, 2011.
- [166] N. Singh, C. Yan, and P. S. Lee, "Room temperature CO gas sensing using Zn-doped In<sub>2</sub>O<sub>3</sub> single nanowire field effect transistors," *Sensors and Actuators B: Chemical*, vol. 150, pp. 19–24, 2010.
- [167] C. Li, D. Zhang, X. Liu, S. Han, T. Tang, J. Han, and C. Zhou, "In<sub>2</sub>O<sub>3</sub> nanowires as chemical sensors," *Applied Physics Letters*, vol. 82, p. 1613, 2003.
- [168] D. Zhang, Z. Liu, C. Li, T. Tang, X. Liu, S. Han, B. Lei, and C. Zhou, "Detection of NO<sub>2</sub> down to ppb levels using individual and multiple In<sub>2</sub>O<sub>3</sub> nanowire devices," *Nano Letters*, vol. 4, pp. 1919–1924, 2004.



- [169] A. Vomiero, S. Bianchi, E. Comini, G. Faglia, M. Ferroni, and G. Sberveglieri, “Controlled growth and sensing properties of  $\text{In}_2\text{O}_3$  nanowires,” *Crystal Growth & Design*, vol. 7, pp. 2500–2504, 2007.
- [170] Z. Zeng, K. Wang, Z. Zhang, J. Chen, and W. Zhou, “The detection of  $\text{H}_2\text{S}$  at room temperature by using individual indium oxide nanowire transistors,” *Nanotechnology*, vol. 20, p. 045503, 2009.
- [171] S. Park, H. Kim, C. Jin, S.-W. Choi, S. S. Kim, and C. Lee, “Enhanced CO gas sensing properties of Pt-functionalized  $\text{WO}_3$  nanorods,” *Thermochimica Acta*, vol. 542, pp. 69–73, 2012.
- [172] T. A. Ho, T.-S. Jun, and Y. S. Kim, “Material and  $\text{NH}_3$ -sensing properties of polypyrrole-coated tungsten oxide nanofibers,” *Sensors and Actuators B: Chemical*, vol. 185, pp. 523–529, 2013.
- [173] A. Ponzoni, E. Comini, G. Sberveglieri, J. Zhou, S. Z. Deng, N. S. Xu, Y. Ding, and Z. L. Wang, “Ultrasensitive and highly selective gas sensors using three-dimensional tungsten oxide nanowire networks,” *Applied Physics Letters*, vol. 88, p. 203101, 2006.
- [174] S. Park, S. Park, J. Jung, T. Hong, S. Lee, H. W. Kim, and C. Lee, “ $\text{H}_2\text{S}$  gas sensing properties of CuO-functionalized  $\text{WO}_3$  nanowires,” *Ceramics International*, vol. 40, pp. 11051–11056, 2014.
- [175] X. Liu, J. Zhang, T. Yang, X. Guo, S. Wu, and S. Wang, “Synthesis of Pt nanoparticles functionalized  $\text{WO}_3$  nanorods and their gas sensing properties,” *Sensors and Actuators B: Chemical*, vol. 156, pp. 918–923, 2011.
- [176] S. Vallejos, T. Stoycheva, P. Umek, C. Navio, R. Snyders, C. Bittencourt, E. Llobet, C. Blackman, S. Moniz, and X. Correig, “Au nanoparticle-functionalised  $\text{WO}_3$  nanoneedles and their application in high sensitivity gas sensor devices,” *Chemical Communications*, vol. 47, pp. 565–567, 2011.
- [177] A. Goldoni, L. Petaccia, S. Lizzit, and R. Larciprete, “Sensing gases with carbon nanotubes: A review of the actual situation,” *Journal of Physics: Condensed Matter*, vol. 22, p. 013001, 2010.
- [178] P. Bondavalli, P. Legagneux, and D. Pribat, “Carbon nanotubes based transistors as gas sensors: State of the art and critical review,” *Sensors and Actuators B: Chemical*, vol. 140, pp. 304–318, 2009.

- [179] D. R. Kauffman and A. Star, “Carbon nanotube gas and vapor sensors,” *Angewandte Chemie International Edition*, vol. 47, pp. 6550–6570, 2008.
- [180] T. Zhang, S. Mubeen, N. V. Myung, and M. A. Deshusses, “Recent progress in carbon nanotube-based gas sensors,” *Nanotechnology*, vol. 19, p. 332001, 2008.
- [181] M. F. L. De Volder, S. H. Tawfick, R. H. Baughman, and A. J. Hart, “Carbon nanotubes: Present and future commercial applications,” *Science*, vol. 339, pp. 535–539, 2013.
- [182] G. Shen, P.-C. Chen, K. Ryu, and C. Zhou, “Devices and chemical sensing applications of metal oxide nanowires,” *Journal of Materials Chemistry*, vol. 19, pp. 828–839, 2009.
- [183] M. Law, J. Goldberger, and P. Yang, “Semiconductor nanowires and nanotubes,” *Annual Review of Materials Research*, vol. 34, pp. 83–122, 2004.
- [184] H. J. Fan, P. Werner, and M. Zacharias, “Semiconductor nanowires: From self-organization to patterned growth,” *Small*, vol. 2, pp. 700–717, 2006.
- [185] G. Cao and D. Liu, “Template-based synthesis of nanorod, nanowire, and nanotube arrays,” *Advances in Colloid and Interface Science*, vol. 136, pp. 45–64, 2008.
- [186] T. Kimura, Y. Sekio, H. Nakamura, T. Siegrist, and A. P. Ramirez, “Cupric oxide as an induced-multiferroic with high- $T_C$ ,” *Nature Materials*, vol. 7, pp. 291–294, 2008.
- [187] D. Wu, Q. Zhang, and M. Tao, “LSDA+U study of cupric oxide: Electronic structure and native point defects,” *Physical Review B*, vol. 73, p. 235206, 2006.
- [188] G. Filipič and U. Cvelbar, “Copper oxide nanowires: A review of growth,” *Nanotechnology*, vol. 23, p. 194001, 2012.
- [189] K. Zhang, C. Rossi, C. Tenailleau, P. Alphonse, and J.-Y. Chané-Ching, “Synthesis of large-area and aligned copper oxide nanowires from copper thin film on silicon substrate,” *Nanotechnology*, vol. 18, p. 275607, 2007.

- [190] X. Jiang, T. Herricks, and Y. Xia, "CuO nanowires can be synthesized by heating copper substrates in air," *Nano Letters*, vol. 2, pp. 1333–1338, 2002.
- [191] M. L. Zhong, D. C. Zeng, Z. W. Liu, H. Y. Yu, X. C. Zhong, and W. Q. Qiu, "Synthesis, growth mechanism and gas-sensing properties of large-scale CuO nanowires," *Acta Materialia*, vol. 58, pp. 5926–5932, 2010.
- [192] A. M. B. Goncalves, L. C. Campos, A. S. Ferlauto, and R. G. Lacerda, "On the growth and electrical characterization of CuO nanowires by thermal oxidation," *Journal of Applied Physics*, vol. 106, p. 034303, 2009.
- [193] L. Yuan, Y. Wang, R. Mema, and G. Zhou, "Driving force and growth mechanism for spontaneous oxide nanowire formation during the thermal oxidation of metals," *Acta Materialia*, vol. 59, pp. 2491–2500, 2011.
- [194] M. Chen, Y. Yue, and Y. Ju, "Growth of metal and metal oxide nanowires driven by the stress-induced migration," *Journal of Applied Physics*, vol. 111, p. 104305, 2012.
- [195] C. Sequeira, "High-temperature oxidation," in *Uhlig's Corrosion Handbook* (R. Winston Revie, ed.), Hoboken: John Wiley & Sons, 2011. ISBN: 978-0-470-08032-0.
- [196] X. Li, J. Zhang, Y. Yuan, L. Liao, and C. Pan, "Effect of electric field on CuO nanoneedle growth during thermal oxidation and its growth mechanism," *Journal of Applied Physics*, vol. 108, p. 024308, 2010.
- [197] R. Mema, L. Yuan, Q. Du, Y. Wang, and G. Zhou, "Effect of surface stresses on CuO nanowire growth in the thermal oxidation of copper," *Chemical Physics Letters*, vol. 512, pp. 87–91, 2011.
- [198] F. Wu, Y. Myung, and P. Banerjee, "Unravelling transient phases during thermal oxidation of copper for dense CuO nanowire growth," *CrystEngComm*, vol. 16, p. 3264, 2014.
- [199] S.-L. Cheng and M.-F. Chen, "Fabrication, characterization, and kinetic study of vertical single-crystalline CuO nanowires on Si substrates," *Nanoscale Research Letters*, vol. 7, p. 119, 2012.
- [200] C.-L. Cheng, Y.-R. Ma, M. H. Chou, C. Y. Huang, V. Yeh, and S. Y. Wu, "Direct observation of short-circuit diffusion during the formation

- of a single cupric oxide nanowire,” *Nanotechnology*, vol. 18, p. 245604, 2007.
- [201] B. J. Hansen, H.-I. Chan, J. Lu, G. Lu, and J. Chen, “Short-circuit diffusion growth of long bi-crystal CuO nanowires,” *Chemical Physics Letters*, vol. 504, pp. 41–45, 2011.
- [202] C.-Y. Huang, A. Chatterjee, S. B. Liu, S. Y. Wu, and C.-L. Cheng, “Photoluminescence properties of a single tapered CuO nanowire,” *Applied Surface Science*, vol. 256, pp. 3688–3692, 2010.
- [203] M. Petrantoni, C. Rossi, V. Conédéra, D. Bourrier, P. Alphonse, and C. Tenailleau, “Synthesis process of nanowired Al/CuO thermite,” *Journal of Physics and Chemistry of Solids*, vol. 71, pp. 80–83, 2010.
- [204] C. H. Xu, C. H. Woo, and S. Q. Shi, “The effects of oxidative environments on the synthesis of CuO nanowires on Cu substrates,” *Superlattices and Microstructures*, vol. 36, pp. 31–38, 2004.
- [205] C. Xu, X. Yang, S.-Q. Shi, Y. Liu, C. Surya, and C. Woo, “Effects of local gas-flow field on synthesis of oxide nanowires during thermal oxidation,” *Applied Physics Letters*, vol. 92, p. 253117, 2008.
- [206] S. Rackauskas, A. G. Nasibulin, H. Jiang, Y. Tian, V. I. Kleshch, J. Sainio, E. D. Obraztsova, S. N. Bokova, A. N. Obraztsov, and E. I. Kauppinen, “A novel method for metal oxide nanowire synthesis,” *Nanotechnology*, vol. 20, p. 165603, 2009.
- [207] R. D. Leapman, L. A. Grunes, and P. L. Fejes, “Study of the  $L_{23}$  edges in the  $3d$  transition metals and their oxides by electron-energy-loss spectroscopy with comparisons to theory,” *Physical Review B*, vol. 26, pp. 614–635, 1982.
- [208] L. A. Grunes, R. D. Leapman, and C. N. Wilker, “Oxygen K near-edge fine structure: An electron-energy-loss investigation with comparisons to new theory for selected  $3d$  transition-metal oxides,” *Physical Review B*, vol. 25, pp. 7157–7173, 1982.
- [209] WEELS - Webservice for Electron Energy Loss Spectra, <http://muller.research.engineering.cornell.edu/sites/WEELS/>, 30.5.2014.
- [210] Z. L. Wang, “ZnO nanowire and nanobelt platform for nanotechnology,” *Materials Science and Engineering R*, vol. 64, pp. 33–71, 2009.

- [211] H. Morkoç and U. Özgür, *Zinc Oxide: Fundamentals, Materials and Device Technology*. Weinheim: Wiley-VCH, 2009. ISBN: 978-3-527-40813-9.
- [212] A. Janotti and C. G. Van de Walle, “Fundamentals of zinc oxide as a semiconductor,” *Reports on Progress in Physics*, vol. 72, p. 126501, 2009.
- [213] G.-C. Yi, C. Wang, and W. I. Park, “ZnO nanorods: Synthesis, characterization and applications,” *Semiconductor Science and Technology*, vol. 20, pp. S22–S34, 2005.
- [214] S. Ren, Y. F. Bai, J. Chen, S. Z. Deng, N. S. Xu, Q. B. Wu, and S. Yang, “Catalyst-free synthesis of ZnO nanowire arrays on zinc substrate by low temperature thermal oxidation,” *Materials Letters*, vol. 61, pp. 666–670, 2007.
- [215] Z. L. Wang, “Zinc oxide nanostructures: Growth, properties and applications,” *Journal of Physics: Condensed Matter*, vol. 16, pp. R829–R858, 2004.
- [216] L. Wang, X. Zhang, S. Zhao, G. Zhou, Y. Zhou, and J. Qi, “Synthesis of well-aligned ZnO nanowires by simple physical vapor deposition on *c*-oriented ZnO thin films without catalysts or additives,” *Applied Physics Letters*, vol. 86, p. 024108, 2005.
- [217] J. Q. Hu, Q. Li, N. B. Wong, C. S. Lee, and S. T. Lee, “Synthesis of uniform hexagonal prismatic ZnO whiskers,” *Chemistry of Materials*, vol. 14, pp. 1216–1219, 2002.
- [218] C. Geng, Y. Jiang, Y. Yao, X. Meng, J. A. Zapien, C. S. Lee, Y. Lifshitz, and S. T. Lee, “Well-aligned ZnO nanowire arrays fabricated on silicon substrates,” *Advanced Functional Materials*, vol. 14, pp. 589–594, 2004.
- [219] S. Li, X. Zhang, B. Yan, and T. Yu, “Growth mechanism and diameter control of well-aligned small-diameter ZnO nanowire arrays synthesized by a catalyst-free thermal evaporation method,” *Nanotechnology*, vol. 20, p. 495604, 2009.
- [220] H. Y. Dang, J. Wang, and S. S. Fan, “The synthesis of metal oxide nanowires by directly heating metal samples in appropriate oxygen atmospheres,” *Nanotechnology*, vol. 14, pp. 738–741, 2003.

- [221] T.-W. Kim, T. Kawazoe, S. Yamazaki, M. Ohtsu, and T. Sekiguchi, “Low-temperature orientation-selective growth and ultraviolet emission of single-crystal ZnO nanowires,” *Applied Physics Letters*, vol. 84, p. 3358, 2004.
- [222] J. B. K. Law, C. B. Boothroyd, and J. T. L. Thong, “Site-specific growth of ZnO nanowires from patterned Zn via compatible semiconductor processing,” *Journal of Crystal Growth*, vol. 310, pp. 2485–2492, 2008.
- [223] H. J. Fan, R. Scholz, F. M. Kolb, and M. Zacharias, “Two-dimensional dendritic ZnO nanowires from oxidation of Zn microcrystals,” *Applied Physics Letters*, vol. 85, p. 4142, 2004.
- [224] S. Rackauskas, A. G. Nasibulin, H. Jiang, Y. Tian, G. Statkute, S. D. Shandakov, H. Lipsanen, and E. I. Kauppinen, “Mechanistic investigation of ZnO nanowire growth,” *Applied Physics Letters*, vol. 95, p. 183114, 2009.
- [225] C. X. Zhao, Y. F. Li, J. Zhou, L. Y. Li, S. Z. Deng, N. S. Xu, and J. Chen, “Large-scale synthesis of bicrystalline ZnO nanowire arrays by thermal oxidation of zinc film: Growth mechanism and high-performance field emission,” *Crystal Growth & Design*, vol. 13, pp. 2897–2905, 2013.
- [226] W. Yu and C. Pan, “Low temperature thermal oxidation synthesis of ZnO nanoneedles and the growth mechanism,” *Materials Chemistry and Physics*, vol. 115, pp. 74–79, 2009.
- [227] L.-C. Chao, C.-F. Lin, and C.-C. Liao, “Effect of surface morphology of metallic zinc films deposited by ion beam sputter deposition on the formation of ZnO nanowires,” *Vacuum*, vol. 86, pp. 295–298, 2011.
- [228] C. H. Xu, H. F. Lui, and C. Surya, “Synthesis of ZnO nanostructures by thermal oxidation in water vapor containing environments,” *Materials Letters*, vol. 65, pp. 27–30, 2011.
- [229] S. C. Lyu, Y. Zhang, C. J. Lee, H. Ruh, and H. J. Lee, “Low-temperature growth of ZnO nanowire array by a simple physical vapor-deposition method,” *Chemistry of Materials*, vol. 15, pp. 3294–3299, 2003.
- [230] Y. Ding and Z. L. Wang, “Structures of planar defects in ZnO nanobelts and nanowires,” *Micron*, vol. 40, pp. 335–342, 2009.

- [231] H. Schmid, E. Okunishi, T. Oikawa, and W. Mader, “Structural and elemental analysis of iron and indium doped zinc oxide by spectroscopic imaging in Cs-corrected STEM,” *Micron*, vol. 43, pp. 49–56, 2012.
- [232] The EELS Data Base, <http://pc-web.cemes.fr/eelsdb/>, 6.6.2014.
- [233] Y. Ding and Z. L. Wang, “Electron energy-loss spectroscopy study of ZnO nanobelts,” *Journal of Electron Microscopy*, vol. 54, pp. 287–291, 2005.
- [234] Y. Marechal, *The Hydrogen Bond and the Water Molecule*. Amsterdam: Elsevier, 2007. ISBN: 978-0-444-51957-3.
- [235] N. Wiberg, A. Holleman, and E. Wiberg, *Inorganic Chemistry*. London: Academic Press, 2001. ISBN: 978-0-12-352651-9.
- [236] N. J. Tro, *Chemistry: A Molecular Approach*. Upper Saddle River: Prentice Hall, 2011. ISBN: 978-0-321-65178-5.
- [237] European Commission, “Commission Directive 2009/161/EU, OJ L 338, p. 87-89,” 19.12.2009.
- [238] R. Grinter, *The Quantum in Chemistry*. Chichester: John Wiley & Sons, 2005. ISBN: 978-0-470-01318-2.
- [239] J. N. Spencer, G. M. Bodner, and L. H. Rickard, *Chemistry: Structure and Dynamics*. Hoboken: John Wiley & Sons, 2012. ISBN: 978-0-470-587119.
- [240] B. Darwent, *Bond dissociation energies in simple molecules*. National Standard Reference Data System, NSRDS-NBS-31, National Bureau of Standards, 1970.
- [241] O. Wunnicke, “Gate capacitance of back-gated nanowire field-effect transistors,” *Applied Physics Letters*, vol. 89, p. 083102, 2006.
- [242] D. R. Khanal and J. Wu, “Gate coupling and charge distribution in nanowire field effect transistors,” *Nano Letters*, vol. 7, pp. 2778–2783, 2007.
- [243] A. A. Samokhvalov, N. A. Viglin, B. A. Gizhevskii, N. N. Loshkareva, V. V. Osipov, N. I. Solin, and Y. P. Sukhorukov, “Low-mobility charge carriers in CuO,” *Journal of Experimental and Theoretical Physics*, vol. 76, pp. 463–468, 1993.

- [244] D. Vashaee, A. Shakouri, J. Goldberger, T. Kuykendall, P. Pauzauskie, and P. Yang, “Electrostatics of nanowire transistors with triangular cross sections,” *Journal of Applied Physics*, vol. 99, p. 054310, 2006.
- [245] R. Martel, T. Schmidt, H. R. Shea, T. Hertel, and P. Avouris, “Single- and multi-wall carbon nanotube field-effect transistors,” *Applied Physics Letters*, vol. 73, p. 2447, 1998.
- [246] F. Hernandez-Ramirez, A. Tarancon, O. Casals, J. Rodriguez, A. Romano-Rodriguez, J. R. Morante, S. Barth, S. Mathur, T. Y. Choi, D. Poulikakos, V. Callegari, and P. M. Nellen, “Fabrication and electrical characterization of circuits based on individual tin oxide nanowires,” *Nanotechnology*, vol. 17, pp. 5577–5583, 2006.
- [247] A. M. Abdul-Lettif, “Auger depth profiling of heat-treated Au/Ni thin films,” *Surface and Interface Analysis*, vol. 33, pp. 306–308, 2002.
- [248] G. Korotcenkov and B. Cho, “Instability of metal oxide-based conductometric gas sensors and approaches to stability improvement (short survey),” *Sensors and Actuators B: Chemical*, vol. 156, pp. 527–538, 2011.
- [249] J. H. He, P. H. Chang, C. Y. Chen, and K. T. Tsai, “Electrical and optoelectronic characterization of a ZnO nanowire contacted by focused-ion-beam-deposited Pt,” *Nanotechnology*, vol. 20, p. 135701, 2009.
- [250] E. Schlenker, A. Bakin, T. Weimann, P. Hinze, D. H. Weber, A. Götzhäuser, H.-H. Wehmann, and A. Waag, “On the difficulties in characterizing ZnO nanowires,” *Nanotechnology*, vol. 19, p. 365707, 2008.
- [251] S.-P. Chang, S.-J. Chang, C.-Y. Lu, M.-J. Li, C.-L. Hsu, Y.-Z. Chiou, T.-J. Hsueh, and I.-C. Chen, “A ZnO nanowire-based humidity sensor,” *Superlattices and Microstructures*, vol. 47, pp. 772–778, 2010.
- [252] P. Li, Q. Liao, Z. Zhang, Z. Wang, P. Lin, X. Zhang, Z. Kang, Y. Huang, Y. Gu, X. Yan, and Y. Zhang, “Investigation on the mechanism of nanodamage and nanofailure for single ZnO nanowires under an electric field,” *ACS Applied Materials & Interfaces*, vol. 6, pp. 2344–2349, 2014.
- [253] A. Nie, J. Liu, C. Dong, and H. Wang, “Electrical failure behaviors of semiconductor oxide nanowires,” *Nanotechnology*, vol. 22, p. 405703, 2011.



- [254] C.-Y. Lee, M.-P. Lu, K.-F. Liao, W.-F. Lee, C.-T. Huang, S.-Y. Chen, and L.-J. Chen, “Free-standing single-crystal NiSi<sub>2</sub> nanowires with excellent electrical transport and field emission properties,” *The Journal of Physical Chemistry C*, vol. 113, pp. 2286–2289, 2009.
- [255] F. Zhang, A. Zhu, Y. Luo, Y. Tian, J. Yang, and Y. Qin, “CuO nanosheets for sensitive and selective determination of H<sub>2</sub>S with high recovery ability,” *The Journal of Physical Chemistry C*, vol. 114, pp. 19214–19219, 2010.
- [256] J. Hennemann, T. Sauerwald, C.-D. Kohl, T. Wagner, M. Bognitzki, and A. Greiner, “Electrospun copper oxide nanofibers for H<sub>2</sub>S dosimetry,” *Physica Status Solidi A*, vol. 209, pp. 911–916, 2012.
- [257] S. Mubeen, T. Zhang, N. Chartuprayoon, Y. Rheem, A. Mulchandani, N. V. Myung, and M. A. Deshusses, “Sensitive detection of H<sub>2</sub>S using gold nanoparticle decorated single-walled carbon nanotubes,” *Analytical Chemistry*, vol. 82, pp. 250–257, 2010.
- [258] G. H. Jain and L. A. Patil, “CuO-doped BSST thick film resistors for ppb level H<sub>2</sub>S gas sensing at room temperature,” *Sensors and Actuators B: Chemical*, vol. 123, pp. 246–253, 2007.
- [259] M. D. Shirsat, M. A. Bangar, M. A. Deshusses, N. V. Myung, and A. Mulchandani, “Polyaniline nanowires-gold nanoparticles hybrid network based chemiresistive hydrogen sulfide sensor,” *Applied Physics Letters*, vol. 94, p. 083502, 2009.
- [260] N. Zhang, K. Yu, Q. Li, Z. Q. Zhu, and Q. Wan, “Room-temperature high-sensitivity H<sub>2</sub>S gas sensor based on dendritic ZnO nanostructures with macroscale in appearance,” *Journal of Applied Physics*, vol. 103, p. 104305, 2008.
- [261] J. Kim and K. Yong, “Mechanism study of ZnO nanorod-bundle sensors for H<sub>2</sub>S gas sensing,” *The Journal of Physical Chemistry C*, vol. 115, pp. 7218–7224, 2011.
- [262] R. K. Joshi, Q. Hu, F. Alvi, N. Joshi, and A. Kumar, “Au decorated zinc oxide nanowires for CO sensing,” *The Journal of Physical Chemistry C*, vol. 113, pp. 16199–16202, 2009.
- [263] S.-J. Chang, T.-J. Hsueh, I.-C. Chen, and B.-R. Huang, “Highly sensitive ZnO nanowire CO sensors with the adsorption of Au nanoparticles,” *Nanotechnology*, vol. 19, p. 175502, 2008.

- [264] A. Fort, M. Mugnaini, I. Pasquini, S. Rocchi, and V. Vignoli, “Modeling of the influence of H<sub>2</sub>O on metal oxide sensor responses to CO,” *Sensors and Actuators B: Chemical*, vol. 159, pp. 82–91, 2011.
- [265] M. Siegele, C. Gamauf, A. Nemecek, G. C. Mutinati, S. Steinhauer, A. Köck, J. Kraft, J. Siegert, and F. Schrank, “Optimized integrated micro-hotplates in CMOS technology,” in *Proceedings of the 11<sup>th</sup> International New Circuits and Systems Conference (NEWCAS), Paris, France, 2013*. DOI:10.1109/NEWCAS.2013.6573624.
- [266] A. Tischner, T. Maier, C. Stepper, and A. Köck, “Ultrathin SnO<sub>2</sub> gas sensors fabricated by spray pyrolysis for the detection of humidity and carbon monoxide,” *Sensors and Actuators B: Chemical*, vol. 134, pp. 796–802, 2008.

## List of Figures

1.1	Important aspects of nanowire-based devices for the gas sensing application	3
2.1	Interactions between solids and gas molecules	10
2.2	Lennard-Jones model for physisorption and chemisorption	12
2.3	Density of adsorbed gas molecules	14
2.4	Surface band bending due to ionosorption of oxygen	15
2.5	Schematics of a conductometric gas sensor based on a polycrystalline film	17
2.6	Conduction mechanism of a porous thick film gas sensor device	18
2.7	Bell-shaped temperature dependence of the sensor response	20
2.8	Interaction between metal oxides and surface additives	22
2.9	Typical waveforms of temperature modulated gas sensors	23
2.10	Schematics of a System on Chip electronic nose device	25
3.1	Top-down and bottom-up paradigms for nanostructure synthesis	27
3.2	Energy band diagrams of metals and semiconductors	30
3.3	Metal contacts to p-type semiconductors	31
3.4	Metal contacts to n-type semiconductors	31
3.5	Band bending at metal oxide nanowire surfaces	35
3.6	Sensor response in nanowire networks	36
4.1	Bottom-up techniques for nanowire synthesis	41
4.2	Schematics of the grain boundary diffusion model for CuO nanowire growth	45
4.3	CuO nanowire synthesis by thermal oxidation of a Cu wire	48
4.4	CuO nanowire characterization (growth on Cu wire)	50
4.5	Fabrication of electroplated Cu structures	51
4.6	CuO nanowire synthesis by thermal oxidation of electroplated Cu structures	52
4.7	CuO nanowire characterization (growth on electroplated Cu structures)	54
4.8	CuO nanowire synthesis by thermal oxidation of evaporated Cu structures	57
4.9	XRD of CuO nanowire sample (growth on evaporated Cu structures)	58
4.10	ZnO nanowire synthesis by vapor solid growth using a Zn wire	63
4.11	Characterization of ZnO nanowires synthesized by vapor phase growth	65
4.12	ZnO nanowire synthesis by thermal oxidation of Zn structures	67
4.13	Characterization of Zn structures before and after thermal oxidation	69
5.1	Assembled gas sensor connected to the ceramic sensor carrier	70
5.2	Schematics of the gas sensor setup	71
6.1	Process flows for single nanowire device fabrication	75
6.2	Single nanowire devices in a two-point configuration	76
6.3	Electrical characterization of a single CuO nanowire (two-point configuration)	77

6.4	Transport parameters of single CuO nanowires (two-point configuration)	78
6.5	Fabrication of single CuO nanowire devices in a four-point configuration	80
6.6	Two-point and four-point IV characteristics of a single CuO nanowire device	82
6.7	Cross-sectional transmission electron microscopy of Ni/Au contacts	83
6.8	Temperature dependence of electrical conductivity of four CuO nanowires	84
6.9	Gas measurements on two single CuO nanowires (four-point configuration)	85
6.10	Fabrication and characterization of single suspended CuO nanowire devices	86
6.11	Gas measurements on single suspended CuO nanowire	87
6.12	Comparison of CO response of five single CuO nanowire devices	89
6.13	Single ZnO nanowire device and the IV characteristics	90
6.14	Electrical resistance of single ZnO nanowire during exposure to humidity	91
7.1	CuO nanowire array devices (electroplated Cu)	94
7.2	Gas measurements on CuO nanowire array devices (electroplated Cu)	96
7.3	CuO nanowire array devices (evaporated Cu)	99
7.4	Gas measurements on CuO nanowire array devices (evaporated Cu)	101
7.5	ZnO nanowire and ZnO/Au nanowire array devices	104
7.6	H <sub>2</sub> S sensing with ZnO nanowire array devices	105
7.7	CO sensing with ZnO/Au nanowire array device	106
8.1	Evaluation of CO sensor response in dry and humid atmosphere	108
8.2	ppb-level H <sub>2</sub> S sensing in dry and humid atmosphere	110
8.3	Evaluation of H <sub>2</sub> S sensor response in dry and humid atmosphere	112
8.4	IV characteristics of the three CuO nanowire sensors at T=325 °C	114
9.1	CMOS microhotplate schematics	117
9.2	CMOS microhotplate and its device performance	118
9.3	Device fabrication process flow	119
9.4	Integration of CuO nanowire arrays on CMOS microhotplates	120
9.5	Gas measurements on CMOS integrated CuO nanowire array	121
10.1	CuO nanowires decorated with metal nanoparticles	122
10.2	Synthesis of CuO-ZnO heterostructures	123
10.3	Self-aligned fabrication of CuO-SnO <sub>2</sub> heterojunctions by Ar ion etching	124

## List of Tables

3.1	Overview of metal oxide nanowire based gas sensor devices	39
7.1	H <sub>2</sub> S detection: comparison of CuO nanowire array with literature results	100
A.1	Process parameters for photolithography lift-off process	159
A.2	Process parameters for electron beam lithography lift-off process	160
B.1	Test gas compositions (Linde Gas)	160

# Appendices

## A Lithography Processes

<i>Description</i>	<i>Parameters</i>	<i>Used equipment</i>
resist	AZ5214E (MicroChemicals GmbH)	-
spin coating	4000 rpm; 35 s	Ramgraber M-Spin150
prebake	100 °C; 60 s	hotplate
exposure	80 mJ/cm <sup>2</sup>	EVG620 mask aligner
reversal bake	100 °C; 60 s	hotplate
flood exposure	250 mJ/cm <sup>2</sup>	EVG620 mask aligner
development	AZ726 MIF; 35 s	-
rinsing	DI water; >2 min	-
metal deposition	material dependent	Univex 450 evaporator Univex 450C sputtering
lift-off	Aceton; >8 h	-
rinsing	Isopropanol; >1 min	-

Table A.1: Process parameters for photolithography lift-off process

<i>Description</i>	<i>Parameters</i>	<i>Used equipment</i>
resist	ARP 679.04 (Allresist GmbH)	-
spin coating	4000 rpm; 45 s	Ramgraber M-Spin150
prebake	150 °C; 120 s	hotplate
exposure	144 $\mu\text{A s}/\text{cm}^2$ acceleration voltage 20 kV	Zeiss SEM Supra 40
development	AR 600-56; 60 s AR 600-60; 30 s	-
metal deposition	material dependent	Univex 450 Evaporator Univex 450C sputtering
lift-off	Aceton; >8 h	-
rinsing	Isopropanol; >1 min	-

Table A.2: Process parameters for electron beam lithography lift-off process

## B Test Gas Compositions

<i>Test gas</i>	<i>Diluted in</i>	<i>Concentration</i>
synthetic air	-	80% N <sub>2</sub> , 20% O <sub>2</sub> <0.1 ppm hydrocarbons <0.1 ppm NO <sub>x</sub>
CO	N <sub>2</sub>	902 ppm
H <sub>2</sub> S	N <sub>2</sub>	10.1 ppm
H <sub>2</sub> S (low conc.)	N <sub>2</sub>	0.61 ppm

Table B.1: Test gas compositions (Linde Gas)

# List of Publications

## Journal Articles

- \* S. Steinhauer, E. Brunet, T. Maier, G. C. Mutinati, A. Köck, O. Freudenberg, C. Gspan, W. Grogger, A. Neuhold, and R. Resel, "Gas sensing properties of novel CuO nanowire devices," *Sensors and Actuators B: Chemical*, vol. 187, pp. 50-57, 2013.
- \* S. Steinhauer, E. Brunet, T. Maier, G. C. Mutinati, and A. Köck, "Suspended CuO nanowires for ppb level H<sub>2</sub>S sensing in dry and humid atmosphere," *Sensors and Actuators B: Chemical*, vol. 186, pp. 550-556, 2013.
- \* E. Brunet, T. Maier, G. C. Mutinati, S. Steinhauer, A. Köck, C. Gspan, and W. Grogger, "Comparison of the gas sensing performance of SnO<sub>2</sub> thin film and SnO<sub>2</sub> nanowire sensors," *Sensors and Actuators B: Chemical*, vol. 165, pp. 110-118, 2012.
- \* G. Tulzer, S. Baumgartner, E. Brunet, G. C. Mutinati, S. Steinhauer, A. Köck, P. E. Barbano, and C. Heitzinger, "Kinetic parameter estimation and fluctuation analysis of CO at SnO<sub>2</sub> single nanowires," *Nanotechnology*, vol. 24, p. 315501, 2013.
- \* L. Filipovic, S. Selberherr, G. C. Mutinati, E. Brunet, S. Steinhauer, A. Köck, J. Teva, J. Kraft, J. Siegert, and F. Schrank, "Methods of simulating thin film deposition using spray pyrolysis techniques," *Microelectronic Engineering*, vol. 117, pp. 57-66, 2014.
- \* L. Filipovic, S. Selberherr, G. C. Mutinati, E. Brunet, S. Steinhauer, A. Köck, J. Teva, J. Kraft, J. Siegert, F. Schrank, C. Gspan, and W. Grogger, "Modeling the growth of tin dioxide using spray pyrolysis deposition for gas sensor applications," *IEEE Transactions on Semiconductor Manufacturing*, vol. 27, pp. 269-277, 2014.
- \* C. Griessler, E. Brunet, T. Maier, S. Steinhauer, A. Köck, T. Jordi, F. Schrank, and M. Schrems, "Tin oxide nanosensors for highly sensitive toxic gas detection and their 3D system integration," *Microelectronic Engineering*, vol. 88, pp. 1779-1781, 2011.
- \* S. Steinhauer, M. Eggeling, T. Maier, G. C. Mutinati, R. Resel, and A. Köck, "Direct integration of ZnO nanowires for gas sensing applications," *in preparation*.
- \* S. Steinhauer, T. Maier, G. C. Mutinati, C. Gspan, W. Grogger, and A. Köck, "Synthesis and characterization of ZnO nanowires and their potential for self-heated gas sensor devices," *in preparation*.

## Book Chapter

- \* E. Brunet, G. C. Mutinati, S. Steinhauer, and A. Köck, "Oxide ultrathin films in sensor applications," in *Oxide Ultrathin Films: Science and Technology* (G. Pacchioni and S. Valeri, eds.), Weinheim: Wiley-VCH, 2012. ISBN: 978-3-527-33016-4.



## Conference Contributions (First Author)

- \* S. Steinhauer, T. Maier, G. C. Mutinati, K. Rohracher, J. Siegert, F. Schrank, and A. Köck, “Local synthesis of CuO nanowires on CMOS microhotplates for gas sensing applications,” in *Proceedings of TechConnect World Nanotech, Washington D.C., USA, 2014*. ISBN: 978-1-4822-5827-12014, pp.53-56.
- \* S. Steinhauer, E. Brunet, T. Maier, G. C. Mutinati, and A. Köck, “Single CuO nanowire devices for gas sensing applications,” in *Proceedings of the 1<sup>st</sup> International Symposium on Nanoparticles/Nanomaterials and Applications (ISN<sup>2</sup>A), Caparica, Portugal, 2014*. ISBN: 978-989-98415-9-8, pp.90-91.  
awarded with Young Scientist Best Presentation Award
- \* S. Steinhauer, E. Brunet, T. Maier, G. C. Mutinati, and A. Köck, “CuO nanowire gas sensors for the detection of low ppb level concentrations of H<sub>2</sub>S,” in *5<sup>th</sup> International Conference on One Dimensional Nanomaterials (ICON), Annecy, France, 2013*.
- \* S. Steinhauer, E. Brunet, T. Maier, G. C. Mutinati, and A. Köck, “Direct integration of ZnO nanowires for gas sensing applications,” in *39<sup>th</sup> International Conference on Micro and Nano Engineering (MNE), London, United Kingdom, 2013*.
- \* S. Steinhauer, E. Brunet, T. Maier, G. C. Mutinati, and A. Köck, “CuO nanowire gas sensors for CO detection in humid atmosphere,” in *Proceedings of the 17<sup>th</sup> International Conference on Solid-State Sensors, Actuators and Microsystems (Transducers & Eurosensors XXVII), Barcelona, Spain, 2013*. DOI:10.1109/Transducers.2013.6626962.
- \* S. Steinhauer, E. Brunet, T. Maier, G. C. Mutinati, A. Köck, and O. Freudenberg, “Single suspended CuO nanowire for conductometric gas sensing,” in *Proceedings of Eurosensors XXVI, Kraków, Poland, 2012. Procedia Engineering*, vol.47, pp. 17-20.
- \* S. Steinhauer, E. Brunet, T. Maier, G. C. Mutinati, and A. Köck, “On-chip synthesis of CuO nanowires for direct gas sensor integration,” in *Proceedings of the 12<sup>th</sup> International Conference on Nanotechnology (IEEE-NANO), Birmingham, United Kingdom, 2012*. DOI:10.1109/NANO.2012.6321957.
- \* S. Steinhauer, E. Brunet, G. C. Mutinati, and A. Köck, “Four-point electrical characterization and gas sensing properties of CuO nanowire devices,” in *DPG Spring Meeting, Berlin, Germany, 2012*.
- \* S. Steinhauer, E. Brunet, T. Maier, G. C. Mutinati, A. Köck, and O. Freudenberg, “Gas sensing properties of novel CuO nanowire devices,” in *Proceedings of the 14<sup>th</sup> International Meeting on Chemical Sensors (IMCS), Nuremberg, Germany, 2012*. DOI:10.5162/IMCS2012/8.4.2.
- \* S. Steinhauer, E. Brunet, T. Maier, G. C. Mutinati, and A. Köck, “Integration schemes for CuO nanowires as gas sensor components,” in *9<sup>th</sup> International Nanotechnology Symposium - New ideas for industry - (Nanofair), Dresden, Germany, 2012*.
- \* S. Steinhauer, E. Brunet, T. Maier, G. C. Mutinati, A. Köck, O. Freudenberg, C. Gspan, and G. Kothleitner, “CMOS compatible fabrication of cupric oxide nanowire devices,” in *37<sup>th</sup> International Conference on Micro and Nano Engineering (MNE), Berlin, Germany, 2011*.

- \* S. Steinhauer, E. Brunet, C. Griessler, M. Milnera, G. C. Mutinati, A. Köck, C. Edtmaier, W.-D. Schubert, C. Gspan, and G. Kothleitner, "Synthesis, characterization and gas sensing applications of CuO nanowires," in *DPG Spring Meeting, Dresden, Germany, 2011*.
- \* S. Steinhauer, E. Brunet, T. Maier, G. C. Mutinati, A. Köck, W.-D. Schubert, C. Edtmaier, C. Gspan, and W. Grogger, "Synthesis of high-aspect-ratio CuO nanowires for conductometric gas sensing," in *Proceedings of Euroensors XXV, Athens, Greece, 2011. Procedia Engineering*, vol.25, pp. 1477-1480.

# Curriculum Vitae

## Personal Data

Name	Stephan Steinhauer
Date of birth	29.09.1986
Place of birth	Vienna
Nationality	Austria

## Education

10/2011 - present	Doctoral programme in Engineering Sciences Vienna University of Technology
10/2008 - 04/2011	Master programme Microelectronics Vienna University of Technology
10/2005 - 06/2008	Bachelor programme Microsystems Engineering University of Applied Sciences Wr. Neustadt
10/2012 - present	Master programme Technical Physics Vienna University of Technology
10/2008 - 10/2012	Bachelor programme Technical Physics Vienna University of Technology

## Career

03/2014 - present	Materials Center Leoben Research Fellow
08/2010 - 02/2014	AIT Austrian Institute of Technology Research Fellow
03/2010 - 06/2010	Vienna University of Technology Teaching Assistant
07/2008 - 08/2008	Sagem Communications Internship
02/2008 - 05/2008	Piezocryst Advanced Sensorics Internship